

INFORMATION TO USERS

This manuscript has been reproduced from the microfilm master. UMI films the text directly from the original or copy submitted. Thus, some thesis and dissertation copies are in typewriter face, while others may be from any type of computer printer.

The quality of this reproduction is dependent upon the quality of the copy submitted. Broken or indistinct print, colored or poor quality illustrations and photographs, print bleedthrough, substandard margins, and improper alignment can adversely affect reproduction.

In the unlikely event that the author did not send UMI a complete manuscript and there are missing pages, these will be noted. Also, if unauthorized copyright material had to be removed, a note will indicate the deletion.

Oversize materials (e.g., maps, drawings, charts) are reproduced by sectioning the original, beginning at the upper left-hand corner and continuing from left to right in equal sections with small overlaps. Each original is also photographed in one exposure and is included in reduced form at the back of the book.

Photographs included in the original manuscript have been reproduced xerographically in this copy. Higher quality 6" x 9" black and white photographic prints are available for any photographs or illustrations appearing in this copy for an additional charge. Contact UMI directly to order.

UMI

**A Bell & Howell Information Company
300 North Zeeb Road, Ann Arbor MI 48106-1346 USA
313/761-4700 800/521-0600**

UNIVERSITY OF ALBERTA

A COINCIDENCE MEASUREMENT
OF THE $D(\gamma, pp\pi^-)$ CROSS SECTION
IN THE REGION OF THE Δ RESONANCE

BY

MAHER A. QURAAN



A thesis
submitted to the Faculty of Graduate Studies and Research
in partial fulfillment of the requirements for the degree of

DOCTOR OF PHILOSOPHY

IN

NUCLEAR PHYSICS

DEPARTMENT OF PHYSICS

EDMONTON, ALBERTA

Spring 1997



**National Library
of Canada**

**Acquisitions and
Bibliographic Services**

**385 Wellington Street
Ottawa ON K1A 0N4
Canada**

**Bibliothèque nationale
du Canada**

**Acquisitions et
services bibliographiques**

**385, rue Wellington
Ottawa ON K1A 0N4
Canada**

Your file Votre référence

Our file Notre référence

The author has granted a non-exclusive licence allowing the National Library of Canada to reproduce, loan, distribute or sell copies of his/her thesis by any means and in any form or format, making this thesis available to interested persons.

The author retains ownership of the copyright in his/her thesis. Neither the thesis nor substantial extracts from it may be printed or otherwise reproduced with the author's permission.

L'auteur a accordé une licence non exclusive permettant à la Bibliothèque nationale du Canada de reproduire, prêter, distribuer ou vendre des copies de sa thèse de quelque manière et sous quelque forme que ce soit pour mettre des exemplaires de cette thèse à la disposition des personnes intéressées.

L'auteur conserve la propriété du droit d'auteur qui protège sa thèse. Ni la thèse ni des extraits substantiels de celle-ci ne doivent être imprimés ou autrement reproduits sans son autorisation.

0-612-21622-5

UNIVERSITY OF ALBERTA

RELEASE FORM

NAME OF THE AUTHOR : Maher Quraan

TITLE OF THE THESIS : A COINCIDENCE MEASUREMENT
OF THE $D(\gamma, pp\pi^-)$ CROSS SECTION
IN THE REGION OF THE Δ RESONANCE

DEGREE : Doctor of Philosophy

YEAR THIS DEGREE GRANTED : 1997

Permission is hereby granted to the University of Alberta Library to reproduce single copies of this thesis and to lend or sell such copies for private, scholarly or scientific research purposes only.

The author reserves all other publication and other rights in association with the copyright in the thesis, and except as hereinbefore provided neither the thesis nor any substantial portion thereof may be printed or otherwise reproduced in any material from whatever without the author's prior written permission.




Centre for Subatomic Research,
University of Alberta,
Edmonton, Alberta.
T6G 2N5

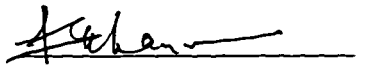
Date : Jan 28, 1997.

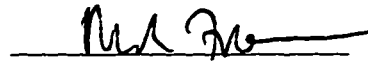
UNIVERSITY OF ALBERTA

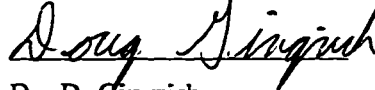
FACULTY OF GRADUATE STUDIES AND RESEARCH

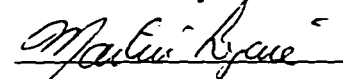
The undersigned certify that they have read, and recommend to the Faculty of Graduate Studies and Research for acceptance, a thesis entitled *A COINCIDENCE MEASUREMENT OF THE $D(\gamma, pp\pi^-)$ CROSS SECTION IN THE REGION OF THE Δ RESONANCE* submitted by MAHER A QURAAN in partial fulfillment of the requirements for the degree of DOCTOR OF PHILOSOPHY in nuclear physics.



Dr. N.L. Rodning (Supervisor)
Professor of Physics



Dr. F.C. Khanna (Chairman)
Professor of Physics


Dr. M. Freeman
Professor of Physics


Dr. D. Gingrich
Professor of Physics


Dr. M. Legare
Professor of Mathematics


Dr. P. Kitching
Professor of Physics


Dr. L. Pilonen (External Reader)
Professor of Physics
Virginia Polytechnic Inst. and State Univ.

Date : Dec 6, 1976 .

ABSTRACT

Photonuclear reactions are excellent means for understanding final state interactions (FSI). The photon interacts only electromagnetically, allowing a clean separation of the strong interaction channels in the final state. The availability of high duty factor electron machines and large acceptance detectors in the past decade have allowed a further investigation of these effects covering wider regions of phase space. In this experiment, we have successfully measured the $D(\gamma, pp\pi^-)$ reaction cross section at the Saskatchewan Accelerator Laboratory (SAL) utilizing the Saskatchewan-Alberta Large Acceptance Detector (SALAD). This is the first measurement of the $\gamma D \rightarrow pp\pi^-$ cross section covering a wide range of phase space with an attempt to study the FSI's and the $\Delta - N$ interaction that has successfully reproduced the normalizations. The Cross section for this reaction is compared to the calculation of J.M. Laget. Laget's theory is quite successful in describing the shapes of the distributions, as well as the overall magnitude of the cross section. The different FSI's and the $\Delta - N$ interaction have an overall effect of 10%-15% on the single differential cross section, with the calculation that includes $\Delta - N$ interaction having the best normalization compared to the data.

ACKNOWLEDGMENTS

I would like to express my sincere appreciation to my supervisor, Professor Nathan Rodning. Nathan has been the perfect supervisor. He has provided a great amount of help and assistance throughout the course of this program. His motivation and encouragement has made this work possible. Working with Nathan has made the years that I spent at the University of Alberta both very educational and enjoyable. Nathan has generously supported me financially through his research grant throughout my years as a graduate student - thanks Nate!

I would like to thank all members of the SALAD collaboration at both the University of Alberta and the University of Saskatchewan. Their joint effort has made this project a success. In particular, I would like to thank Professor Norman Kolb for his numerous contributions to the SALAD project. Norman has always been ready to answer my questions and make valuable comments. He has also been a good source of encouragement. I would also like to thank Professor Elie Korkmaz for his continued interest in this project, and for his valuable comments and suggestions.

The help of my colleague Dr. Evan Hackett is greatly appreciated. The many discussions that we had together as graduate students working on the SALAD project has always been very helpful. Evan has also generously donated his time to explain the far side cartoons which is greatly appreciated! I would also like to thank my colleague Mohammad Hedayatipoor for answering many of my theoretical questions.

I would like to thank the other members of my defense committee (although some of them asked way too many questions)! In particular, I would like to thank Professor Peter Kitching, Professor Douglas Gingrich and my external examiner, Professor Leo Pilonen for their many comments and suggestions. The Help of Professor Faqir Khanna in answering my theoretical questions, and his comments and advice is appreciated.

The help of all the staff at the Centre of Subatomic Research and the Physics Department is appreciated. Special thanks to Professor Helmy Sherif who provided lots of help and advice as the Associate Chairman of the Physics Department. Many thanks to Lynn Chandler and Audrey Schaapman for their help throughout the years.

My family has provided numerous support throughout my undergraduate and graduate programs. Their help, encouragement, and financial support throughout the years has made this work possible. In particular I would like to thank my mom for her love and support, and my sister Maha who is the only one in my family that might actually understand my thesis!

Many thanks to my other colleagues. They have all been a source of encouragement and entertainment (mostly entertainment)! In particular I would like to thank Ariadna Fernandez, Boje Siebels, Peter Damiano and Suresh Pillai for the good times we spent together, Philip Kayal and Norman Buchanan for dragging me out when I'm busy working in my office, and Robert Davis for the many "cool" parties that he invited me to! I would also like to thank my friends Firas Mansour and Mohamad Al-Hawaree for being good friends.

Contents

1	Introduction	1
2	The Experiment	6
2.1	Tagged Photon Beam	6
2.1.1	Photon Beam	6
2.1.2	SAL Tagger	9
2.1.3	Collimation and Shielding	11
2.1.4	Beam Flux	13
2.2	Gas Target Cell	16
2.3	The Detector	16
2.3.1	Wire Chambers	17
2.3.1.1	ADC Pedestals	20
2.3.1.2	High Voltage Calibrations	21
2.3.1.3	Position Calibrations	21
2.3.1.4	Angular Resolutions	25
2.3.2	Calorimeter	26
2.3.2.1	Scintillator Thresholds	26

2.3.2.2	PMT High Voltage Calibrations and Gain Measurements	29
2.3.2.3	Light Output Corrections	32
2.3.2.4	Energy Resolution	34
2.4	Trigger and Data Acquisition	34
2.4.1	Trigger Electronics	34
2.4.2	Data Acquisition	38
3	Theory	40
3.1	Introduction	40
3.2	Laget's Model	40
3.3	Calculation of the $\gamma D \rightarrow pp\pi^-$ Reaction Cross Section	45
3.3.1	The Single Nucleon Term	47
3.3.2	Rescattering Effects	56
3.3.2.1	$\pi - N$ Rescattering	56
3.3.2.2	$N - N$ Rescattering	60
3.3.3	Two-loop Diagrams	65
3.3.4	The $\Delta - N$ Interaction	65
4	Analysis	69
4.1	Data Analysis	70
4.1.1	Track Reconstruction	70
4.1.2	Particle Identification	75
4.1.3	Event Selection	88
4.2	Monte Carlo Simulations	92

5	Results	106
5.1	Calculation of the $D(\gamma, pp\pi^-)$ cross section	106
5.1.1	Experimental Yield	108
5.1.2	Photon Beam Flux	109
5.1.3	Target Density	110
5.1.4	Detector Efficiency	112
5.2	$D(\gamma, pp\pi^-)$ Cross Section	114
5.2.1	Systematic Errors	119
5.3	Comparison to Theory	120
6	Summary and Conclusions	126

List of Tables

2.1	Applied high voltages and measured leakage currents on the four SALAD wire chambers during the $D(\gamma, pp\pi^-)$ experiment.	21
2.2	Wires excluded from the $D(\gamma, pp\pi^-)$ analysis.	25
4.1	Distribution of track multiplicities found in a typical $D(\gamma, pp\pi^-)$ run. . .	73
4.2	Particles emitted as a result of the π^- absorption process on ^{12}C [20]. . .	86
4.3	Types of $D(\gamma, pp\pi^-)$ events analyzed, and the results of the analysis. All events have three tracks and three ΔE signals. The average χ^2 is computed from values between zero and 10.	90
4.4	Final cuts imposed on the remaining $D(\gamma, pp\pi^-)$ events and the percentage of events remaining after each successive cut is applied.	92
5.1	List of variables used to calculate the $D(\gamma, pp\pi^-)$ cross section. The range for each variable was divided into 10 bins.	109
5.2	Number of photons N_γ ($\times 10^9$) determined from the fits of the bremsstrahlung distribution.	110
5.3	Sources of systematic errors and there contribution to the total systematic error.	120

List of Figures

2.1	Electron Linear Accelerator and Pulse Stretcher Ring at the Saskatchewan Accelerator Laboratory.	8
2.2	Experimental Setup for the $D(\gamma, pp\pi^-)$ experiment performed in June 1992.	10
2.3	SALAD-tagger coincidences to tagger sum ratio, and electron to proton ratio for different positions of the first collimator. The solid curve is drawn to guide the eye.	12
2.4	Tagging efficiency measurements performed during the $D(\gamma, pp\pi^-)$ experiment.	15
2.5	End View of the SALAD Detector.	18
2.6	Side view of the SALAD Detector.	19
2.7	Sum of the charge deposited in the wire chambers for three track $D(\gamma, pp\pi^-)$ events.	22
2.8	Support structure for the wire chambers.	24
2.9	Position histogram for the radioactive source located at the center of a wire.	27
2.10	SALAD resolution of the scattering angle θ	28

2.11	Limits on pion and proton energies detectable in the SALAD scintillators as a function of the scattering angle θ	30
2.12	Scintillator gain versus time for a) a typical E scintillator and b) a typical ΔE scintillator. The data points are determined from cosmic ray data: the solid line is a linear fit.	33
2.13	Energy resolution of the SALAD scintillators. The top plot is for the ΔE scintillators, and the bottom plot is for the E scintillators. The solid line is a fit to the data.	35
2.14	SALAD scintillator's circuitry and trigger logic.	36
3.1	Feynman diagrams for the two body disintegration of the deuteron.	43
3.2	Total photoabsorption cross section on deuterium. The experimental points are a compilation from several experiments as plotted in reference [29]. The theoretical curves are calculated by J.M. Laget [29]. The dashed curves include only the quasi-free diagram, whereas the solid curve includes rescattering effects as well.	44
3.3	Feynman diagrams for the reaction $\gamma p \rightarrow n\pi^+$	45
3.4	Total cross sections for single and double pion photoproduction on protons. The experimental data is a compilation from two experiments as plotted in reference [27]. The theoretical curves are calculated by J.M. Laget [27]. The dashed curve includes the Born terms, whereas the solid curve allows for the excitation of a Δ resonance.	46
3.5	Feynman diagrams for $\gamma D \rightarrow pp\pi^-$	48

3.6	Experimental yield for $\gamma D \rightarrow pp\pi^-$. The experimental points are obtained at DESY by Benz et al. [4]. The theoretical curves are calculated by J.M. Laget [27]. The dashed curve includes only the quasi-free diagram. The solid curve includes rescattering effects as well.	53
3.7	Deviations from the spectator nucleon model for $\gamma D \rightarrow pp\pi^-$ at a spectator nucleon momentum of 50 MeV/c. The experimental data are obtained at Saclay by Argan et. al. [2]. The theoretical curves are calculated by J.M. Laget [25].	54
3.8	Deviations from the spectator nucleon model for $\gamma D \rightarrow pp\pi^-$ at a spectator nucleon momentum of 400 MeV/c. The experimental data are obtained at Saclay by Argan et al. [3]. The theoretical curves are calculated by J.M. Laget [3]. The solid curve includes $\pi - N$ rescattering, whereas the dot dashed curve includes meson exchange currents as well.	55
3.9	Scattering cross section for $\gamma n \rightarrow p\pi^-$ as extracted from the $\gamma D \rightarrow pp\pi^-$ reaction cross section at a spectator nucleon momentum of 50 MeV/c. The experimental points are obtained at Saclay by Argan et al. [2] The theoretical curves are calculated by J.M. Laget [25].	57
3.10	Meson exchange Feynman diagrams for $\gamma D \rightarrow pp\pi^-$	60
3.11	Deviations from the spectator nucleon model for $\gamma D \rightarrow pp\pi^-$ at a spectator nucleon momentum of 550 MeV/c. The experimental data are obtained at Saclay by Argan et. al. [3]. The theoretical curves are calculated by J.M. Laget [3]. The solid curve includes $\pi - N$ rescattering, whereas the dot dashed curve includes meson exchange currents as well.	61

3.12	Differential cross section for $\gamma D \rightarrow pp\pi^-$ reaction. The experimental data are obtained at Saclay by Ardiot et al. [28]. The theoretical curves are calculated by J.M. Laget [28]. The dashed curve includes only the quasi-free diagram, whereas the solid curve includes $N - N$ rescattering as well.	63
3.13	Differential cross section for $\gamma D \rightarrow nn\pi^+$ reaction. The experimental data are obtained at Saclay by Ardiot et al. [28]. The theoretical curves are calculated by J.M. Laget [28]. The dashed curve includes only the quasi-free diagram, whereas the solid curve includes $N - N$ rescattering as well.	64
3.14	Feynman diagrams for the $\Delta - N$ interaction.	66
4.1	A typical reconstructed three track $D(\gamma, pp\pi^-)$ event as seen in SALAD.	72
4.2	Vertex definition for two track events.	74
4.3	The z position of the vertex for events with track multiplicities ≥ 1 from a typical $D(\gamma, pp\pi^-)$ run.	76
4.4	A θ versus z plot for events with track multiplicity ≥ 1 from a typical $D(\gamma, pp\pi^-)$ run.	77
4.5	The z position of the vertex for three track $D(\gamma, pp\pi^-)$ events after the final cuts are applied. The solid histogram is a Monte Carlo simulation.	78
4.6	Radial position of the vertex for three track $D(\gamma, pp\pi^-)$ events. The top plot was obtained before the final cuts were applied. The bottom plot was obtained after the final cuts were applied. The solid histogram is a Monte Carlo simulation.	79

4.7	Average minimum distance between outgoing tracks for three track $D(\gamma, pp\pi^-)$ events after the final cuts are applied. The solid histogram is a Monte Carlo simulation.	80
4.8	Stopping power as a function of energy for protons and pions as calculated from the Bethe-Bloch formula.	83
4.9	Stopping power versus energy for three track $D(\gamma, pp\pi^-)$ events before applying the cuts.	84
4.10	Linearized stopping power histogram for three track $D(\gamma, pp\pi^-)$ events before applying the cuts. The first peak corresponds to electrons, the small bump (at about 0.3) is due to pions, whereas the second peak is due to protons.	85
4.11	Pion's linearized stopping power histogram for three track $D(\gamma, pp\pi^-)$ events after applying the cuts. The top plot compares the data to a Monte Carlo simulation that does not take π^- absorption into account. The bottom plot compares the same data to a Monte Carlo simulation that accounts for π^- absorption.	87
4.12	Stopping power versus energy for three track $D(\gamma, pp\pi^-)$ events after the final cuts were applied. The figure in the top right corner is a linearized stopping power histogram.	89
4.13	A schematic summary of the analysis showing the different types of $D(\gamma, pp\pi^-)$ events analyzed.	93

4.14	χ^2 distributions for $D(\gamma, pp\pi^-)$ candidates with three tracks and three ΔE signals which were not used in this analysis. Figure (a) is for events with one E pion signal, Figure (b) is for events with one E proton signal, and Figure (c) is for events with two E proton signals.	94
4.15	χ^2 distributions for $D(\gamma, pp\pi^-)$ candidates considered in the remaining part of the analysis. These events include three track events with three ΔE signals, and either three E or two E proton-pion signals. A cut is imposed at $\chi^2 = 3$ to eliminate the remaining background. The solid histogram is a Monte Carlo simulation.	95
4.16	Photon energy distribution generated by the SALAD Monte Carlo to simulate a bremsstrahlung distribution. The bremsstrahlung cross section is obtained from Schiff [40], and calculated at an electron energy of 284 MeV for the top plot and 290 MeV for the bottom plot, corresponding to the two electron energies at which the experiment was conducted. . .	97
4.17	Efficiencies of the four SALAD wire chambers.	98
4.18	Shift in proton energy due to strong interactions in plastic scintillators. The distribution is obtained from the GEANT simulation package GHEISHA. A log scale was used to show the tail of the distribution. The number of protons that deposit a different amount of energy than expected due to nuclear interactions is 0.37%.	100
4.19	Shift in pion energy as a result of absorption in the SALAD scintillators.	102
4.20	Pion lifetime distribution in units of the pion mean life $\tau (= 2.60 \times 10^{-8} s)$.	104

5.1	A schematic diagram of the $D(\gamma, pp\pi^-)$ reaction showing the intermediate process resulting in the creation of the $\Delta(1232)$ resonance and its subsequent decay. The definition of the kinematic variables used to calculate the cross section are also shown on the plot.	107
5.2	Bremsstrahlung photon energy distribution fitted to the tagger counting rates. The plots correspond to a maximum electron energy of 284 and 290 MeV for the top and the bottom plot, respectively.	111
5.3	Single differential cross section for $D(\gamma, pp\pi^-)$ in terms of (a) the pion's azimuthal angle and (b) the pion's scattering angle as measured using SALAD. Both angles are calculated in the Δ rest frame, where the direction of the Δ defines the z-axis.	115
5.4	Single differential cross section for $D(\gamma, pp\pi^-)$ in terms of (a) the Δ scattering angle and (b) the $p-\pi^-$ invariant mass as measured using SALAD. The Δ scattering angle is calculated in the $\gamma - D$ centre of mass frame, where the direction of the photon defines the z-axis.	116
5.5	$D(\gamma, pp\pi^-)$ cross section as a function of beam energy measured using SALAD. The bottom plot is the total cross section in the measured region plotted at the centre of that region.	117
5.6	Single differential cross section for $D(\gamma, pp\pi^-)$ in terms of (a) the pion's azimuthal angle and (b) the pion's scattering angle as measured using SALAD. Both angles are calculated in the Δ rest frame, where the direction of the Δ defines the z-axis. The theoretical curves are calculated by J.M. Laget and corrected for the efficiency of SALAD.	122

5.7	Single differential cross section for $D(\gamma, pp\pi^-)$ in terms of (a) the Δ scattering angle and (b) the $p-\pi^-$ invariant mass as measured using SALAD. The Δ scattering angle is calculated in the $\gamma - D$ centre of mass frame, where the direction of the photon defines the z-axis. The theoretical curves are calculated by J.M. Laget and corrected for the efficiency of SALAD.	123
5.8	$D(\gamma, pp\pi^-)$ cross section as a function of beam energy measured using SALAD. The bottom plot is the total cross section in the measured region plotted at the centre of that region. The theoretical curves are calculated by J.M. Laget and corrected for the efficiency of SALAD.	124

Chapter 1

Introduction

The photodisintegration of the deuteron above the pion production threshold has been of particular interest since the early 1960's. While many experiments on the photoproduction of neutral and positive pions off protons have been performed leading to a good understanding of such processes, experiments on the photoproduction of negative pions off neutrons are scarce. Since construction of neutron targets is not practical, two other methods have been used. The first method is to measure the cross section of the inverse reaction, the radiative pion capture by protons. The dynamics of this process is equivalent to the direct reaction if time reversal is assumed. The interest in testing the time reversal invariance, however, lead to the interest in measuring the direct reaction cross section [37].

The other method is to use a deuterium target. Since the deuteron is a loosely bound system, neutrons may be considered to be approximately free. This is known as the spectator model in which the photon is assumed to be completely absorbed by the neutron, while the proton does not participate in the reaction but remains there as a

spectator carrying its original Fermi energy and momentum.

Most of the $\gamma n \rightarrow p\pi^-$ cross sections were extracted from the $\gamma D \rightarrow pp\pi^-$ reaction cross sections in the framework of the spectator model. In some cases, cuts were made to exclude regions of the phase space for which deviations from the spectator model are expected to be large. In other cases some of the corrections related to the use of a deuterium target were considered in doing the extraction [37, 39, 4]. The analyses of these experiments are model dependent and since, among other factors, the effects of final state interactions were little known, the controversial results of such experiments were not particularly surprising. Moreover, most of these experiments suffered from at least one of the following experimental limitations:

- (1) The use of bremsstrahlung beams which resulted in a relatively large overall uncertainty in the normalization.
- (2) Poor energy resolutions of about 40-50 MeV, particularly in the bubble chamber experiments.
- (3) Explorations limited to certain regions of the phase space.
- (4) Poor statistics.
- (5) Incomplete determination of final state kinematics.

While early interest in the $\gamma D \rightarrow pp\pi^-$ reaction stemmed from the interest in the $\gamma n \rightarrow p\pi^-$ reaction and, hence, focused on the regions of phase space in which the spectator model was expected to be valid, recent interest has been devoted to understanding final state interactions (FSI) away from the region where the quasi-free process is dominant. Although FSI's have been studied in many reaction processes, $\gamma D \rightarrow pp\pi^-$ offers a unique system. One such advantage is that photonuclear reactions involve only an electromagnetic interaction in the initial state. Since the electromagnetic interaction is

well understood, no ambiguity arises from the initial state, allowing a clean separation of the FSI's. This is in contrast to hadronic induced reactions where strong interactions occur in both initial and final states. Another advantage is in the use of a deuterium target as opposed to heavier nuclei. The deuteron is the simplest bound state and its wave function is well understood. In addition, the deuteron is disintegrated altogether, and hence no ambiguity arises from the propagation of the outgoing particles in a nuclear medium. The presence of only three particles in the final state provides another advantage. On one hand, the limited number of possible interactions allows for detailed microscopic calculations including different ingredients of FSI's. On the other hand, the presence of three particles in the final state (as opposed to two) provides more freedom in the choice of the regions of phase space to focus on and study.

Of the different FSI's that may occur in this process, the $\Delta - N$ interaction is the least understood. The experimental difficulty in studying this interaction arises from the fact that the Δ is an unstable particle. The Δ is created in the intermediate process and decays via the strong interaction:

$$\gamma D \rightarrow p\Delta \rightarrow pp\pi^- \quad (1.1)$$

The lifetime of the Δ is very short (width, $\Gamma = 115$ MeV; mean life, $\tau = 6 \times 10^{-24}$ s), and the only way to get to the $\Delta - N$ interaction is through that very short lived intermediate process. On the theoretical side calculating a $\Delta - N$ interaction imposes a challenge as well. While calculating a two-body interaction is relatively simple, the Δ , being a $\pi - N$ resonance, is a composite particle. Its interaction with the nucleon is thus a relativistic three-body problem which is quite hard to solve. Few calculations have been put forward to investigate this interaction with limited success for two reasons.

On the theoretical side, only approximate solutions have been considered where the Δ is treated as a stable particle, with the width of the Δ taken into account in some cases. On the experimental side, the amount of data available is limited, and confined to specific reactions. There is definite need for both, detailed theoretical calculations of the $\Delta - N$ interaction, as well as experimental data from various reaction mechanisms to allow for definite conclusions and consistency checks.

In order to study such interactions in more detail, experiments with high statistical accuracy are required for which final state kinematics are completely determined. The difficult task of obtaining a reasonable number of counts is due to the small cross sections of photon induced reactions which are typically $\sim 1/100$ times smaller than those for hadron induced reactions, and due to the limitation on the photon beams available. Until recently most machines suffered from low tagged photon fluxes ($\sim 10^5$ Hz) and very small duty factors ($< 2\%$). In addition to the difficulty of obtaining enough statistics that such limitations imply, small duty factors result in a reduced signal to background ratio. Moreover, since coincidence experiments are required for a complete determination of final state kinematics, discrete detectors impose serious limitations on statistics.

In the past decade, considerable experimental progress has been achieved. Electron machines with duty factors up to 100% were built and used in conjunction with high flux photon taggers. The experiment described here was performed at the Saskatchewan Accelerator Laboratory (SAL) which can achieve duty factors of nearly 100%. Outgoing charged particles were detected in coincidence using the Saskatchewan-Alberta Large Acceptance Detector (SALAD). The high duty factor SAL machine and the SALAD detector are described in some detail in the next chapter.

Theoretical calculations may be made using a diagrammatic approach. Each transition amplitude may be expanded in terms of a few relevant Feynman diagrams. Although this method is completely relativistic, appropriate non-relativistic approximations may be made at medium and low energies to simplify the calculations. This method has been used by J. M. Laget in the analysis of final state interactions and has been quite successful in reproducing a large body of experimental data. A detailed description of the calculation is given in the third chapter.

Detailed comparisons of the data to theoretical calculations allow an understanding of final state interaction effects. The calculation may include different ingredients of final state interactions, and the final state kinematics may be chosen so as to focus on the final state interaction of interest. This method has proved to be successful, and several final state interactions have been explored in this fashion. A detailed description of the data analysis is presented in the fourth chapter, and comparisons of the data obtained in the experiment considered here to such calculations are presented in the fifth chapter.

SALAD has been a useful device in the investigation of many other reactions as well. Since it has been stationed at SAL, several experiments have been performed on D_2 , 3He , 4He and ^{12}C targets. Most of the data has been analyzed, and some have already been published [21, 22, 17].

Chapter 2

The Experiment

This experiment was performed at the Saskatchewan Accelerator Laboratory (SAL), located at the University of Saskatchewan. SAL provides a high duty factor electron beam with an energy in the region of the Δ resonance. The data were taken in June 1992, using the Saskatchewan-Alberta Large Acceptance Detector (SALAD). The details of the Saskatchewan accelerator and SALAD are presented in this chapter, as well as the calibration measurements performed during this experiment.

2.1 Tagged Photon Beam

2.1.1 Photon Beam

The SAL linear accelerator (linac) consists of six radio-frequency cavities that accelerate electrons up to an energy of 300 MeV. The linac produces a pulsed beam with a 2.5 μ s duration, and a duty factor of 0.03%, where the duty factor is given by

$$\eta = \frac{\langle I \rangle^2}{\langle I^2 \rangle}. \quad (2.1)$$

where I is the beam intensity. Since photonuclear reactions have inherently low cross sections, a high duty factor is desirable to obtain statistically significant data over a reasonable period of time. In addition, a high duty factor results in an improved signal to noise ratio. Pulse stretcher rings (PSR) have been used in the past decade to increase the duty factor of linear accelerators to over 85% [23]. The earliest PSR successfully achieving high duty factors was designed and built at the University of Saskatchewan, and has been operating since the late 1980's, increasing the duty factor of the linac from 0.03% to over 65%. The experimental program started in the summer of 1988 [10].

The pulse stretcher ring of the University of Saskatchewan has a total length of 108.78 m, with dimensions of 50.49 m by 6.64 m as dictated by the constraints of a pre-existing building. It consists of two 180° bend regions connected by two straight sections, as shown in Figure 2.1. The linac accelerates electrons up to a maximum energy of 300 MeV. The beam is then injected into one of the straight sections of the PSR. The energy of the beam in the PSR is maintained using a radio frequency system. The beam may be extracted from the straight section opposite to the injection region. The change in tune is achieved through synchrotron radiation losses as electrons pass through the bend regions of the PSR [10, 24, 41].

For this experiment, technical difficulties resulted in a reduced duty factor that averaged at approximately 44%. The duty factor as a function of time was monitored during each run, and the beam was tuned whenever needed to ensure a high duty factor. The electron energy achieved was 290 MeV for the first set of runs and 284 MeV for the remaining set.

The electron beam travels through the extraction line and passes through a 15 μm thick aluminum radiator as shown in Figure 2.2, and results in producing a photon beam

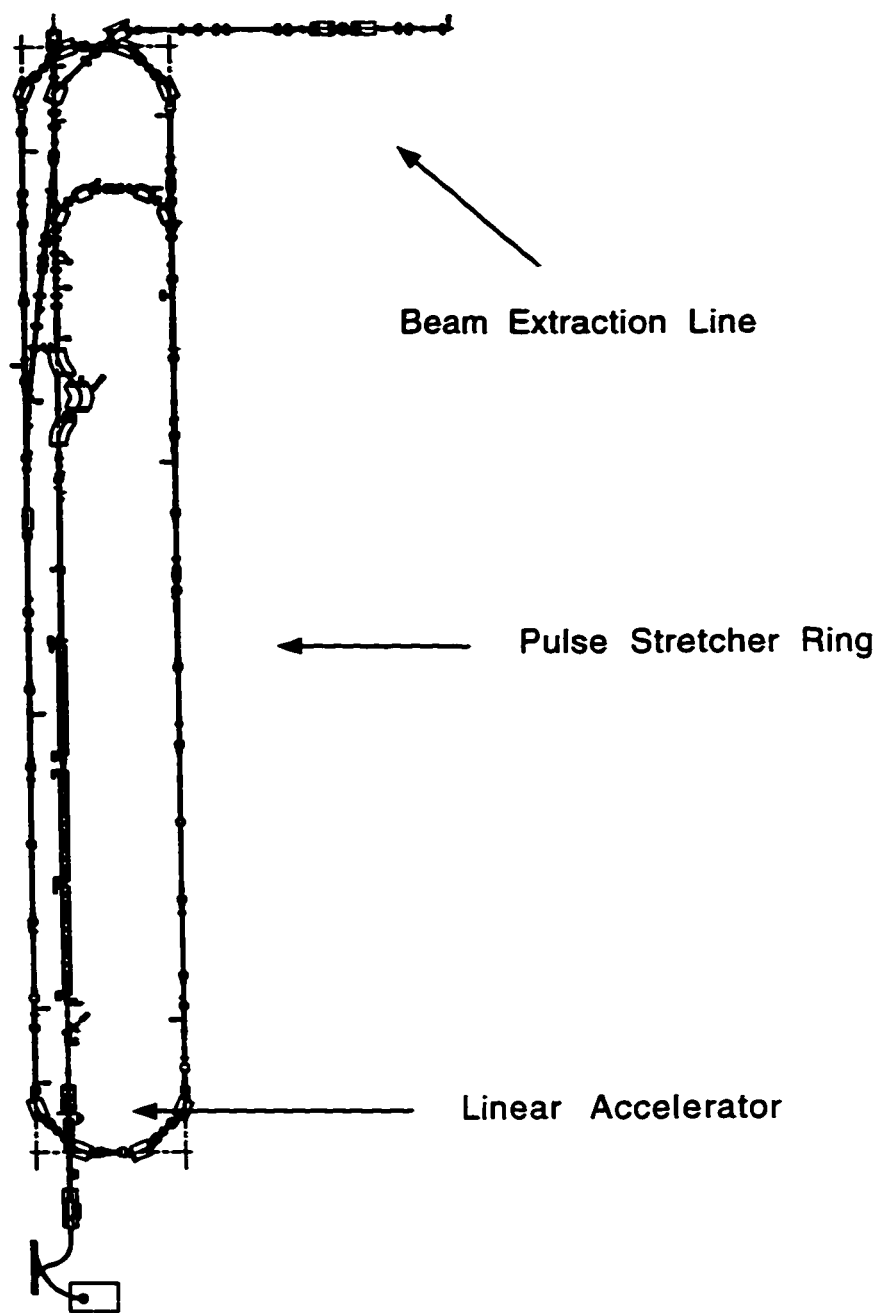


Figure 2.1: Electron Linear Accelerator and Pulse Stretcher Ring at the Saskatchewan Accelerator Laboratory.

by bremsstrahlung. The resulting photon beam has an intensity of 10^7 photons/s. The beam then emerges from the vacuum into air through an exit window which consists of a 0.5 mm thick Al foil and 0.125 mm thick kapton foil.

The electron beam is momentum analyzed in a magnetic field. Electrons that radiate photons in the selected energy range are bent so as to hit a 62-channel focal plane detector (tagger). The energy of the associated photon is determined from the radius of curvature of the recoil electron. For an electron of energy E_e incident on the radiator, the photon energy E_γ is given by

$$E_\gamma = E_e - E'_e, \quad (2.2)$$

where E'_e is the energy of the recoil electron. Electrons that do not radiate photons in the tagged region are dumped out through an opening in the left side of the experimental area (as seen by the beam) using a sweeping magnet. Lead bricks shield the focal plane from backgrounds associated with the dumped beam.

2.1.2 SAL Tagger

The photon tagging system consists of the above mentioned analyzing magnet and a 62-channel focal plane detector. The focal plane detector is made up of 63 3.2 mm thick plastic scintillators. The scintillators are arranged in two overlapping rows. In order to reduce backgrounds associated with the tagger, a coincidence is required between a front row and a back row scintillator. The two rows are offset by half a scintillator to allow for a better energy resolution. Due to this offset the 63 counters result in a 62 channel tagger. This allows the tagging of photons with energies in the range 187-229 MeV. and a resolution of ~ 0.6 MeV [36, 42]. The tagged energy range may be changed by changing the magnetic field of the analyzing magnet or the electron energy. The upper

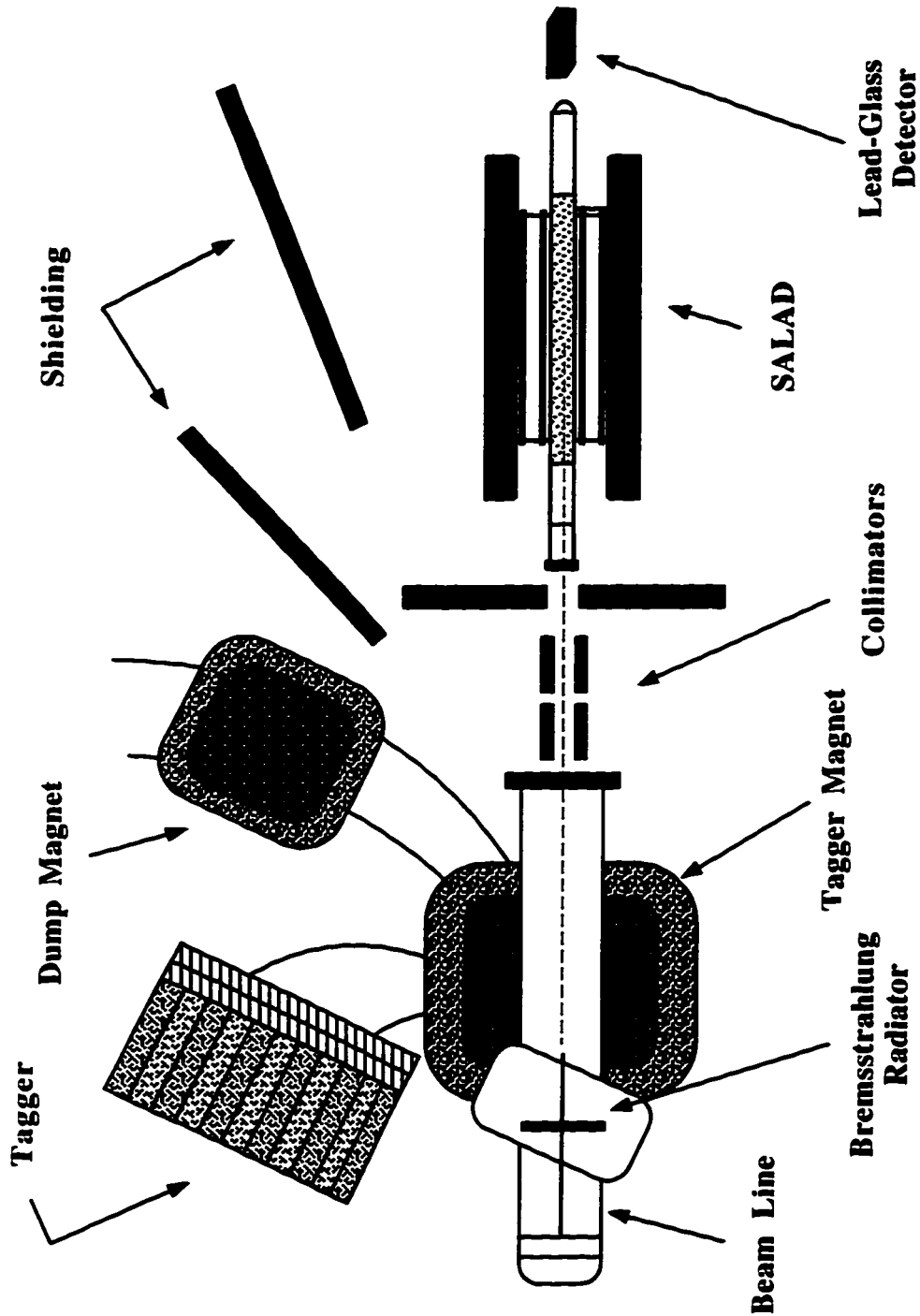


Figure 2.2: Experimental Setup for the $D(\gamma, pp\pi^-)$ experiment performed in June 1992.

limit of 229 MeV tagged photon energy, however, is dictated by the magnet geometry and cannot be exceeded.

The tagger serves two purposes: it allows the determination of the photon energy, and the determination of the photon flux required for calculating the cross section. In this experiment, only events that result in three signals in the SALAD calorimeter were analyzed. Such events result from photons with energies above that of the tagger range. Since these events are overdetermined, the photon energy is determined from the kinematics. The tagger is useful, however, in the photon flux determination. While direct measurement of the photon flux is not possible, the photon flux in the tagged region may be extrapolated using a bremsstrahlung distribution to determine the flux in the untagged region. The details of this are discussed in section 5.1.2.

2.1.3 Collimation and Shielding

The bremsstrahlung photon beam was collimated using two 12.6 cm long lead collimators of 15 and 20 mm diameter. The horizontal positions of these two collimators are computer controlled. Several tests were performed in order to fine-tune the collimator positions. The best alignment for the first collimator was first determined and the relative position of the second collimator was subsequently determined while fixing the first in place. Since electrons and positrons may be produced by the beam hitting the edge of a collimator, the best alignment was determined by minimizing both the ratio of the total coincidences (between SALAD and the tagger) to the tagger sum, and the electron to proton ratio. Figure 2.3 shows a typical plot.

A clean-up magnet was placed downstream of the collimators to deflect secondary electrons produced on the collimators. Several trial runs were performed with this

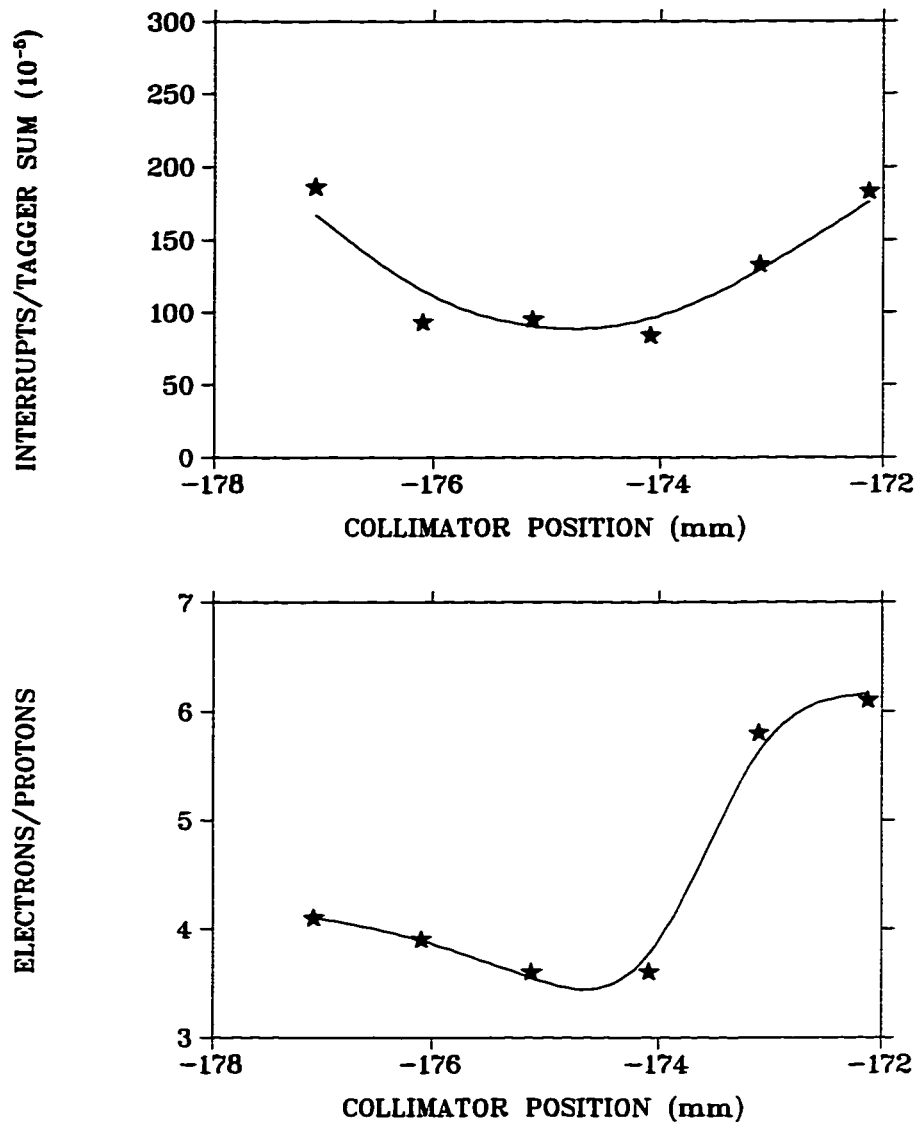


Figure 2.3: SALAD-tagger coincidences to tagger sum ratio, and electron to proton ratio for different positions of the first collimator. The solid curve is drawn to guide the eye.

magnet off or on with a field of 3.0 kG. Results showed no improvement in the interrupts to tagger sum ratio or in the electron to proton ratio with the magnet on. The clean-up magnet was turned off for all $D(\gamma, pp\pi^-)$ data runs.

A lead wall 9 cm thick was placed between the clean-up magnet and the upstream end of SALAD to provide shielding from backgrounds associated with the beam dump. A third collimator 13.3 cm long of 30 mm diameter was fitted into a hole in the lead wall to allow the beam to pass through. This collimator size was chosen to be large enough such that the primary collimated beam was not affected. SALAD was aligned so that its axis coincided with that of the beam.

To further reduce the background, a 26.0 cm long, 2.32 cm thick removable lead shielding tube was designed with an outside diameter of 12.1 cm and was mounted at the upstream end of SALAD as shown in Figure 2.6. While the shielding is expected to reduce the background, a quantitative estimate of this reduction was not determined since the shielding was used in all runs due to difficulty in removal.

2.1.4 Beam Flux

In order to determine the incident photon flux, tagging efficiency measurements are required. The incident photon flux cannot be directly determined from the counting rates of the tagger for two reasons. First, background electrons may be detected by the tagger which do not originate from the radiator and hence do not correspond to tagged photons. Secondly, the use of collimators results in cutting part of the photon beam. Electrons that radiate photons may thus be detected by the tagger, while the associated photons may not make it into the target region.

The tagging efficiency was measured using a lead-glass detector. The lead-glass de-

detector was placed behind the downstream end of SALAD. The cross sectional area of the lead-glass detector was bigger than that of the collimated beam. The number of tagged photons, N_γ , is measured by requiring a coincidence between the lead-glass detector and the tagger. A background correction is made by repeating the same measurement with the radiator removed. The tagging efficiency, η_{tag} , is then given by

$$\eta_{tag} = \frac{N_\gamma - \frac{\tau}{\tau'} N'_\gamma}{N_{tag} - \frac{\tau}{\tau'} N'_{tag}}, \quad (2.3)$$

where N_γ is the number of tagged photons with the radiator in. N'_γ is the number of coincidences between the lead-glass detector and the tagger with the radiator removed. N_{tag} (N'_{tag}) is the tagger channel sum with the radiator in (out), and τ (τ') is the time of the measurement with the radiator in (out).

Tagging efficiency measurements were carried out at a much lower photon flux rate than production runs to avoid damage to the lead-glass detector; the tagging efficiency, however, is flux independent. After tagging efficiency measurements were made, the high voltage on the lead-glass detector was turned off and the detector was moved away from the beam line under computer control. Several tagging efficiency measurements were performed during this experiment. The background ratio (N'_γ/N'_{tag}) in these measurements was typically less than 0.5%, and the time ratio (τ/τ') was of the order of one. As may be seen from Figure 2.4, the tagging efficiencies fall into two groups, averaging around 49% and 56% (summed over the 62 tagger channels). The shift in tagging efficiency was due to a major tuning of the beam. Due to this shift, the cross section was calculated separately for the data obtained before and after the beam tuning.

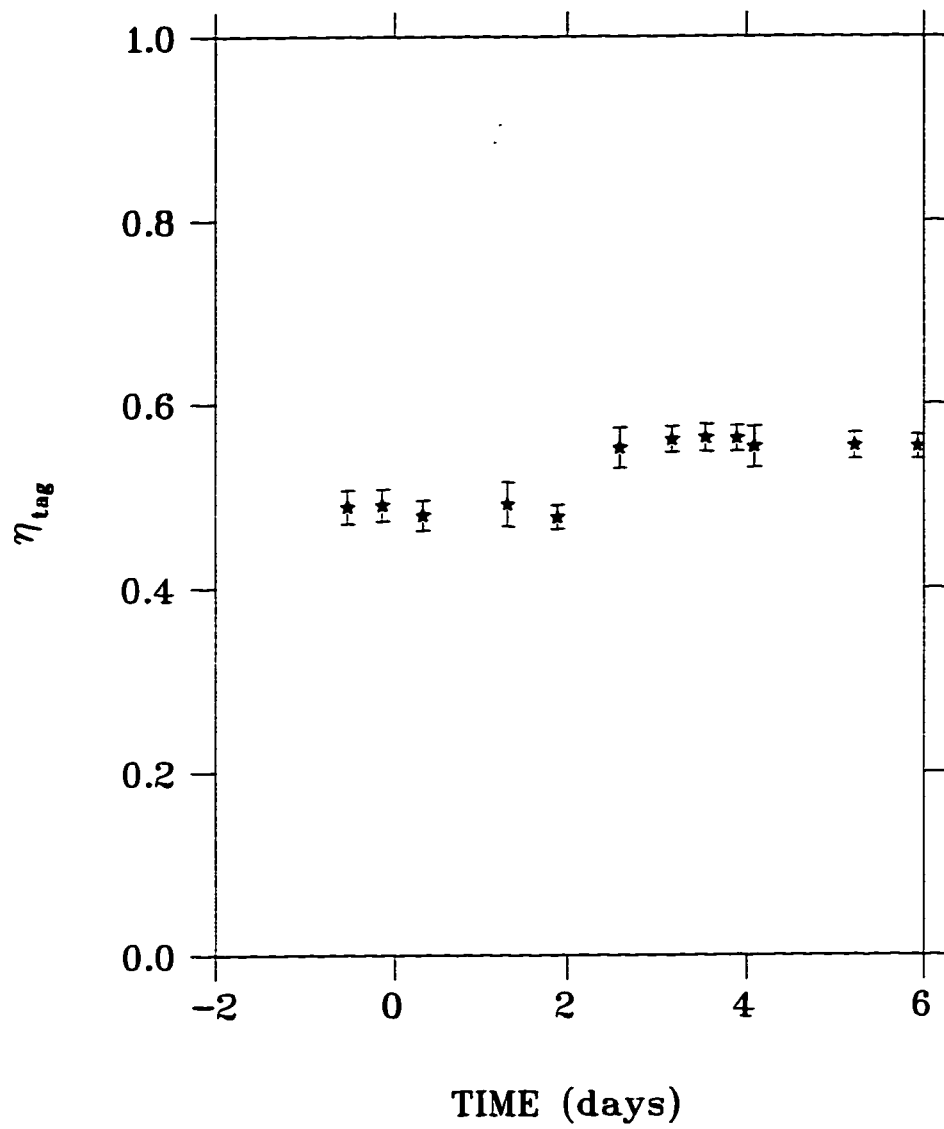


Figure 2.4: Tagging efficiency measurements performed during the $D(\gamma, pp\pi^-)$ experiment.

2.2 Gas Target Cell

Small counting rates are expected from photonuclear reactions due to typically small cross sections. A target should therefore be carefully designed so as to optimize the counting rate. Since the counting rate is proportional to the number of target particles per unit area, a large areal thickness would optimize the counting rate in SALAD. On the other hand, the radial thickness of the target should be small to reduce the energy lost by scattered particles inside the target, and allow such particles to be detected.

The target used in this experiment is a pressurized cylinder with overall length of 237 cm and an inner radius of 5.05 cm. The main portion of the target is made up of 208.3 cm long mylar lined carbon fiber tubing. Two 33.020 cm long \times 0.079 cm thick aluminum tubes are inserted into each end of the fiber tubing. An aluminum flange and an aluminum dome are attached to the upstream and downstream ends of this assembly, respectively. The flange is used to mount a mylar window. A 60 cm long section of this mylar lined carbon fiber tubing has been tested to a pressure of In this experiment, the target was filled with deuterium gas at room temperature with an initial absolute pressure of 6.99 atmospheres. Small amounts of leakage caused the absolute pressure to drop to 6.42 atmospheres at the end of the one week long production run. The target is described in detail elsewhere [7, 30].

2.3 The Detector

An end view of SALAD is shown in Figure 2.5. The gas target cell is mounted in the center of the detector with its axis parallel to that of SALAD. The target may be inserted or removed at any time during the experiment. Surrounding the target are

two inner wire chambers each containing 36 wires followed by two outer wire chambers each containing 72 wires. The wire chambers are 120 cm long, and are labeled 1 to 4 starting from the innermost chamber. The wire chambers are surrounded in turn by the calorimeter, an assembly of 24 $\Delta E - E$ scintillation counter pairs. The overall diameter of the detector is 75 cm. A side view of the SALAD detector is shown in Figure 2.6. The detector's design and calibration are described in detail elsewhere [7, 30].

2.3.1 Wire Chambers

All the wires in the four chambers are aligned parallel to the detector axis. The 36 wires in chambers 1 and 2 are 10° apart. The wires are staggered by half a cell so that wire #1 in chamber 1 is positioned at a ϕ angle of 10° while wire #1 in chamber 2 is positioned at an angle of 5° . The 72 wires in chambers 3 and 4 are 5° apart, and staggered by half a cell. Wire #1 in chamber 3 is at an angle of 5° while that in chamber 4 is at an angle of 2.5° . The wire chambers are used to provide a three dimensional position determination of passing charged particles, using charge division to obtain the z coordinate of the hit.

The chambers operate on the principle of charge division and are operated in the self-quenching streamer (SQS) mode [6]. The chambers are filled with a mixture of 70% isobutane gas (C_4H_{10}) and 30% Argon by volume. Argon provides a high charge gain due to gas multiplication, while isobutane absorbs the ultraviolet photons that cause the discharge to propagate along the wire, thus localizing the position of charge deposition on the wire. This allows operation with high gain and good resolution.

The support structure of the wire chambers is shown in Figure 2.8. The walls of the wire chambers are made up of low density polyurethane. This reduces the energy loss

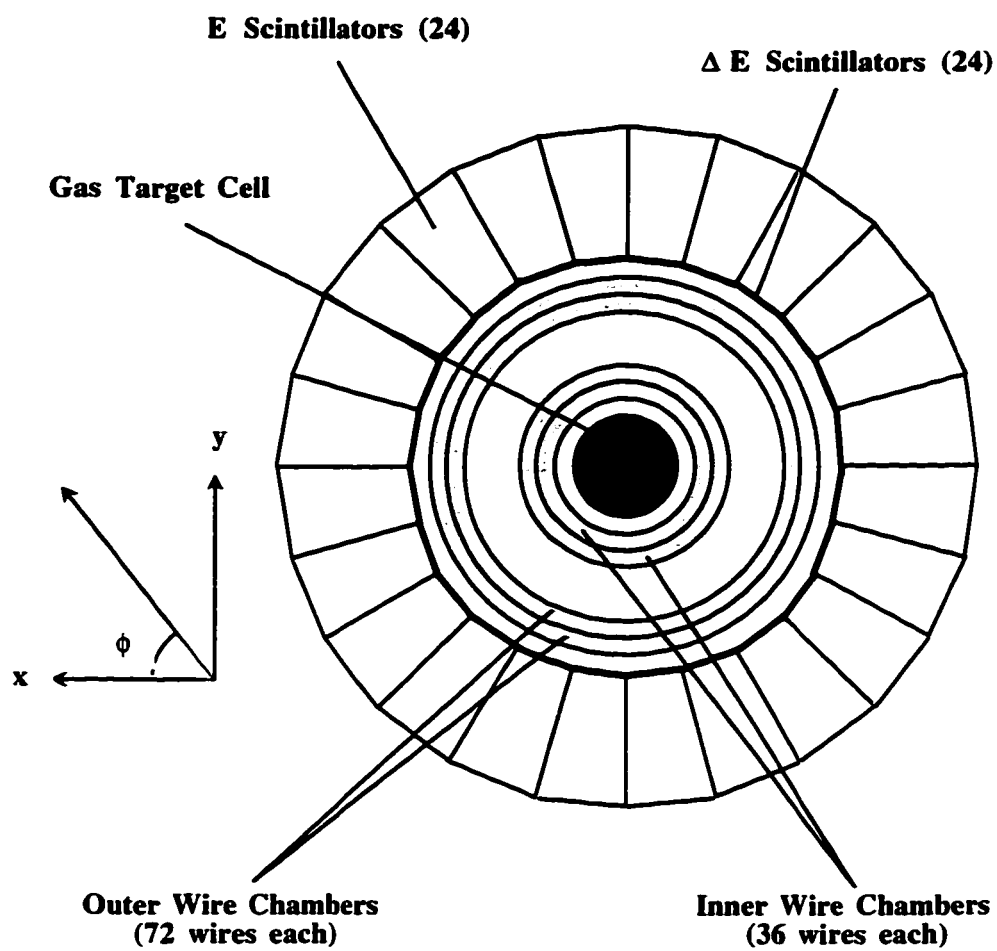


Figure 2.5: End View of the SALAD Detector.

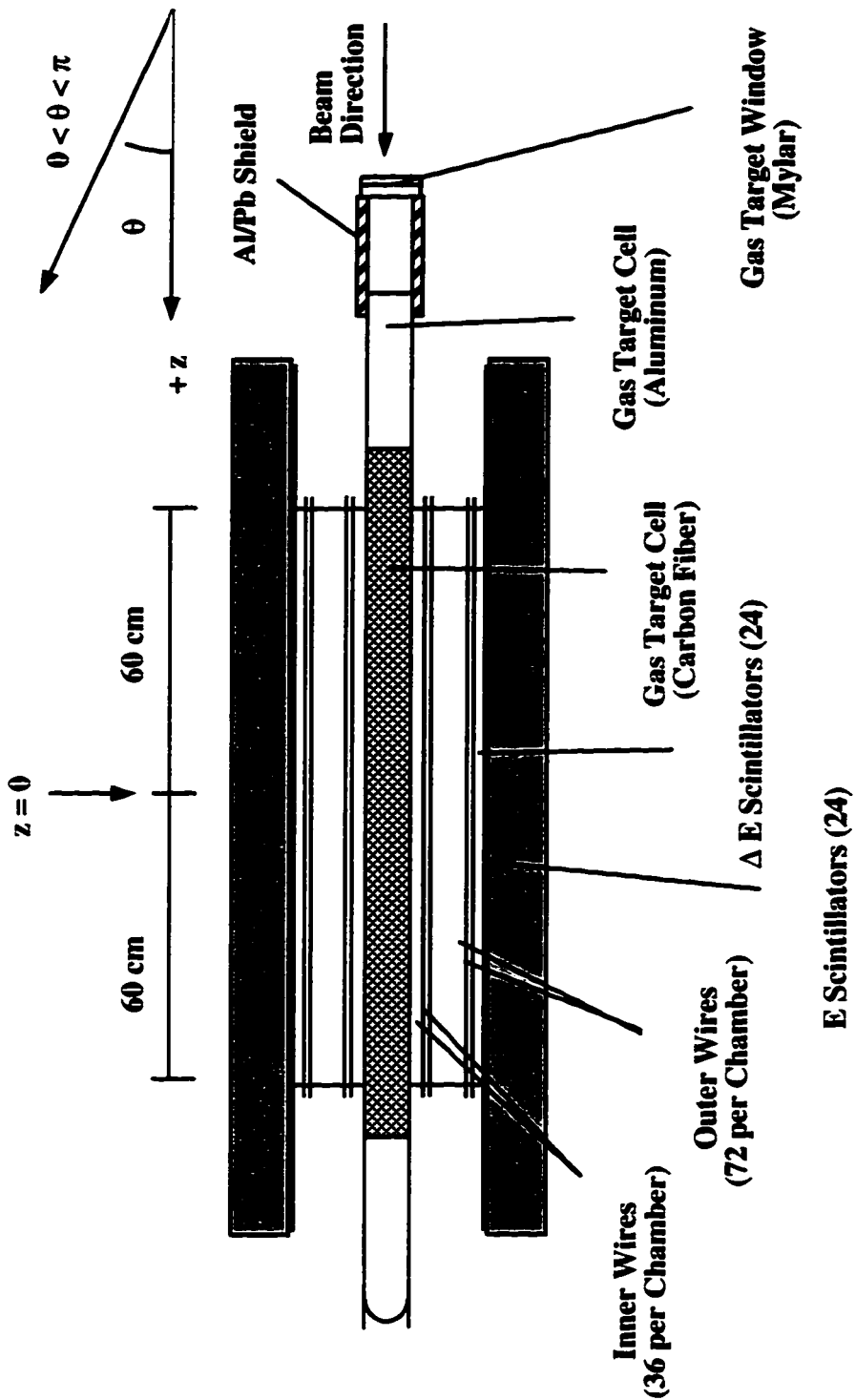


Figure 2.6: Side view of the SALAD Detector.

of passing particles allowing them to be detected in the calorimeter while avoiding dead zones which would result from the use of supporting rods. This foam is lined on both sides with a thin sheet of kapton, coated with a conducting film of graphite. The wires in each wire chamber are separated by a thin ribbon of graphite coated Kapton. The ribbons and walls are connected to a negative high voltage source.

2.3.1.1 ADC Pedestals

Signals from each end of the wires in the four chambers, as well as each end of the ΔE and E scintillators are sent to a fastbus ADC. This results in a total of 528 ADC channels for which a pedestal calibration is required. At the beginning of each SALAD experiment a pedestal run is performed by reading the ADC values with no input signal for a large number of random trigger events (typically hundreds of thousands of events). These are called off-line pedestals. These ADC pedestals are then downloaded to the data acquisition computer and used in the data compression and the on-line analysis.

Since pedestals typically drift over time, the ADC pedestals are measured continuously during the experiment. In this experiment an ADC pedestal readout was performed after each 10,000 events. These are called on-line pedestals. On-line pedestals were grouped together in six groups, each spanning a period of about 24 hours, and the appropriate group was used in the data analysis. Variations of the pedestals within each one of these groups are less than 0.5%. Variations of the pedestals between any two groups is less than 4%.

Wire Chamber #	High Voltage (kV)	Leakage Current (μA)
1	-3.7	~ 90
2	-3.8	~ 75
3	-3.9	~ 40
4	-3.8	~ 50

Table 2.1: Applied high voltages and measured leakage currents on the four SALAD wire chambers during the $D(\gamma, pp\pi^-)$ experiment.

2.3.1.2 High Voltage Calibrations

The high voltages that were applied to the wire chambers in this experiment are listed in Table 2.1. The optimum voltage was chosen separately for each chamber by considering the total charge deposited in that chamber by outgoing protons. The charge collected at both ends of all wires in a chamber, Q_{sum} , is shown in Figure 2.7 for each chamber using protons from $D(\gamma, pp\pi^-)$ events.

2.3.1.3 Position Calibrations

The charge deposited is collected at the upstream and downstream ends of the wire. The z position of the hit is, to first order, linearly proportional to ΔQ , given by

$$\Delta Q = \frac{A_u - A_d}{A_u + A_d}, \quad (2.4)$$

where A_u and A_d are the ADC values of the upstream and downstream ends of the wire, respectively. Gain mismatch between the upstream and downstream end electronics require second order corrections. The dependence of z on ΔQ in this case is given by

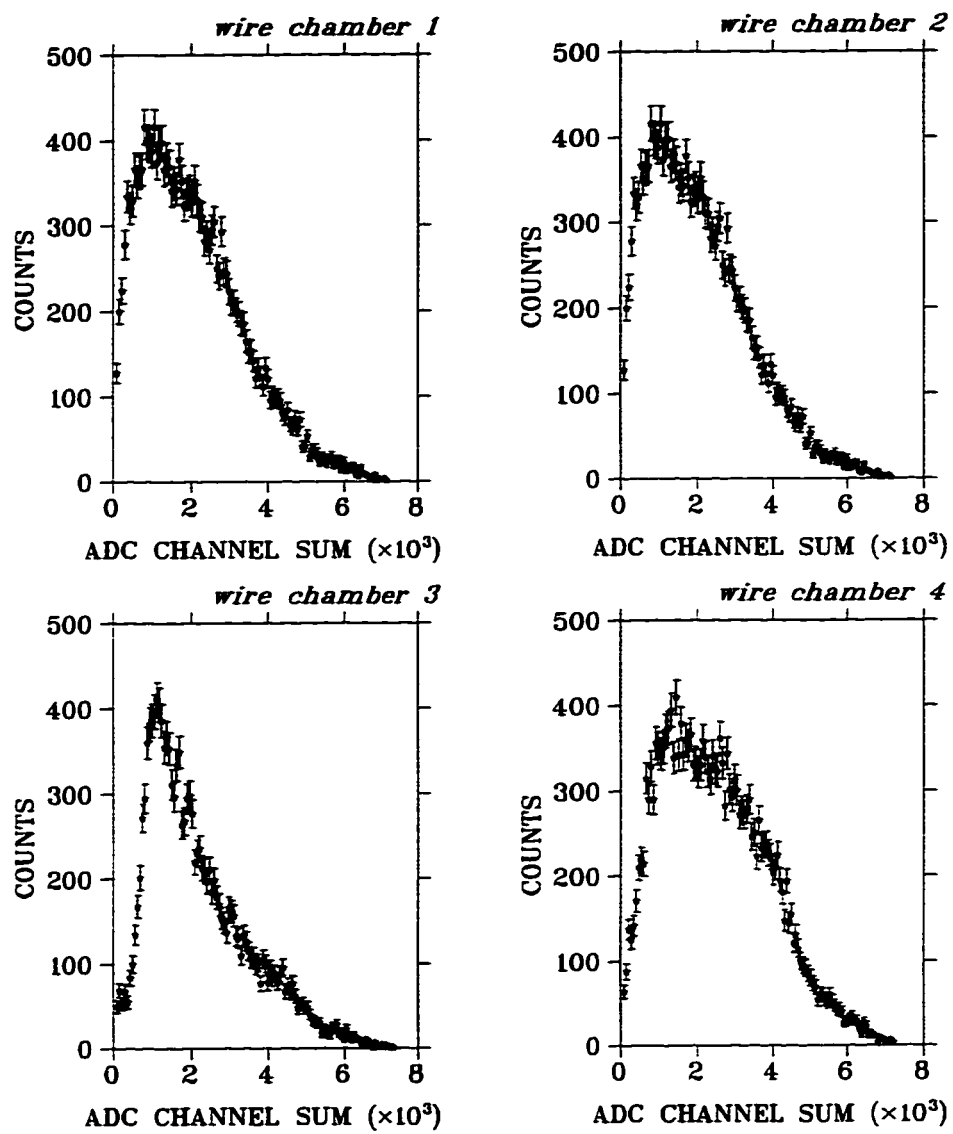


Figure 2.7: Sum of the charge deposited in the wire chambers for three track $D(\gamma, pp\pi^-)$ events.

the equation

$$z = L_0 + L_1 \times \Delta Q + L_2 \times \Delta Q^2 \quad (2.5)$$

where L_1 is the effective wire length, and L_0 and L_2 account for differences in input impedance and gain mismatch between the upstream and downstream electronics. These coefficients are determined from wire chamber calibration measurements.

The wires are calibrated using two ^{55}Fe sources located between the inner and outer wire chambers as shown in Figure 2.8. One of these sources illuminates the inner chambers while the other illuminates the outer. The sources are well collimated and their positions are computer controlled. When not in use, the sources are parked in shielded areas. For a source calibration, the sources are positioned successively at several z locations. For each z position, the sources are rotated around the axis of the detector in steps of 5° . While these sources may not be precisely aligned with respect to one another, the relative positions of the two sources may be determined by tracking cosmic ray particles through the detector. In this way it was determined that in this experiment the two sources were misaligned by -13 mm, and this correction was made to the calibration.

In this experiment two source calibration measurements were performed. Measurements at seven z positions were made ($z = 0, \pm 150, \pm 300, \pm 450$ mm). A quadratic fit of z versus ΔQ was used to determine the constants of equation 2.5. One of these calibration measurements was used in the analysis of the data, whereas the other was used to determine the error in the measurement. The resulting difference in the number of good events between the two measurements is less than 2%. The same calibration file was used to generate and analyze Monte Carlo events to ensure perfect consistency with the data. Several wires resulted in a bad spectrum. These wires were turned off

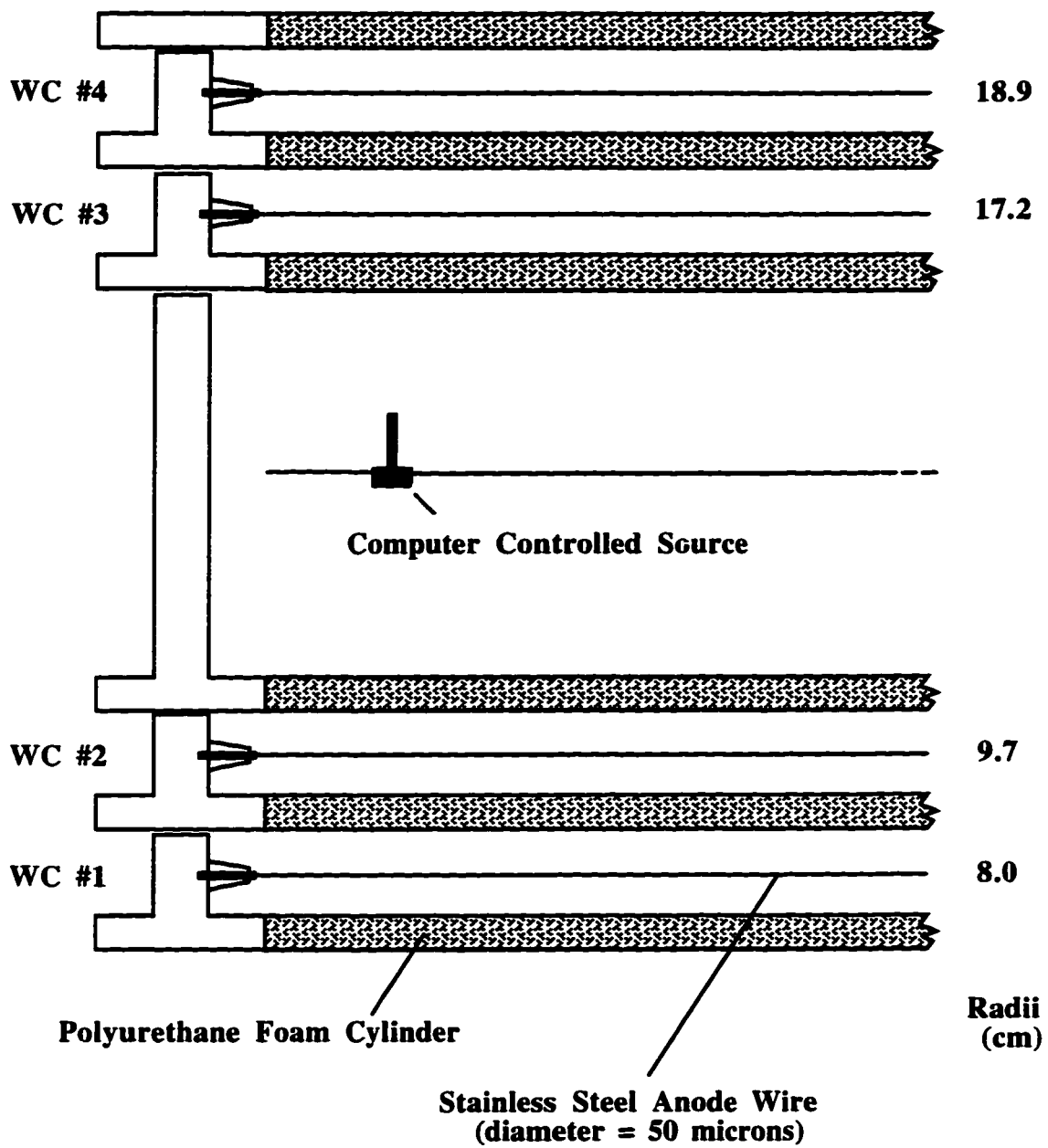


Figure 2.8: Support structure for the wire chambers.

Wire Chamber	Wires
1	13
2	15, 19, 23
3	5, 27, 39, 40, 61
4	9, 23, 24, 40, 41, 42, 59, 71

Table 2.2: Wires excluded from the $D(\gamma, pp\pi^-)$ analysis.

in both the data analysis as well as in the Monte Carlo. Table 2.2 contains a list of the bad wires.

For a source run, the trigger is provided by the wire chamber signals. Schmitt triggers are used at both ends of each wire. The wires from the four wire chambers are organized in 12 sectors. Each sector contains three wires from each inner chamber, and 6 wires from each outer chamber. The Schmitt triggers in a given sector are enabled only when the wires in that sector are illuminated by the source. The readout is triggered by a single hit at either end of a wire in the active sector.

2.3.1.4 Angular Resolutions

The wire chambers provide a determination of the coordinates of outgoing charged particles. The finite spacing between the wires limits the ϕ resolution to about $\sigma_\phi = 2.6^\circ$. Two factors limit the z position resolution in a source calibration measurement. The first factor results from the input impedance of the amplifying circuit. This results in a resolution that is z dependent; being minimum in the middle and maximum near the ends. The other factor is due to the finite collimation of the source to about 0.5 mm. The overall resolution varies from 1.2 mm at the center to 2.5 mm standard deviation

near the ends. Figure 2.9 shows a z position spectrum when the source is located at $z=0$.

Once a charged particle is tracked through the wire chambers, its angle θ may be calculated. The resulting resolution in θ is θ -dependent. Figure 2.10 shows the variation in σ_θ as a function of θ . The z dependence of σ_θ resulting from the different z position resolution along the wire is neglected.

2.3.2 Calorimeter

The ΔE scintillators are 180.3 cm long whereas the E scintillators are 182.9 cm long. Each of the 24 $\Delta E - E$ scintillators subtends an angle of 15° in ϕ . The ΔE scintillators are 0.32 cm thick, while the E scintillators are 12.75 cm thick. Photomultiplier tubes are attached to both ends of each ΔE and E scintillator via light guides. Since the scintillator bars are 1.83 m long, Bicron BC-408 and BC-412 were chosen for their long attenuation lengths. Each of the ΔE and E scintillators is separately wrapped in a thin sheet of aluminized mylar. The calorimeter is sealed as a unit by a steel cylinder from the outside and a black vinyl tube from the inside.

2.3.2.1 Scintillator Thresholds

The SALAD scintillator thresholds are a function of both the particle energies and the track angles. As shown in Figure 2.11, the minimum threshold occurs at 90° , at which angle a pion needs a kinetic energy of about 10 MeV to deposit enough energy in the scintillators and result in a signal that exceeds threshold; whereas the threshold proton energy is about 20 MeV. On the other hand, the scintillators are capable of stopping pions and protons with a maximum energy of 60 MeV and 140 MeV, respectively.

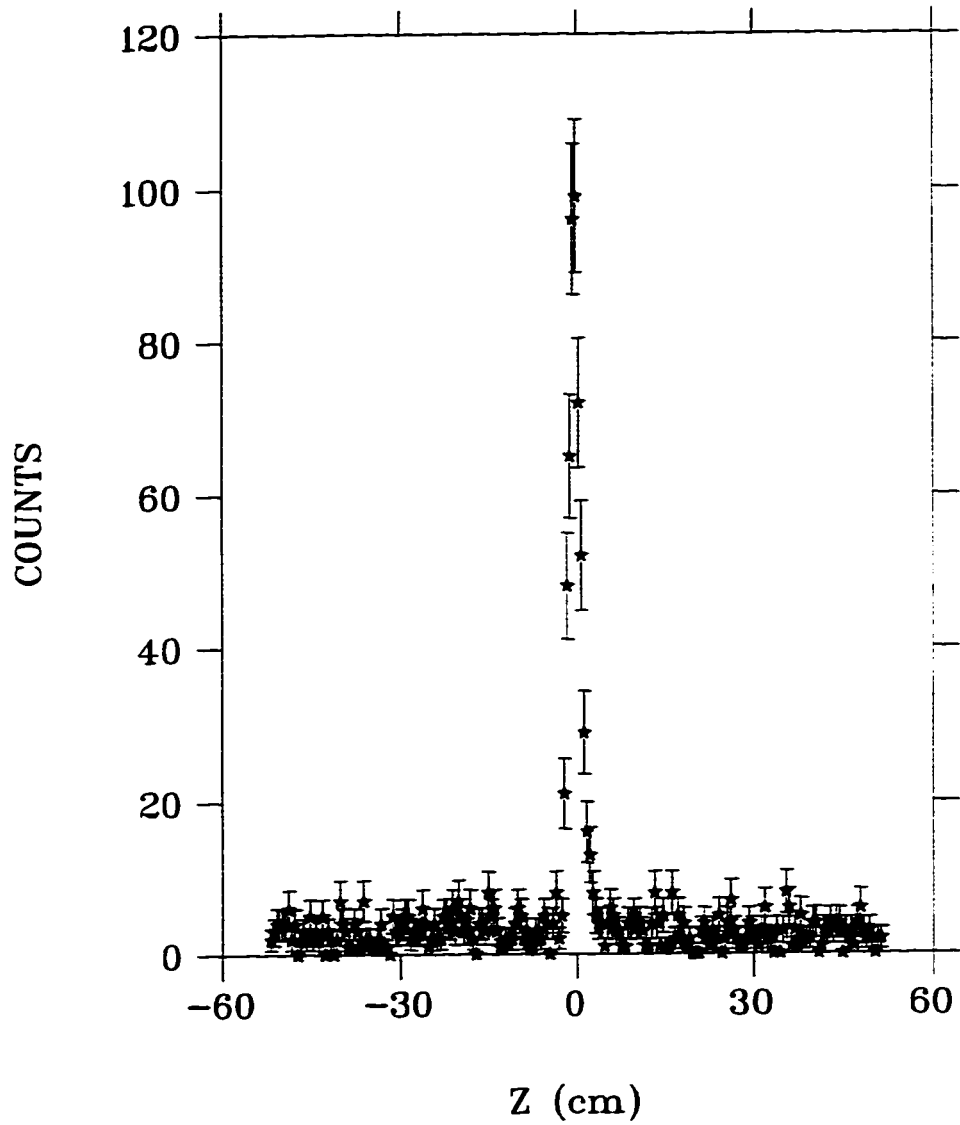


Figure 2.9: Position histogram for the radioactive source located at the center of a wire.

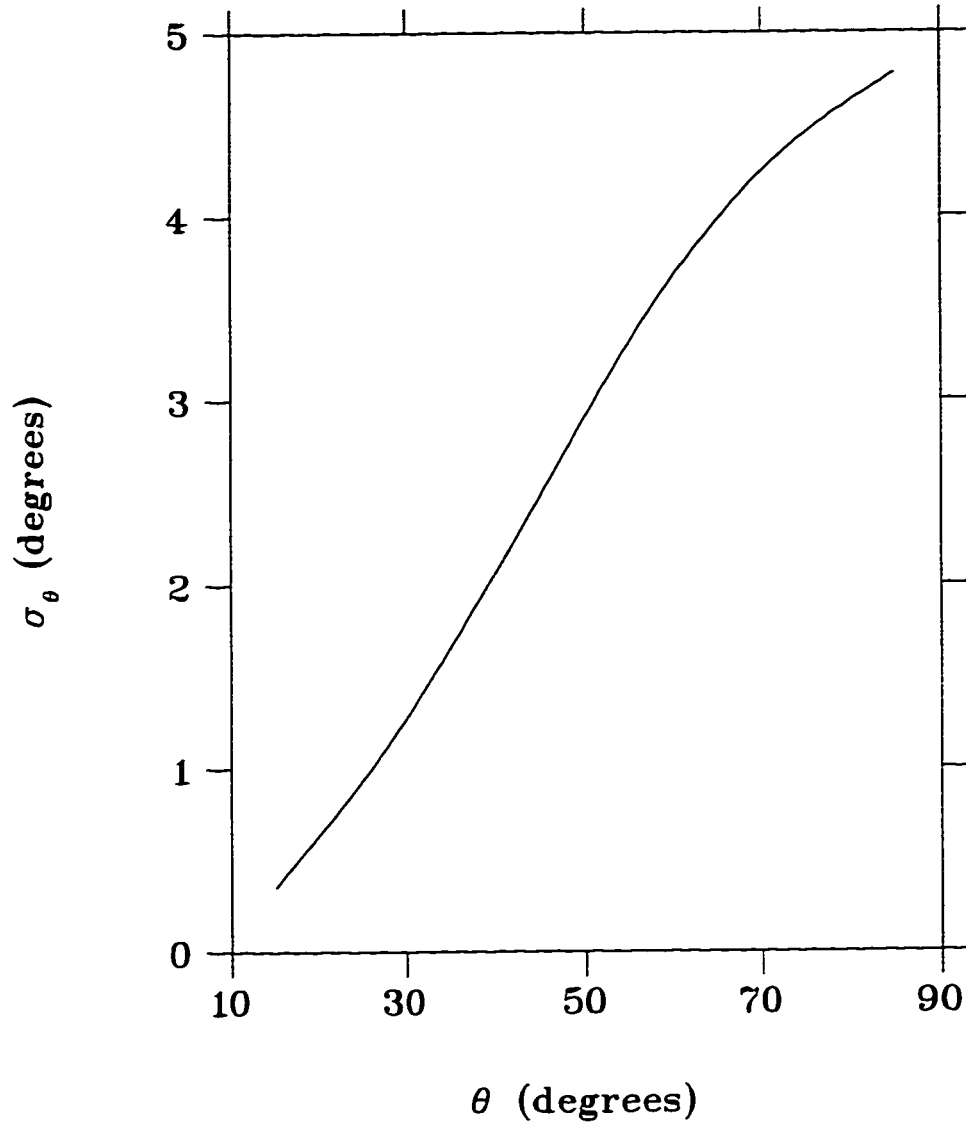


Figure 2.10: SALAD resolution of the scattering angle θ .

incident at an angle of 90° . Since the maximum kinetic energy available for the three final state particles is ~ 155 MeV (maximum electron energy minus pion mass), the amount of energy/particle available is low enough that particles with enough energy to punch through the scintillators are unlikely.

2.3.2.2 PMT High Voltage Calibrations and Gain Measurements

Gain calibrations of the ΔE and E PMT's were first determined from p-p elastic scattering at TRIUMF [30]. In two body elastic scattering, a knowledge of the direction of one of the outgoing particles allows a complete determination of the final state kinematics. When a proton is detected, its direction may be determined by tracking it through the wire chambers. Its energy may therefore be calculated, corrected for energy losses in the walls of the target and wire chambers, and compared to the measured ADC value.

The ADC values recorded at the upstream and downstream ends of a scintillator are given by

$$ADC_u = \alpha N_0 e^{-\lambda z}, \quad (2.6)$$

and

$$ADC_d = \beta N_0 e^{-\lambda(L-z)}, \quad (2.7)$$

where α and β are factors that depend on the light collection efficiency and the external electronics including the PMT gain, N_0 is the total number of photons emitted in the scintillator, λ is the scintillator attenuation length, and z is the distance from the upstream end of the scintillator to where the hit occurred. We may then define a mean ADC value as

$$\overline{ADC} = \sqrt{ADC_u \times ADC_d} = (\sqrt{\alpha\beta} e^{-\lambda L/2}) N_0. \quad (2.8)$$

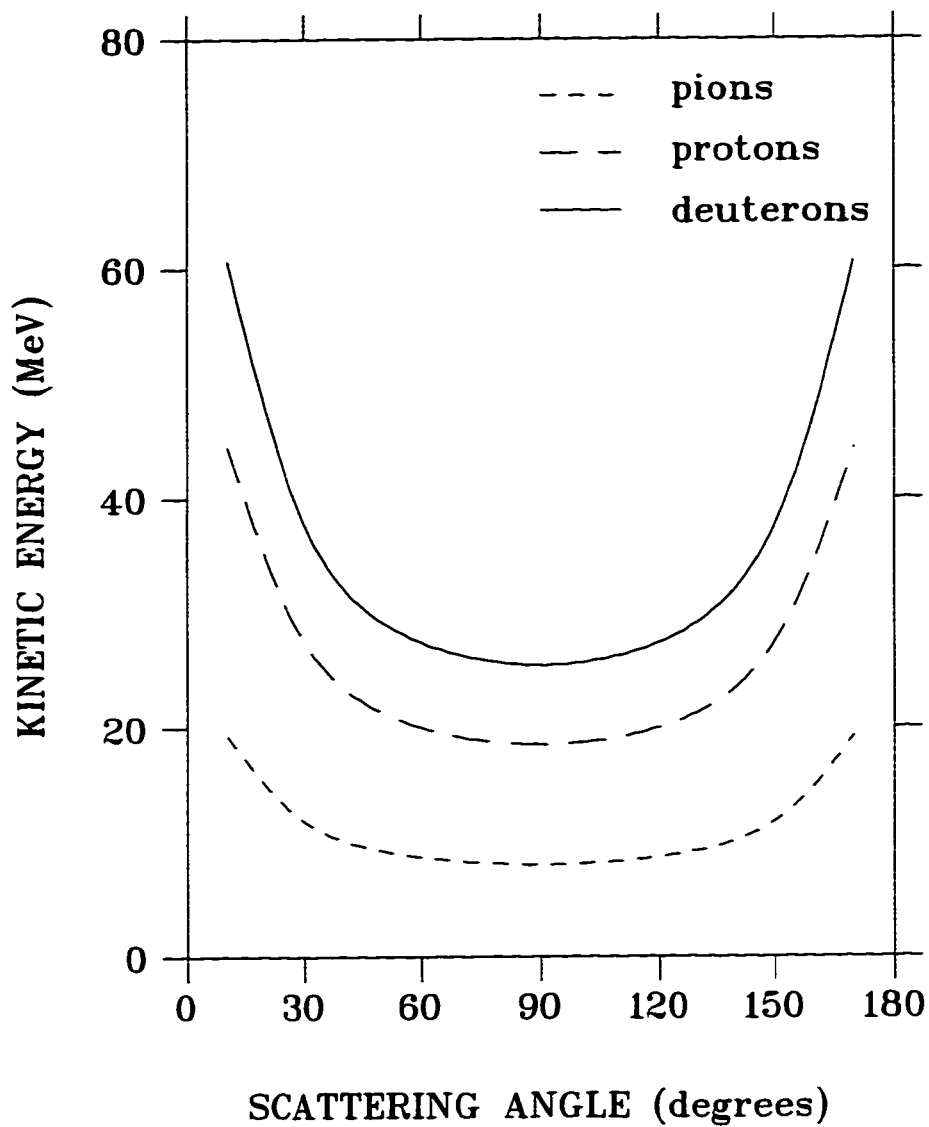


Figure 2.11: Limits on pion and proton energies detectable in the SALAD scintillators as a function of the scattering angle θ .

The energy deposited in a scintillator is, to first order, proportional to N_0 . We then have

$$E_{deposited} = kN_0 = \left(\frac{k}{\sqrt{\alpha\beta}}e^{\lambda L/2}\right)\overline{ADC}, \quad (2.9)$$

where k is a constant. Defining,

$$\overline{gain} = \frac{\sqrt{\alpha\beta}e^{-\lambda L/2}}{k}, \quad (2.10)$$

we have,

$$\overline{gain} = \frac{\overline{ADC}}{E_{deposited}}. \quad (2.11)$$

Gains may thus be determined using equation 2.11. A knowledge of neither α and β nor the attenuation length is required to determine the gains. It is worth noting that the term "gain" in this case does not refer to the PMT gains alone, but includes the attenuation length and the light collection efficiency as well.

Since gains drift with time, a re-calibration was required at the time of our experiment. Cosmic rays provide a convenient source of radiation that may be used for this purpose. The energy loss of cosmic rays in the ΔE and E scintillators was measured at TRIUMF after the gains were determined from p-p elastic scattering. This measurement may be repeated at any future time allowing a redetermination of the gains.

The scintillator gains are determined at the beginning of each experiment using cosmic ray data. The PMT high voltages are adjusted so as to approximately match the gains among the 24 ΔE and 24 E scintillators. Several cosmic ray data sets are acquired during each experiment to determine the PMT gain drift. Gains were also determined from $D(\gamma, pn)$ and ${}^3He(\gamma, pD)$ experiments, which provide a large number of events with overdetermined kinematics. This allows a consistency check on the gains determined from cosmic ray data.

Six cosmic ray data runs were performed during the June 1992 SALAD run which includes the $D(\gamma, pp\pi^-)$ and the $^{12}\text{C}(\gamma, pp)$ experiments. The two experiments were performed over a four-week period. The gains determined from these six runs were observed to decrease steadily over the four-week period, for both the ΔE and E scintillators, as may be seen from Figure 2.12. The gain of each ΔE and E scintillator was fitted to a function of the form

$$\text{gain} = g_0 + g_1 t, \quad (2.12)$$

where g_0 and g_1 are constants determined from the fit.

During the data analysis, the proper gains are calculated at the beginning of each run from the formula above. Each $D(\gamma, pp\pi^-)$ run spans a period of about 90 minutes, during which time the variations of the gains are negligible. Monte Carlo events were generated and analyzed with the value of the gains computed from equation 2.12 at the middle of the $D(\gamma, pp\pi^-)$ run.

2.3.2.3 Light Output Corrections

Plastic scintillator light response is linear for electrons of energies above 125 keV. For heavier particles the response is non-linear up to much higher energies. Electrons stopped in plastic scintillators result in higher light output than heavier particles of the same incident energy [9]. This phenomenon is a result of the saturation of available atomic states that occurs due to the high ionization density along the particle's track in the case of protons and other heavy charged particles. In this case, part of the energy deposited is dissipated non-radiatively. Although this process is not described exactly, several semi-empirical formulas have been advanced. The parameterization of Wright was used in the present analysis [43].

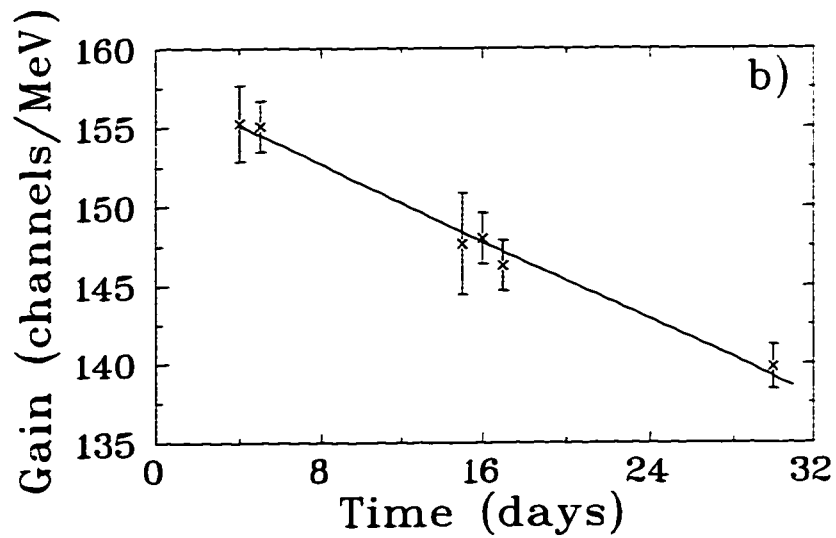
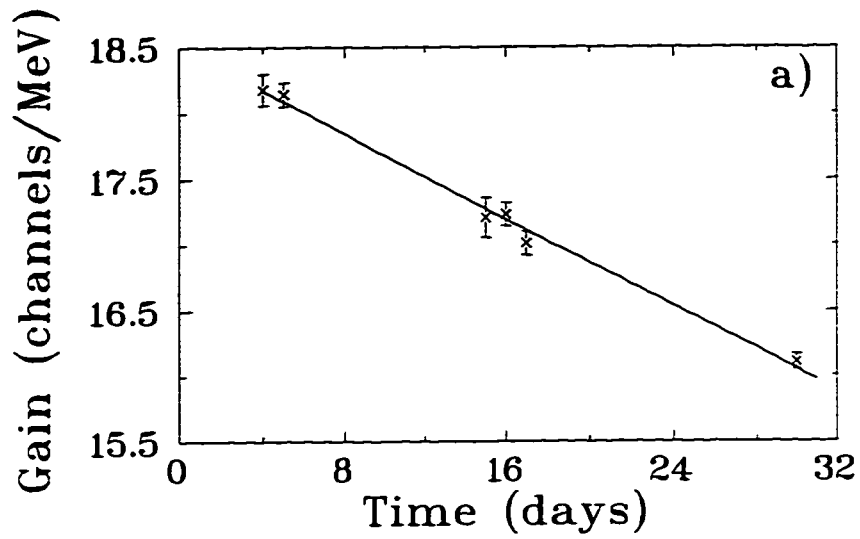


Figure 2.12: Scintillator gain versus time for a) a typical E scintillator and b) a typical ΔE scintillator. The data points are determined from cosmic ray data; the solid line is a linear fit.

2.3.2.4 Energy Resolution

The energy resolution of the scintillators was determined from overdetermined kinematics obtained from the ${}^3\text{He}(\gamma, pD)$ and $D(\gamma, p)n$ experiments. Figure 2.13 shows a plot of σ_E as a function of energy deposited in the ΔE and E scintillators. The data are fit to a function of the form $\sigma_E = A + B\sqrt{E}$, where both A and B are determined from the fit. These resolutions are used in the Monte Carlo to simulate the scintillators' response.

2.4 Trigger and Data Acquisition

A total of 82 hours of beam on target were achieved in this experiment. The acquired data were written to magnetic (8 mm video) tapes. About 10% of these data were analyzed on line and many histograms were monitored during each run. A total of 87 $D(\gamma, pp\pi^-)$ runs were performed. A typical $D(\gamma, pp\pi^-)$ run results in 300 megabytes of data and consists of ~ 1 million coincidence triggers.

2.4.1 Trigger Electronics

The SALAD trigger electronics are shown in Figure 2.14. Two different calorimeter trigger circuits are available. In the first circuit, the four output signals from both the upstream and the downstream ends of a $\Delta E - E$ scintillator pair are sent to a four-fold coincidence unit. Different combinations of these four signals may be computer selected, and the desired thresholds may be demanded.

In the second circuit, the four $\Delta E - E$ signals are sent to a fan in / fan out module

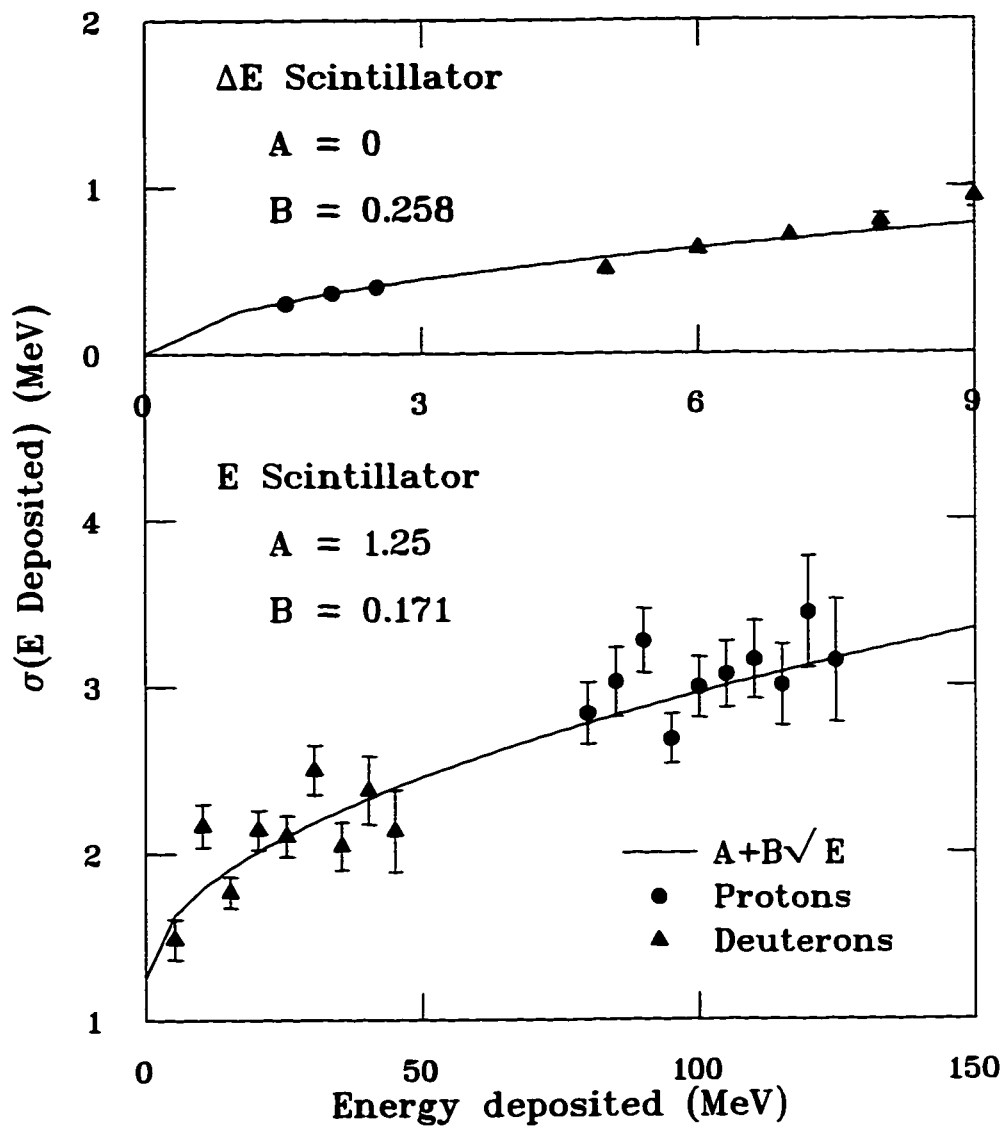


Figure 2.13: Energy resolution of the SALAD scintillators. The top plot is for the ΔE scintillators, and the bottom plot is for the E scintillators. The solid line is a fit to the data.

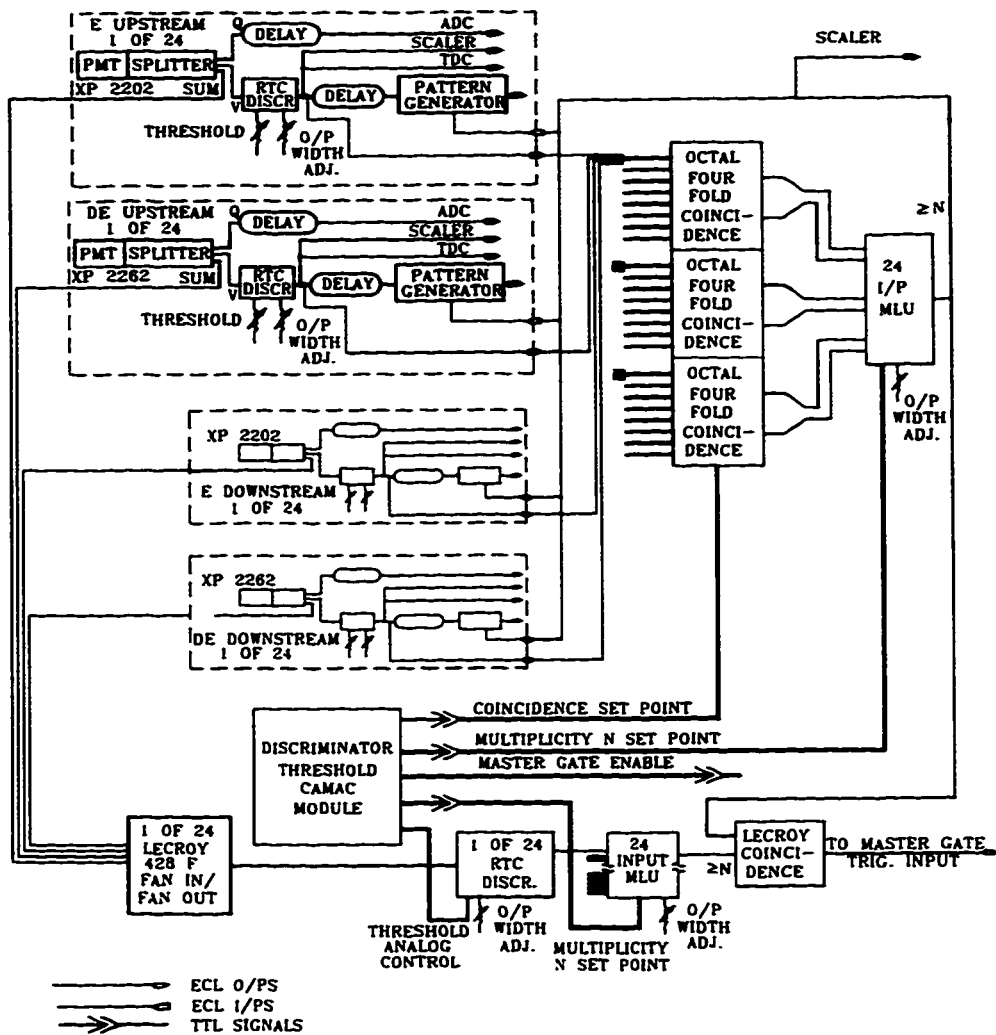


Figure 2.14: SALAD scintillator's circuitry and trigger logic.

and summed in the form

$$\Delta E_s + f E_s, \quad (2.13)$$

where ΔE_s (E_s) is the sum of the upstream and downstream $\Delta E(E)$ signals, and f is a constant determined by the signal attenuation and tube gains of the ΔE counters relative to the E counters. This sum may be required to exceed a certain computer selectable threshold referred to as a sum-threshold. The sum-threshold approximates a stopping power discriminator.

The two calorimeter trigger circuits may be used alone or in coincidence. The output from the 24 coincidence units are sent to a 24-input multiplicity logic unit (MLU). This allows triggering on multi-particle final states. The multiplicity is computer selectable and may be set to require anywhere from 1 to 4 $\Delta E-E$ scintillator pairs. In a production run, the calorimeter trigger may be required to occur in coincidence with the tagger.

For cosmic runs, since cosmic are minimum ionizing, the first of the above described triggers is used. The selected combination is for $2(E_{upstream} \cdot E_{downstream})$ to be above a reasonably low threshold. For production runs, the sum-threshold is used in coincidence with a $(\Delta E_{upstream} \cdot \Delta E_{downstream})$ trigger. Since the major background at SAL is due to electrons and positrons resulting from $\gamma \rightarrow e^+e^-$ pair production, the sum-threshold allows an on-line rejection of a good fraction of this background.

For reactions with three particles in the final state, at least five quantities should be measured for a complete determination of final state kinematics if the beam energy is known. In the analysis of the $D(\gamma, pp\pi^-)$ reaction a fitting program was used where only overdetermined events were analyzed to allow a high confidence level, and an accurate determination of the kinematics. A minimum of multiplicity two trigger was therefore used. The experimental trigger is usually required to occur in coincidence with the

tagger, but since the maximum tagged photon energy was 229 MeV, for tagged events, the vertex energy of at least one of the outgoing particles is in most cases too low for that particle to reach the calorimeter and cause a trigger. Many three track events may therefore be lost. To avoid this, the trigger multiplicity was set such that multiplicity two SALAD triggers were required to occur in coincidence with a tagger signal, while multiplicity three SALAD triggers were accepted without requiring a tagger signal. This is called a multiplicity 2 + 3 forced trigger. Events with a multiplicity 2 trigger were analyzed and found to be mostly background. Only events with a multiplicity 3 trigger are presented here.

2.4.2 Data Acquisition

A Motorola VME system was used for data acquisition. The system was first used in this experiment, and resulted in drastically increasing the speed of data acquisition over previous SALAD operation. The limiting factor in the speed of the data acquisition is now the leakage current on wire chamber 1, which imposes a limit on the photon flux. Typical values of the leakage currents on the wire chambers for the $D(\gamma, pp\pi^-)$ experiment are listed in Table 2.1. The leakage current on wire chamber 1 is highest since this chamber is closest to the beam line, and a large fraction of the background in SALAD occurs at small angles (section 4.1.1).

The rate at which particles are detected in one of the tagger middle channels is called the e-29 rate. The leakage currents cited in Table 2.1 were obtained at an average e-29 rate of about 65 kHz. While the wire chambers are expected to withstand higher leakage currents, the e-29 rate was kept at a reasonably low value, such that the leakage current on wire chamber 1 does not exceed 100 mA. This was mainly done to keep

the hit multiplicity reasonably low so that particles may be easily tracked in the wire chambers.

Chapter 3

Theory

3.1 Introduction

Although several calculations are available for the photo- and electro- disintegration of the deuteron [31, 29], only one calculation has been done for $\gamma D \rightarrow pp\pi^-$. This calculation is carried out by Jean-Marc Laget, and has been very successful in describing previous experimental data. In this chapter the details of this calculation will be presented, as well as comparisons to this data. Comparisons of Laget's calculation to the SALAD data will be presented in the fifth chapter.

3.2 Laget's Model

For a three body reaction of the form

$$a + b \rightarrow c + d + e \tag{3.1}$$

the total momentum and energy in the initial state are given by

$$\vec{P}_i = \vec{p}_a + \vec{p}_b \quad (3.2)$$

and

$$E_i = E_a + E_b. \quad (3.3)$$

Similarly the total momentum and energy in the final state are given by

$$\vec{P}_f = \vec{p}_c + \vec{p}_d + \vec{p}_e \quad (3.4)$$

and

$$E_f = E_c + E_d + E_e. \quad (3.5)$$

The relative velocity of particles a and b is

$$|v_a - v_b|. \quad (3.6)$$

The nine fold differential cross section for this process is then given by

$$d^9\sigma = \frac{1}{N_i} \sum_i \sum_f \frac{(2\pi)^4}{|v_a - v_b|} \delta(E_i - E_f) \delta(\vec{P}_i - \vec{P}_f) |T_{fi}|^2 \frac{d^3p_c}{(2\pi)^3} \frac{d^3p_d}{(2\pi)^3} \frac{d^3p_e}{(2\pi)^3}, \quad (3.7)$$

where the initial states are averaged and the final states are summed over. and N_i is the number of initial spin states. The factor T_{fi} that appears in this equation is the transition matrix element given by

$$T_{fi} = \langle \psi_f | T | \psi_i \rangle, \quad (3.8)$$

where

$$T = V + V \frac{1}{E - H_o} T, \quad (3.9)$$

and V is the interaction.

It is conventional in low energy nuclear physics to calculate the scattering cross section by solving the Schrödinger equation assuming a certain model for the interaction. The wave function is usually expanded in terms of partial waves, and the Schrödinger equation is solved for each partial wave. At higher energies more partial waves contribute, and the calculation becomes more difficult.

An alternative method that may be used in this case is to expand the cross section in terms of Feynman diagrams. This method has been particularly successful when dealing with electromagnetic interactions. The weak nature of the interaction results in a coupling constant α , where α is the fine structure constant ($=1/137$). Since $\alpha \ll 1$, a perturbative expansion may be used, allowing the calculation of the cross section to the accuracy desired. In contrast, the strong interaction has a coupling constant of the order of unity, and it is no longer obvious that a perturbative expansion will work. If such a method is to be used when dealing with the strong interaction, a calculation of the matrix elements corresponding to these Feynman diagrams has to be performed, and it has to be shown explicitly that the higher order Feynman diagrams will indeed result in small contributions. If this is the case, once the cross section is calculated, a comparison to the data may be made, allowing a confirmation that the selected set of Feynman diagrams is sufficient in describing the cross section.

This model has two additional advantages, the first of which is that the model is completely relativistic. In the energy range of interest, however, a full relativistic treatment is not required. Since a semi-relativistic treatment greatly simplifies the calculations, only terms up to the order of p^2/m^2 are retained in the calculation of the transition amplitudes. The model also allows the calculation of the matrix element for each of the Feynman diagrams separately. This allows each Feynman diagram to be

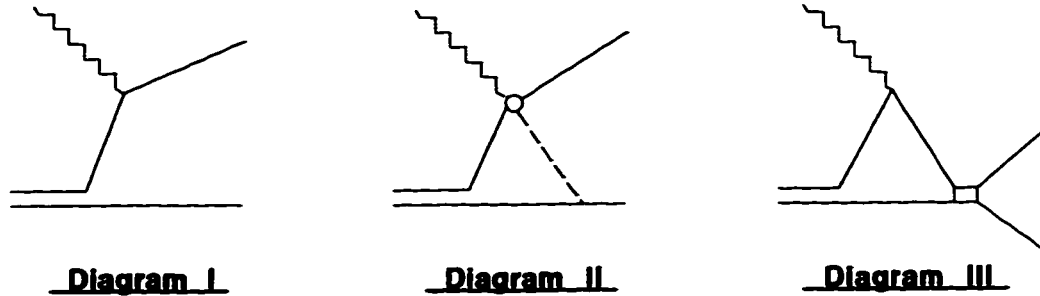


Figure 3.1: Feynman diagrams for the two body disintegration of the deuteron.

singled out and its effects investigated, thus providing an excellent way of investigating the effects of the different final state interactions.

For example, the two body photodisintegration of the deuteron may be expanded in terms of the Feynman diagrams of Figure 3.1. Figure 3.2 shows the cross section for this process. The data is a compilation from several experiments. Laget's calculation is shown including only the quasi-free process (diagram I of Figure 3.1) as the dashed curve, and including contributions from two nucleon mechanisms as the solid curve. The two nucleon mechanisms include the production of a pion at one nucleon which is absorbed by the other (diagram II of Figure 3.1), as well as the nucleon-nucleon rescattering diagram (diagram III of Figure 3.1). The contribution of the quasi-free process dominates the cross section at low energies. At higher energies contributions from the two nucleon mechanisms become important, increasing from about 10% at $E_\gamma = 10$ MeV to about 30% at $E_\gamma = 100$ MeV [26, 29].

Laget's method consists of expanding the transition amplitudes corresponding to the different Feynman diagrams in terms of the resonant singularities. This allows each diagram to be singled out and its effects to be examined by choosing the kinematics

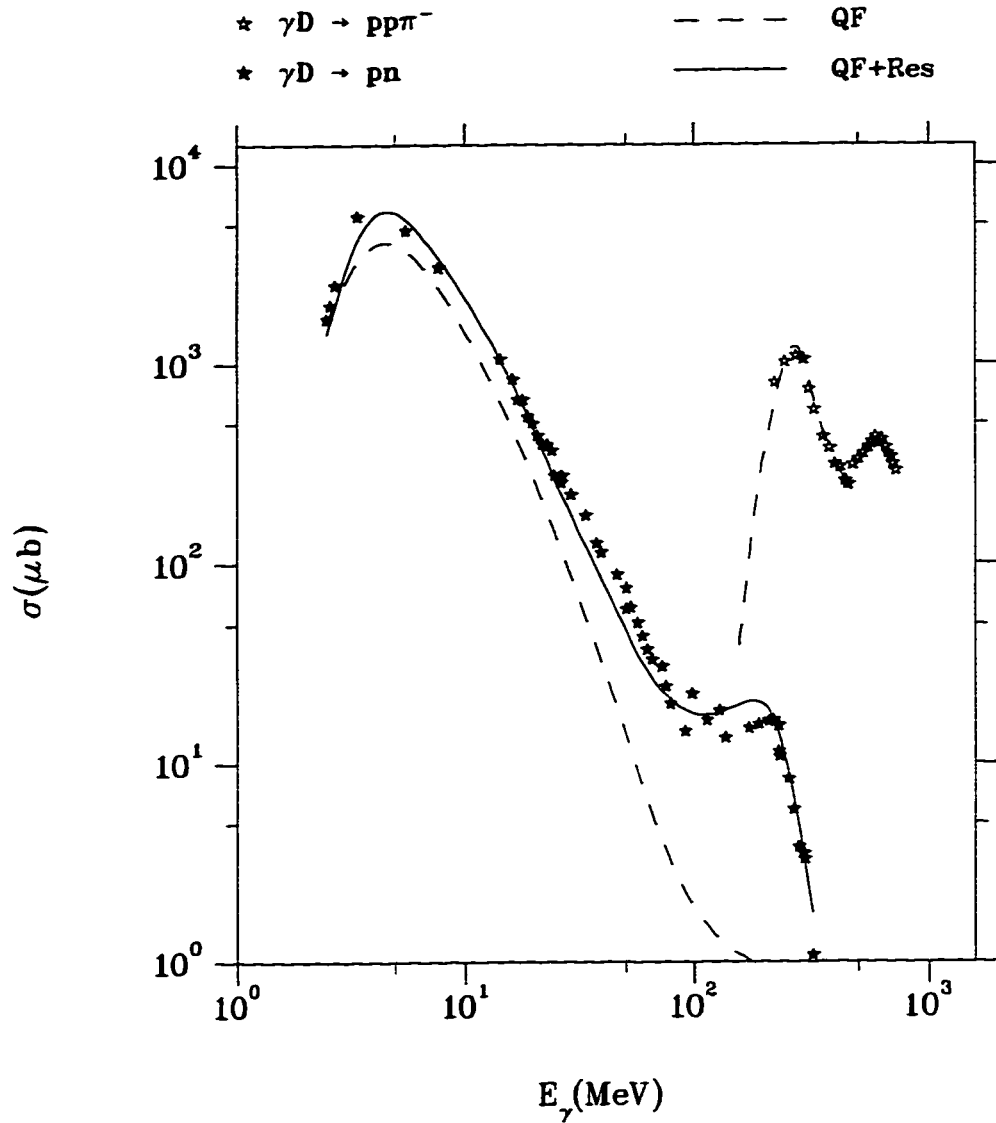


Figure 3.2: Total photoabsorption cross section on deuterium. The experimental points are a compilation from several experiments as plotted in reference [29]. The theoretical curves are calculated by J.M. Laget [29]. The dashed curves include only the quasi-free diagram, whereas the solid curve includes rescattering effects as well.

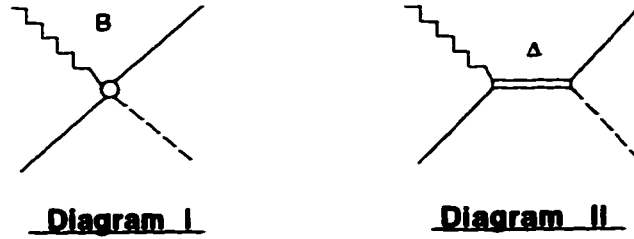


Figure 3.3: Feynman diagrams for the reaction $\gamma p \rightarrow n\pi^+$.

in the physical region to be close to the singularities. For example, the amplitude of the elementary reaction $\gamma p \rightarrow n\pi^+$ may be expanded in terms of the Born terms and the $\Delta(1232)$ resonance, as shown in Figure 3.3. The Born terms result in a strong background with little variation with energy, as may be seen from Figure 3.4. The amplitude responsible for the creation of the $\Delta(1232)$ has a pole near the mass of the Δ and results in the strong variation of the cross section in the corresponding energy range [27].

3.3 Calculation of the $\gamma D \rightarrow pp\pi^-$ Reaction Cross Section

The diagrammatic expansion for the $\gamma D \rightarrow pp\pi^-$ reaction is shown in Figure 3.5. The kinematic equations for this reaction in the laboratory frame may be written as

$$\vec{k} = \vec{\mu} + \vec{p}_1 + \vec{p}_2 \quad (3.10)$$

and

$$k^0 + M_D = \mu^0 + p_1^0 + p_2^0, \quad (3.11)$$

where (k°, \vec{k}) , $(\mu^\circ, \vec{\mu})$, (p_1°, \vec{p}_1) and (p_2°, \vec{p}_2) are the four-momenta of the photon, pion, and the two nucleons, respectively. When the photon beam energy is known, five independent variables must be measured for a complete determination of the final state kinematics. If the measured quantities are the pion momentum and one proton direction $(\mu, \theta_\pi, \phi_\pi, \theta_1, \phi_1)$, a measurement of the differential cross section, $d\sigma/d\mu d\Omega_1$, is possible. A calculation of the cross section gives [25]

$$\frac{d\sigma}{d\vec{\mu}d\Omega_1} = \frac{Q}{|\vec{\mu}_{cm}|} \frac{p_2^\circ |\vec{p}_1|^3}{\mu^\circ |\vec{p}_1^\circ p_2^\circ - p_1^\circ \vec{p}_1 \cdot \vec{p}_2|} \frac{d\sigma}{d\vec{p}_2[d\Omega_\pi]_{cm}}, \quad (3.12)$$

where Q is the total energy of the detected nucleon-pion pair in their center of mass (cm) frame. The reduced cross section may be expressed as a sum of the matrix elements corresponding to the six diagrams of Figure 3.5 [25]

$$\frac{d\sigma}{d\vec{p}_2[d\Omega_\pi]_{cm}} = \frac{1}{(2\pi)^5} \frac{|\vec{\mu}_{cm}|m^2}{4|\vec{k}|p_2^\circ Q} \frac{1}{6} \sum_{\epsilon, M, m_1, m_2} \left| \sum_{i=1}^{VI} \mathcal{M}_i(\vec{k}, \epsilon, \vec{\mu}, M, \vec{p}_1, m_1, \vec{p}_2, m_2) - \sum_{i=1}^{VI} \mathcal{M}_i(\vec{k}, \epsilon, \vec{\mu}, M, \vec{p}_2, m_2, \vec{p}_1, m_1) \right|^2. \quad (3.13)$$

where ϵ is the photon polarization, and M , m_1 , and m_2 are the magnetic quantum numbers of the deuteron and the two nucleons, respectively, and m is the nucleon mass. The Pauli exclusion principle is taken into account by subtracting two matrix elements in which the two outgoing protons are interchanged.

In the sections below Laget's calculations of the above matrix elements are presented, and comparisons to previous experimental data are made.

3.3.1 The Single Nucleon Term

The first order Feynman diagram is the quasi-free diagram (diagram I of Figure 3.5), and as in the case of the two body photodisintegration of the deuteron, it accounts for

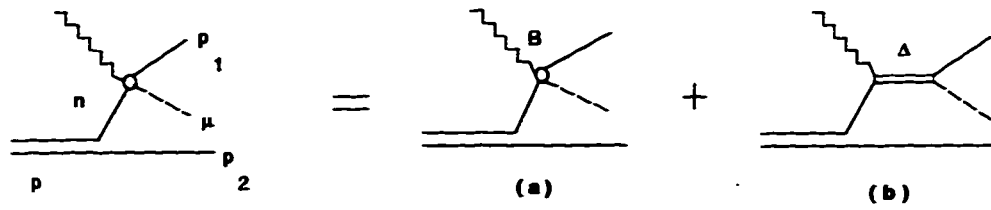


Diagram I

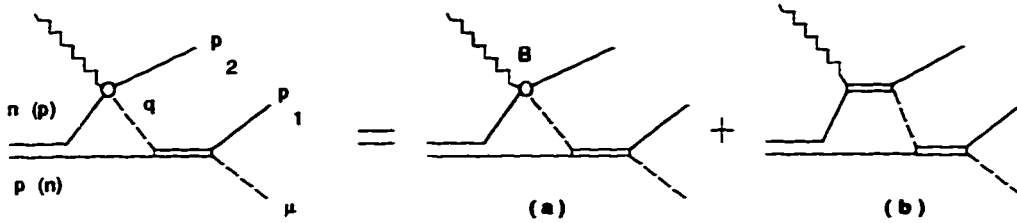


Diagram II

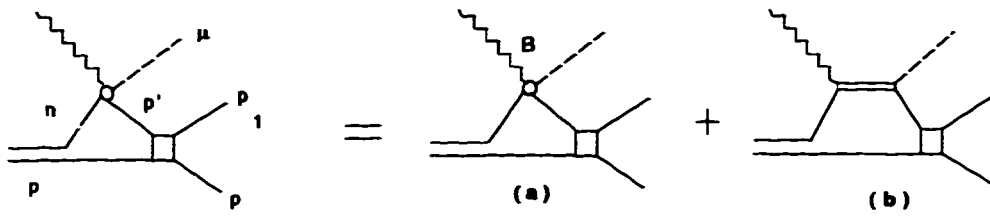


Diagram III

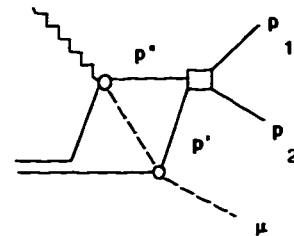
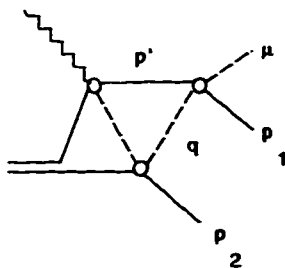
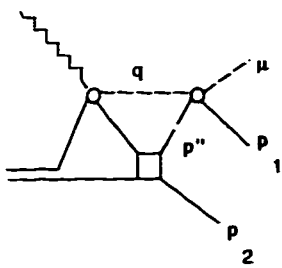


Figure 3.5: Feynman diagrams for $\gamma D \rightarrow pp\pi^-$.

most of the $\gamma D \rightarrow pp\pi^-$ cross section. In this approximation the photon is absorbed by the neutron. The proton does not participate in this reaction and remains there as a spectator, carrying its Fermi energy and momentum.

The matrix element for this diagram may be written as [25]

$$\begin{aligned} \mathcal{M}_I(\vec{k}, \epsilon, \vec{\mu}, M, \vec{p}_1, m_1, \vec{p}_2, m_2) = \\ i \sum_{m_l, m_s} \sum_{l, s} \langle lm_l sm_s | 1M \rangle \langle \frac{1}{2}(m_s - m_2) \frac{1}{2}m_2 | sm_s \rangle \times \\ u_l(p_2) Y_l^{m_l}(\hat{p}_2) T_{\gamma, N}(\vec{p}_1, m_1, -\vec{p}_2, m_s - m_2). \end{aligned} \quad (3.14)$$

The $D \rightarrow np$ vertex in this diagram is defined by the deuteron wave function, $u_l(p_2)Y_l^{m_l}(\hat{p}_2)$, where both an s- and a d-wave component are allowed. The wave function is chosen to be of the Hulthén form with a soft core. It has been shown by Laget that the different deuteron wave functions give similar results as the matrix element is strongly dependent on the low momentum distribution of the wave function, and typical deuteron wave functions give similar results in this range. The $\gamma N \rightarrow N\pi$ vertex may be obtained from the transition matrix element $T(\gamma N \rightarrow N\pi)$, which is computed up to order p^2/m^2 and given by [5]

$$\begin{aligned} T_{fi}(\gamma N \rightarrow N\pi) = C_\pi C_\gamma \frac{G_1(Q)G_3(Q)}{Q^2 - M_\Delta^2 + iM_\Delta\Gamma(Q)} \times \\ \langle \chi_f | \vec{S} \cdot \left[\vec{\mu} - \frac{\mu^o}{M_\Delta} \vec{p}_\Delta \right] \vec{S}^\dagger \cdot \left[\left(\vec{k} - \frac{M_\Delta - m}{m} \vec{p}_\Delta \right) \times \vec{\epsilon} \right] | \chi_i \rangle, \end{aligned} \quad (3.15)$$

where \vec{S} is a transition spin operator which connects the four component $\Delta(1232)$ with the two component nucleon Pauli spinors, and p_Δ is the total momentum of the pion-

nucleon pair. The product of the pionic and the electromagnetic isospin factors are [5]

$$C_\pi C_\gamma = \left\{ \begin{array}{lll} \sqrt{2}/3 & \text{for} & \gamma n \rightarrow p\pi^- \\ -\sqrt{2}/3 & \text{for} & \gamma p \rightarrow n\pi^+ \\ 2/3 & \text{for} & \gamma p \rightarrow p\pi^0 \text{ and } \gamma n \rightarrow n\pi^0 \end{array} \right\}. \quad (3.16)$$

The two form factors that appear in this transition matrix, $G_1(Q)$ and $G_3(Q)$, correspond to the γNN (or $\gamma N\Delta$) and the $N\pi\pi$ (or $N\pi\Delta$) vertices, respectively. The width of the Δ , $\Gamma(Q)$, is allowed to be momentum dependent. Each one of these parameters (the form factors and the Δ width) should be determined together with the mass of the Δ at its peak, M_Δ . To get an accurate determination of the values of these parameters one needs to fit as much experimental data as available. Fortunately, three of these parameters, $G_3(Q)$, $\Gamma(Q)$ and M_Δ appear in the transition matrix element for reactions of the type $\pi N \rightarrow \pi N$. In this case the transition matrix is given by [5]

$$T_{fi}(\pi N \rightarrow \pi N) = C_\pi^2 \frac{2M_\Delta G_3^2(Q)}{Q^2 - M_\Delta^2 + iM_\Delta \Gamma(Q)} \times \langle \chi_f | \vec{S} \cdot \left[\vec{q}_f - \frac{q_f^0}{M_\Delta} \vec{p}_\Delta \right] \vec{S}^\dagger \cdot \left[\vec{q}_i - \frac{q_i^0}{M_\Delta} \vec{p}_\Delta \right] | \chi_i \rangle. \quad (3.17)$$

where the kinematic equations are

$$q_i^0 + p_i^0 = q_f^0 + p_f^0 = p_\Delta^0 \quad (3.18)$$

and

$$\vec{q}_i + \vec{p}_i = \vec{q}_f + \vec{p}_f = \vec{p}_\Delta \quad (3.19)$$

and the pionic isospin factor is given by [5]

$$C_\pi^2 = \left\{ \begin{array}{lll} 1 & \text{for} & \pi^+ p \rightarrow \pi^+ p \text{ and } \pi^- n \rightarrow \pi^- n \\ 1/3 & \text{for} & \pi^- p \rightarrow \pi^- p \text{ and } \pi^+ n \rightarrow \pi^+ n \\ \pm\sqrt{2}/3 & \text{for} & \pi^- p \rightarrow \pi^0 n \text{ and } \pi^+ n \rightarrow \pi^0 p \end{array} \right\}. \quad (3.20)$$

These three parameters have been determined by fitting the experimental cross sections for $\pi^-p \rightarrow \pi^-p$, $\pi^+p \rightarrow \pi^+p$ and $\pi^-p \rightarrow \pi^0n$ [28]. The resulting parameters are as follows [28]

$$M_\Delta = 1231 \text{ MeV} \quad (3.21)$$

$$\Gamma(Q) = 109 \left(\frac{|\vec{q}|}{|\vec{q}_\Delta|} \right)^3 \frac{M_\Delta}{Q} \frac{1 + (R|\vec{q}_\Delta|)^2}{1 + (R|\vec{q}|)^2} \text{ MeV} \quad (3.22)$$

$$G_3(Q) = \frac{g_3}{m_\pi} \sqrt{\frac{1 + (R|\vec{q}_\Delta|)^2}{1 + (R|\vec{q}|)^2}} \text{ MeV}^{-1} \quad (3.23)$$

where

$$R = 0.00552 \text{ MeV}^{-1} \quad (3.24)$$

$$g_3 = 2.13 \quad (3.25)$$

$$|\vec{q}| = \frac{1}{2Q} \sqrt{[Q^2 - (m + m_\pi)^2][Q^2 - (m - m_\pi)^2]} \quad (3.26)$$

$$|\vec{q}_\Delta| = \frac{1}{2M_\Delta} \sqrt{[M_\Delta^2 - (m + m_\pi)^2][M_\Delta^2 - (m - m_\pi)^2]}. \quad (3.27)$$

This leaves one parameter undetermined, the electromagnetic form factor $G_1(Q)$. This parameter may be determined by fitting the experimental cross sections for the reactions $\gamma n \rightarrow p\pi^-$ and $\gamma p \rightarrow n\pi^+$. This results in [28]

$$G_1 = g_1 \frac{M_\Delta + m}{m} \sqrt{\frac{4\pi}{137}}, \quad (3.28)$$

where

$$g_1 = 0.282. \quad (3.29)$$

The resulting values of all parameters are in good agreement with those determined from other models, and the theoretical calculations are in good agreement with the shapes of the experimental cross sections for all five reactions.

When $|\vec{p}_1| \gg |\vec{p}_2|$, the antisymmetrization in the quasi-free matrix element, \mathcal{M}_I , may be neglected, and the reduced cross section takes the simple form [28]

$$\frac{d\sigma}{d\vec{p}_2[d\Omega_\pi]_{cm}} = (1 + \beta_2 \cos \theta_2) \rho(|\vec{p}_2|) \frac{d\sigma}{[d\Omega_\pi]_{cm}}(Q, \omega), \quad (3.30)$$

where $\rho(|\vec{p}_2|)$ is the momentum distribution of the spectator nucleon, and ω is the angle between the photon and the pion momenta. This is the so-called spectator model, in which the dependence on the spectator nucleon is separated out through the factor $(1 + \beta_2 \cos \theta_2) \rho(|\vec{p}_2|)$. The other factor, $d\sigma/[d\Omega_\pi]_{cm}(Q, \omega)$, is the cross section for the elementary reaction $\gamma n \rightarrow p\pi^-$, and depends only on Q and ω .

Once the quasi-free contribution is calculated a comparison to the experimental data may be made. This allows a check on the deviations from the quasi-free contribution. As may be seen from Figure 3.6, for small values of the spectator nucleon momentum, the agreement is quite good. Deviations start to appear above $p_2 \sim 200$ MeV/c, indicating the need for calculating the FSI contributions in this region [27].

FSI effects may be further examined by looking in specific regions of phase space where certain diagrams have important contributions. For example, if Q , ω and p_2 are kept constant, deviations from the quasi-free distribution may be examined by plotting these deviations against the scattering angle of the spectator nucleon. Figure 3.7 shows such a plot at a small value of the spectator nucleon momentum ($p_2 = 50$ MeV/c). As expected, deviations from the quasi-free diagram calculation at this momentum are quite small [2]. Figure 3.8 shows the same kind of plot where p_2 is fixed at a value of 400 MeV/c to suppress the quasi-free contribution [3]. In this case strong deviations are seen. These deviations may be accounted for by considering the contributions from other diagrams. The details of which are discussed in the next few sections.

The quasi-free diagram is adequate in describing the experimental data for small

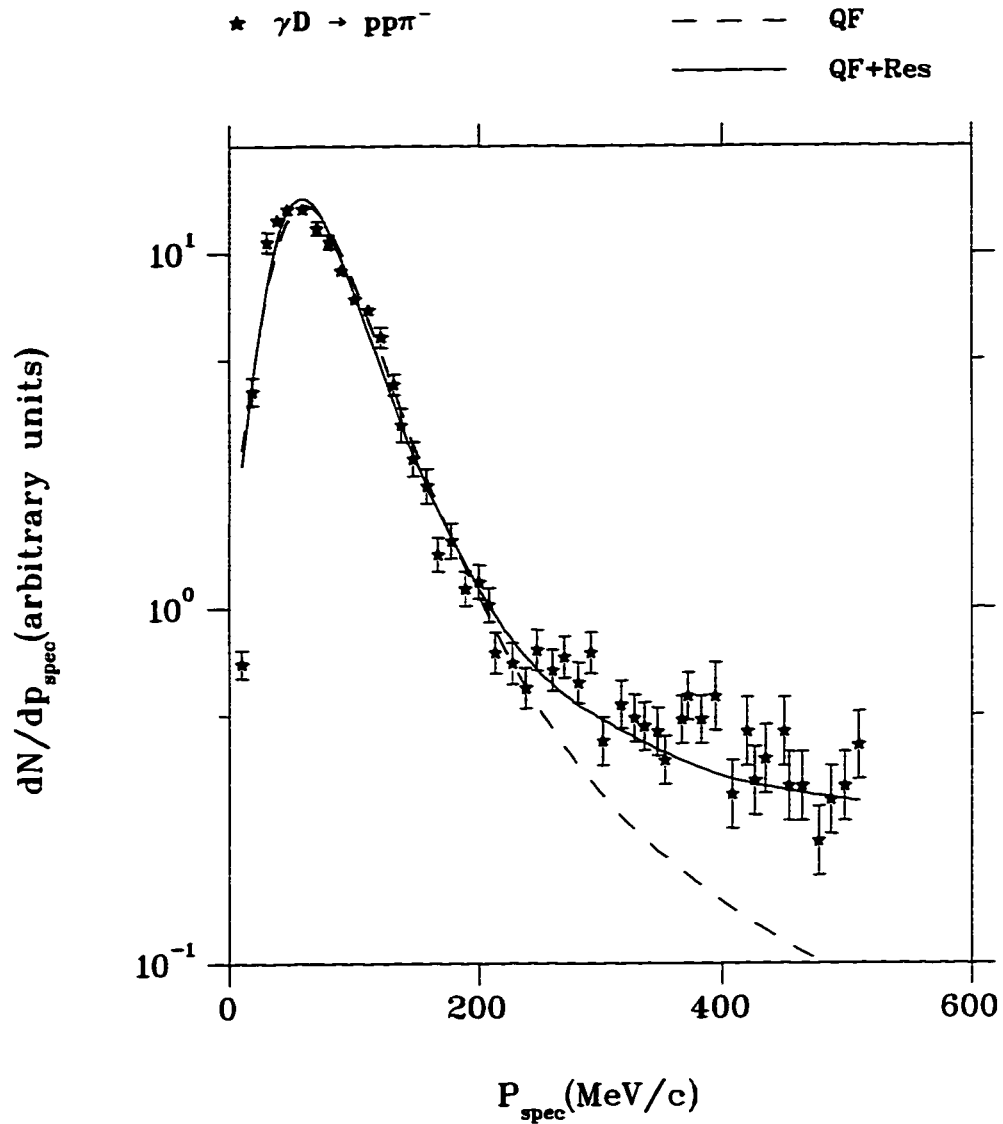


Figure 3.6: Experimental yield for $\gamma D \rightarrow pp\pi^-$. The experimental points are obtained at DESY by Benz et al. [4]. The theoretical curves are calculated by J.M. Laget [27]. The dashed curve includes only the quasi-free diagram. The solid curve includes rescattering effects as well.

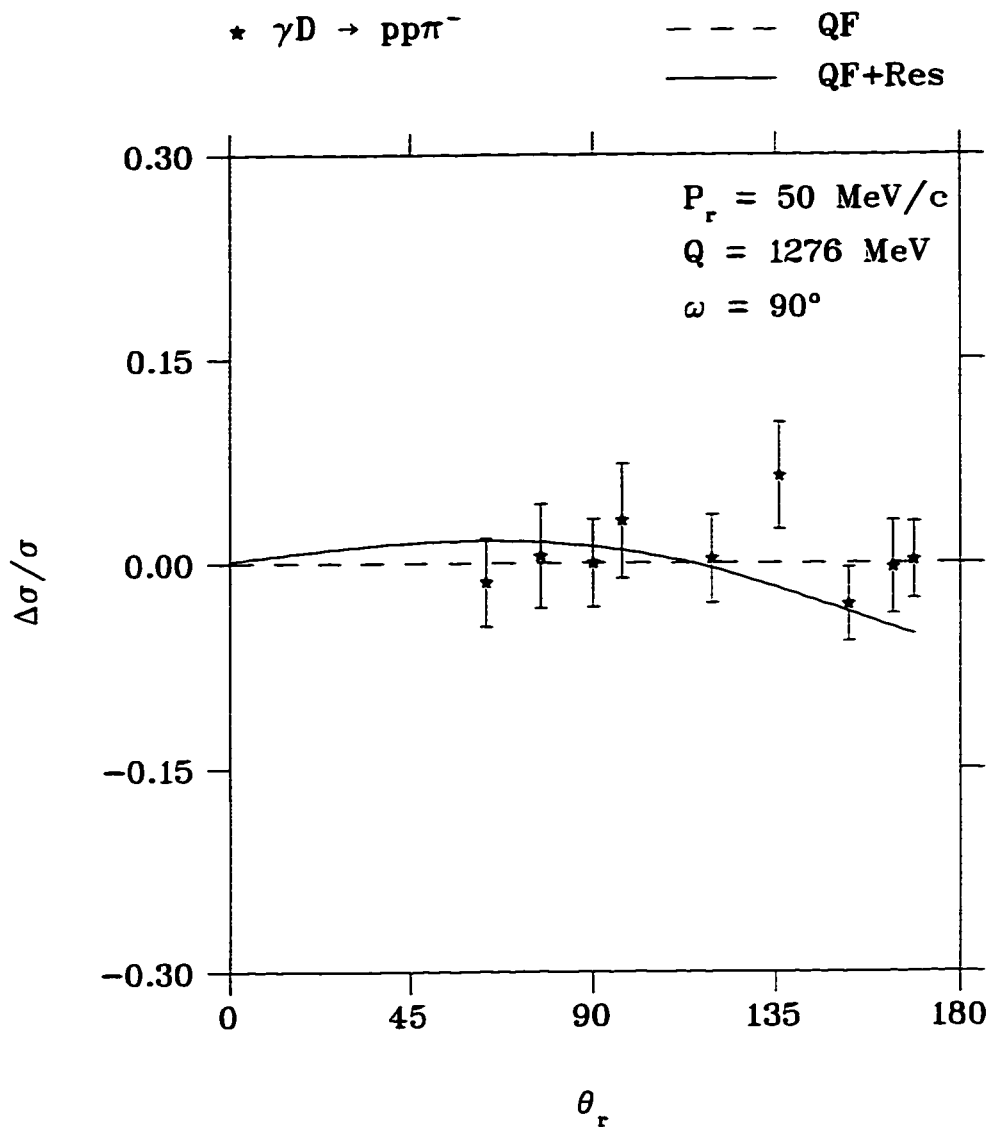


Figure 3.7: Deviations from the spectator nucleon model for $\gamma D \rightarrow pp\pi^-$ at a spectator nucleon momentum of 50 MeV/c. The experimental data are obtained at Saclay by Argan et. al. [2]. The theoretical curves are calculated by J.M. Laget [25].

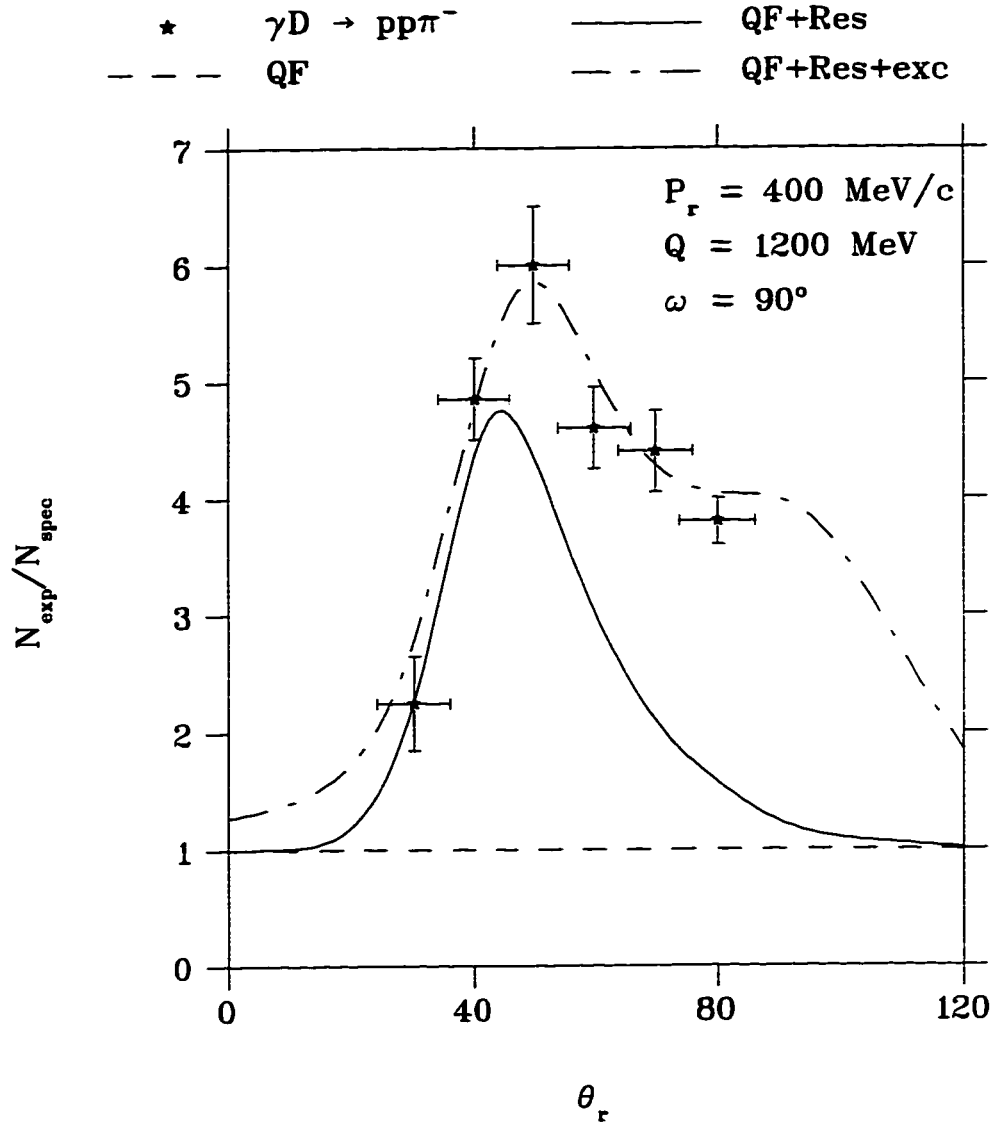


Figure 3.8: Deviations from the spectator nucleon model for $\gamma D \rightarrow pp\pi^-$ at a spectator nucleon momentum of 400 MeV/c. The experimental data are obtained at Saclay by Argan et al. [3]. The theoretical curves are calculated by J.M. Laget [3]. The solid curve includes $\pi - N$ rescattering, whereas the dot dashed curve includes meson exchange currents as well.

values of the spectator nucleon momentum ($p_2 < 200$ MeV/c). In this region, the elementary reaction $\gamma n \rightarrow p\pi^-$ may be extracted from the $\gamma D \rightarrow pp\pi^-$ reaction cross section in the framework of the spectator model. The data may be compared to the full calculation of the elementary transition amplitude as in Figure 3.9. The calculation may also be compared to the $\gamma p \rightarrow n\pi^+$ reaction cross section. In both cases the agreement is quite good and yields confidence in the calculation of the elementary transition amplitude [5].

3.3.2 Rescattering Effects

The first contribution to the FSI's to be considered is that of the one loop diagrams. These are the $\pi - N$ and $N - N$ rescattering effects (diagrams II and III in Figure 3.5, respectively). The quasi-free diagram together with these two diagrams accounts for the bulk part of the total $\gamma D \rightarrow pp\pi^-$ cross section, as may be seen from Figure 3.6. Although the contributions of these two diagrams to the total cross section is small relative to the quasi-free diagram, their effects may be examined by focusing on the regions of phase space where they are expected to be large. In the next two sections Laget's calculation for these two diagrams is presented and compared to experimental data.

3.3.2.1 $\pi - N$ Rescattering

Two possible absorption mechanisms contribute to this process. In the first case the photon gets absorbed on a neutron, as in the quasi-free case. This results in producing a proton and a π^- . The second vertex in this case will thus correspond to $\pi^- p \rightarrow \pi^- p$ scattering. In the second case the photon gets absorbed on a proton resulting in a

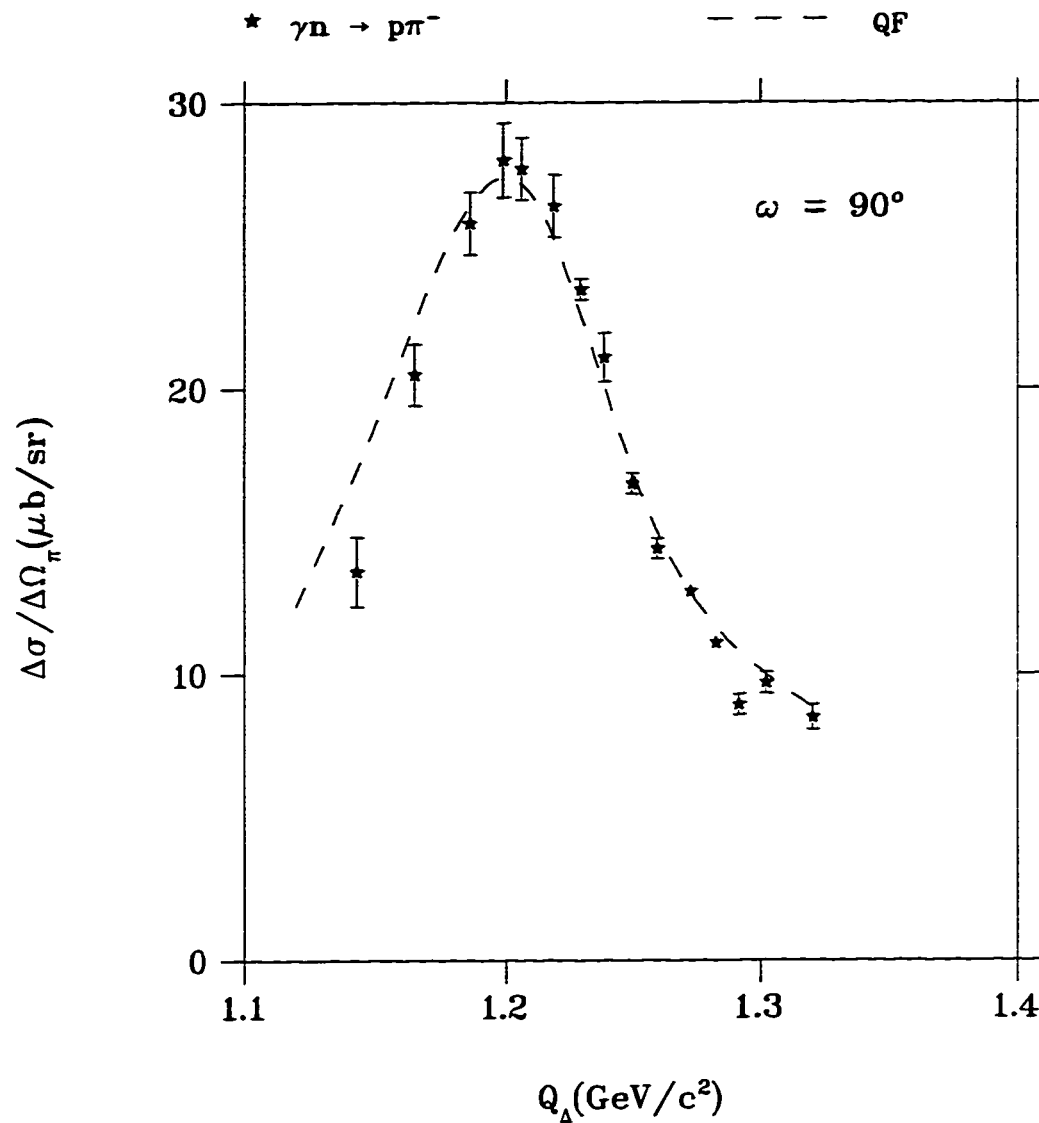


Figure 3.9: Scattering cross section for $\gamma n \rightarrow p\pi^-$ as extracted from the $\gamma D \rightarrow pp\pi^-$ reaction cross section at a spectator nucleon momentum of 50 MeV/c. The experimental points are obtained at Saclay by Argan et al. [2] The theoretical curves are calculated by J.M. Laget [25].

proton and a π^0 . The second vertex will then correspond to $\pi^0 n \rightarrow \pi^- p$ scattering. The matrix element for this diagram may be written as [26]

$$\mathcal{M}_{II}(\vec{k}, \epsilon, \vec{\mu}, M, \vec{p}_1, m_1, \vec{p}_2, m_2) = -i \sum_{m_n, m_p} \langle \frac{1}{2} m_n \frac{1}{2} m_p | 1M \rangle \int \frac{d^3 \vec{p}}{(2\pi)^3} \frac{1}{\sqrt{4\pi}} \frac{u_o(p) T_{\gamma, N} \widehat{T}_{\pi, N}}{q^2 - m_\pi^2 + i\epsilon}. \quad (3.31)$$

where

$$T_{\gamma, N} \widehat{T}_{\pi, N} = [T(\gamma n \rightarrow \pi^- p) T(\pi^- p \rightarrow \pi^- p) - T(\gamma p \rightarrow \pi^0 p) T(\pi^0 n \rightarrow \pi^- p)]. \quad (3.32)$$

and q^2 is the square of the pion four momentum

$$q^2 = (q^0)^2 - (\vec{q})^2. \quad (3.33)$$

Only the s-wave contribution of the deuteron wave function, $u_o(p_2)$, has been considered. Similarly the particular choice of the deuteron wave function is not important, as they yield similar results in the low momentum range. This was verified by considering both the Hulthén soft-core wave function and the McGee parametrization of the Hamada-Johnston wave function (which are identical up to $p \sim 300$ MeV/c) in the calculation of the matrix element [25].

This matrix element may be written as a sum of an on-shell ($q^2 = m_\pi^2$) and an off-shell term. The on-shell term has the major contribution, however, and no ambiguity arises from the choice of the off-shell continuations [5].

The $\pi - N$ rescattering diagram is particularly interesting as the rescattering amplitude has a singularity that comes close to the physical region at a spectator nucleon scattering angle $\theta_2 = 45^\circ$. Figure 3.8 shows the deviations from the quasi-free diagram contribution [3]. The singularity is clearly apparent in the experimental data. The dashed curve includes $\pi - N$ rescattering as in the calculation above. Although the

curve follows the general trend of the data, it falls short of accounting for the full cross section, particularly at higher values of θ_2 . Deviations from this calculation may be accounted for by considering meson exchange current corrections. When two pions are produced below the double pion photoproduction threshold, one of these pions is virtual, and is photoproduced at one nucleon and reabsorbed by the other, as is shown in Figure 3.10. This pion is similar to that produced in the photodisintegration of the deuteron below the single pion threshold. Above the double pion photoproduction threshold, the contribution of this mechanism to the total photoabsorption cross section becomes important. As can be seen from Figure 3.2, at 650 MeV the contribution of the $\gamma N \rightarrow N\pi\pi$ channel to the cross section is about 2/3 the contribution of the $\gamma N \rightarrow N\pi^+$ channel [27].

The predictions of this pion exchange amplitude are too high unless a form factor is used at each pion-baryon vertex and the exchange of ρ -mesons is allowed [26]. This results in the dot-dashed curve of Figure 3.8. This effect may be further examined by looking in a region of phase space where both the quasi-free diagram and the single $\pi - N$ rescattering diagram are suppressed, as in Figure 3.11 [3]. An excellent agreement is seen there as well. It is worth noting, however, that the kinematic regions for both Figures 3.8 and 3.11 are not accessible by our SALAD experiment as they correspond to a $300 \text{ MeV} < E_\gamma < 600 \text{ MeV}$.

The πNN form factor used in this calculation is taken to be of the form [26]

$$F_\pi(q_\pi^2) = \frac{\Lambda_\pi^2 - m_\pi^2}{\Lambda_\pi^2 - q_\pi^2} \quad (3.34)$$

while the $\rho - N$ form factor is taken to be of the form [26]

$$F_\rho(q_\rho^2) = \left(\frac{\Lambda_\rho^2 - m_\rho^2}{\Lambda_\rho^2 - q_\rho^2} \right)^2, \quad (3.35)$$

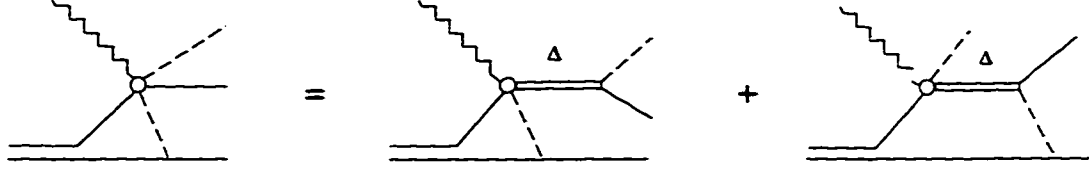


Figure 3.10: Meson exchange Feynman diagrams for $\gamma D \rightarrow pp\pi^-$.

where $q_\pi^2(q_\rho^2)$ is the π (ρ) squared four momentum, and the cut off masses are Λ_π and Λ_ρ for the π and ρ , respectively.

The value of Λ_ρ is chosen to be $2m_N$ (where m_N is the nucleon mass) according to the vector meson dominance model. This leaves two free parameters in this calculation: the pion cutoff mass, Λ_π , and the ratio of the squares of the ρNN to the πNN coupling constants G_ρ^2/G_π^2 . These two parameters have been determined from the $\gamma D \rightarrow pn$ cross section independently in two different kinematic regions, yielding: $\Lambda_\pi=1.2$ GeV and $G_\rho^2/G_\pi^2=1.6$ [26, 29]. The latter value is in agreement with $N-N$ and $\pi-N$ cross section analyses as well.

3.3.2.2 $N-N$ Rescattering

The second single rescattering effect to be considered here is $N-N$ rescattering, which corresponds to diagram III in Figure 3.5. The matrix element for this diagram is given by [5]

$$\mathcal{M}_{III}(\vec{k}, \epsilon, \vec{\mu}, M, \vec{p}_1, m_1, \vec{p}_2, m_2) = -i \sum_{m_n, m_p, m_p'} \langle \frac{1}{2}m_n \frac{1}{2}m_p | 1M \rangle \times$$

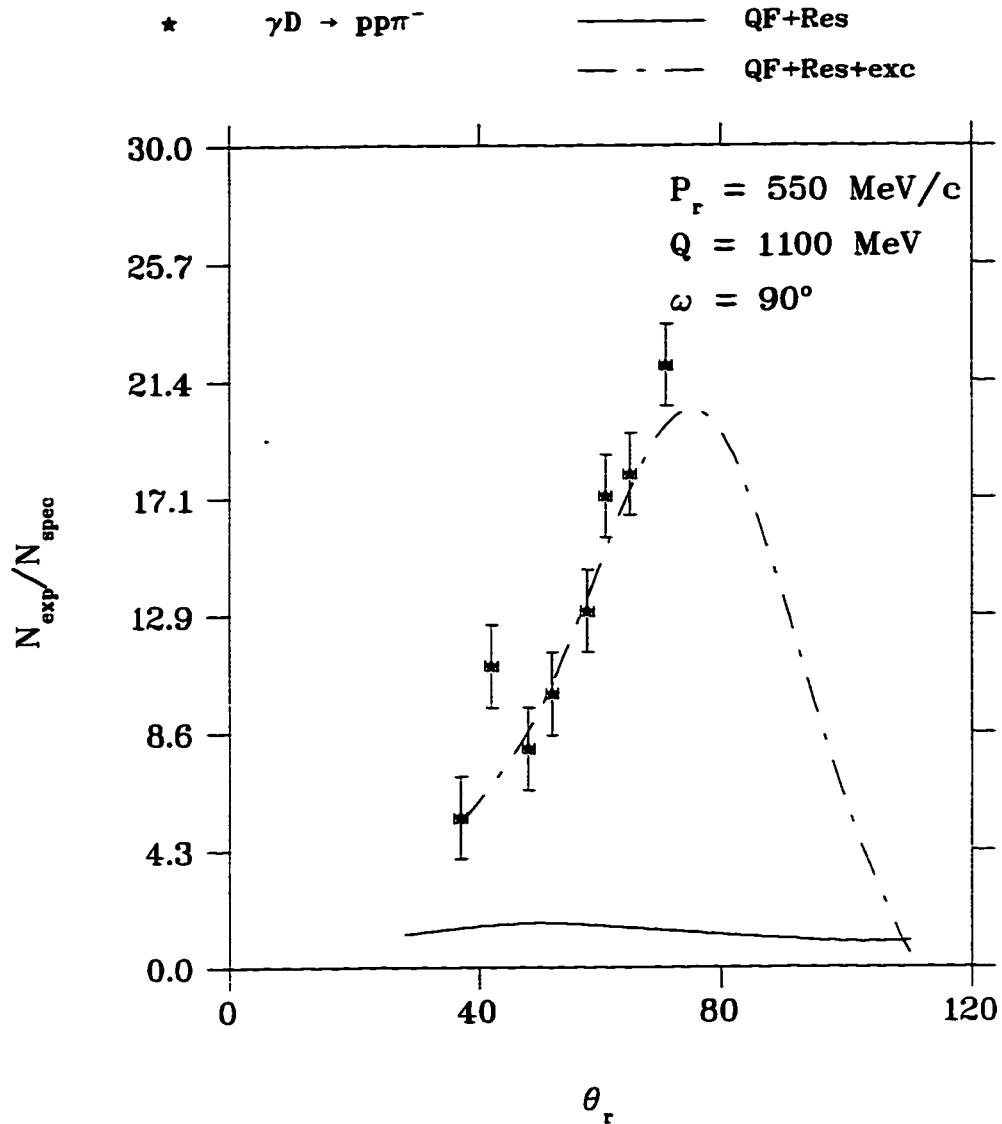


Figure 3.11: Deviations from the spectator nucleon model for $\gamma D \rightarrow pp\pi^-$ at a spectator nucleon momentum of 550 MeV/c. The experimental data are obtained at Saclay by Argan et. al. [3]. The theoretical curves are calculated by J.M. Laget [3]. The solid curve includes $\pi-N$ rescattering, whereas the dot dashed curve includes meson exchange currents as well.

$$\int \frac{d^3\vec{p}}{(2\pi)^3} \frac{1}{\sqrt{4\pi}} \frac{u_o(p)T(\gamma n \rightarrow p\pi^-)T(pp \rightarrow pp)}{p^{\circ'} - E'_p + i\epsilon}, \quad (3.36)$$

The quantities $p^{\circ'}$ and E'_p which appear in the denominator are the off-shell and on-shell energies given, respectively, by

$$p^{\circ'} = E - \sqrt{p^2 + m^2} \quad (3.37)$$

and

$$E'_p = \sqrt{(\vec{P} - \vec{p})^2 + m^2}, \quad (3.38)$$

where p is the momentum of the deuteron internal proton and \vec{P} and E are the sum of the outgoing protons momentum and energy given by

$$\vec{P} = \vec{p}_1 + \vec{p}_2 \quad (3.39)$$

and

$$E = p_1^0 + p_2^0. \quad (3.40)$$

The contribution of the $N - N$ rescattering mechanism becomes important when the relative kinetic energy of the nucleons is small. In the energy range between threshold and a few tens of MeV above threshold, $N - N$ rescattering becomes important, and the cross section is enhanced by up to six times compared to the quasi-free cross section. Figures 3.12 and 3.13 show the contribution of this mechanism at higher energies ($E_\gamma = 299$ MeV) to the $\gamma D \rightarrow pp\pi^-$ and the $\gamma D \rightarrow nn\pi^+$ cross sections [28]. When the pion momentum is high, the relative momentum of the nucleons is small and strong effects of $N - N$ rescattering are apparent. Comparison of the $\gamma D \rightarrow pp\pi^-$ and the $\gamma D \rightarrow nn\pi^+$ cross sections in this region show the different contributions to $N - N$ scattering due to the Coulomb force.

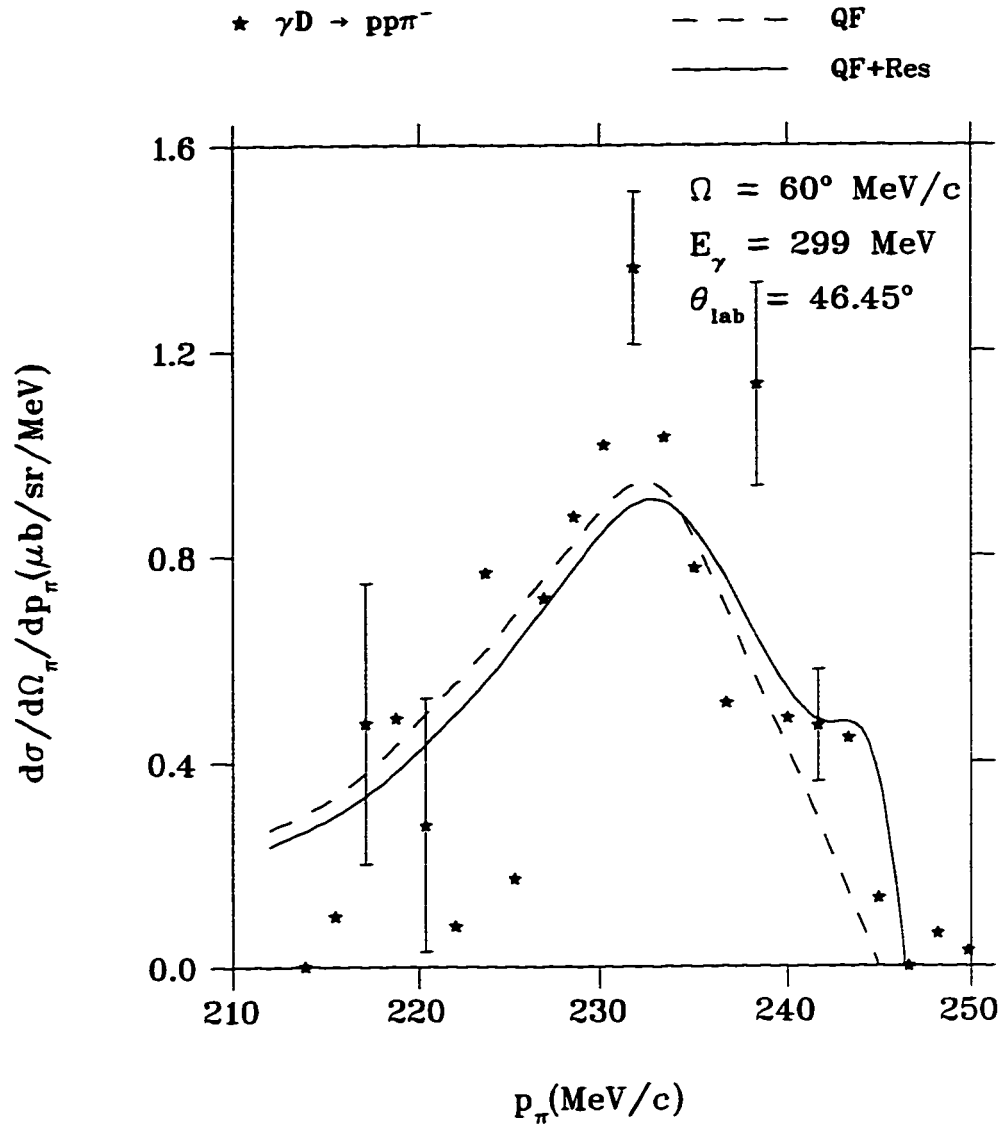


Figure 3.12: Differential cross section for $\gamma D \rightarrow pp\pi^-$ reaction. The experimental data are obtained at Saclay by Ardiot et al. [28]. The theoretical curves are calculated by J.M. Laget [28]. The dashed curve includes only the quasi-free diagram, whereas the solid curve includes $N - N$ rescattering as well.

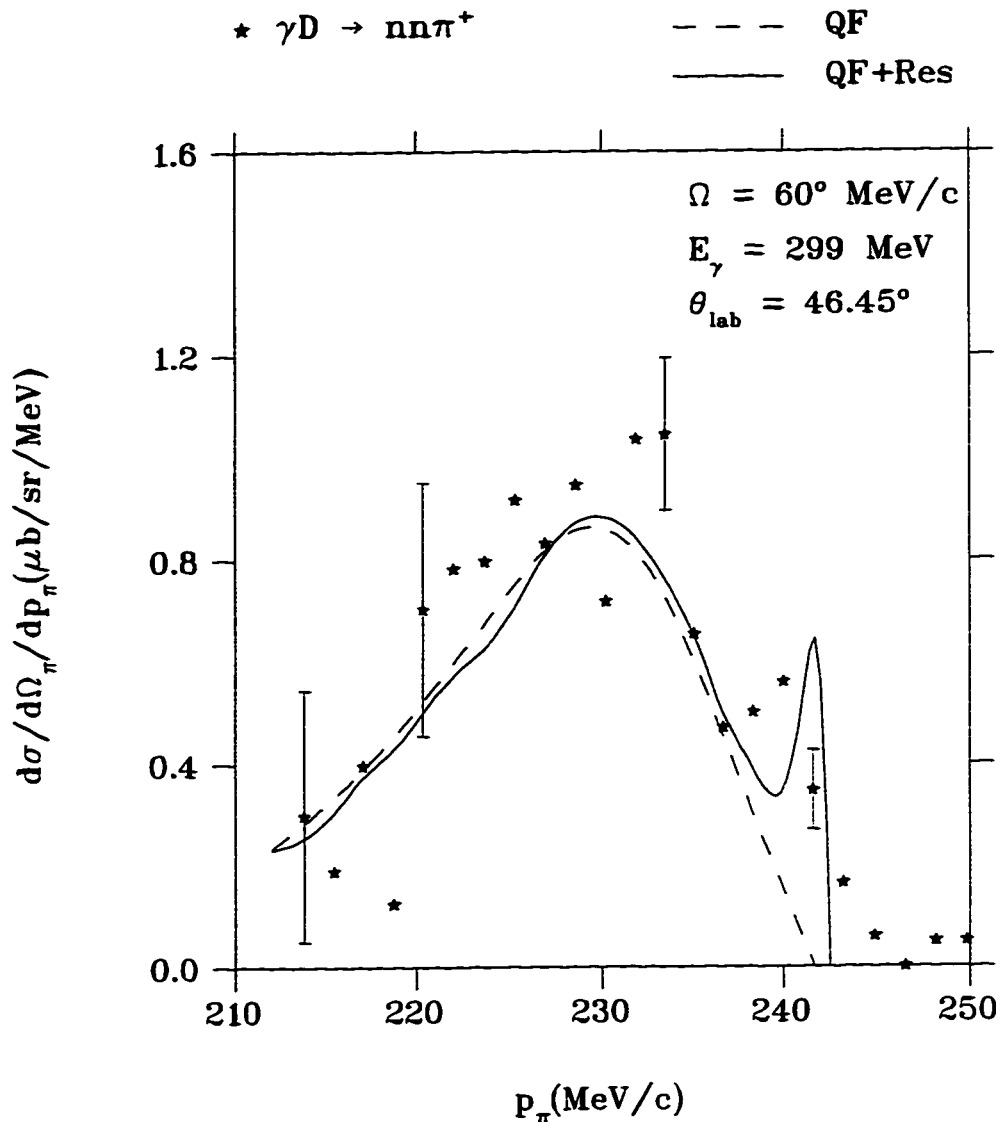


Figure 3.13: Differential cross section for $\gamma D \rightarrow nn\pi^+$ reaction. The experimental data are obtained at Saclay by Ardiot et al. [28]. The theoretical curves are calculated by J.M. Laget [28]. The dashed curve includes only the quasi-free diagram, whereas the solid curve includes $N - N$ rescattering as well.

3.3.3 Two-loop Diagrams

Possible two loop diagrams are also shown in Figure 3.5 (diagrams IV, V and VI). The contribution of diagram V has been calculated and found negligible. Diagram VI contributes only in limited regions of the phase space and has been neglected. Only diagram IV is included. The interaction matrix corresponding to this diagram is given by [28]

$$\begin{aligned} \mathcal{M}_{IV}(\vec{k}, \epsilon, \vec{\mu}, M, \vec{p}_1, m_1, \vec{p}_2, m_2) = & \int \frac{d^3 \vec{p}'}{(2\pi)^3} \frac{1}{q^2 - m_\pi^2 + i\epsilon} \\ & \{ \mathcal{M}_{III}^{pp}(\vec{k}, \epsilon, \vec{\mu}, M, \vec{p}', m_p'', \vec{p}_2, m_2) T(\pi^- p \rightarrow \pi^- p) \\ & + \mathcal{M}_{III}^{np}(\vec{k}, \epsilon, \vec{\mu}, M, \vec{p}', m_p'', \vec{p}_2, m_2) T(\pi^0 n \rightarrow \pi^- p) \}, \end{aligned} \quad (3.41)$$

where two terms appear on the right hand side of this equation to account for the exchange of charged as well as neutral pions (see section 3.3.2.1). The matrix elements \mathcal{M}_{III}^{pp} and \mathcal{M}_{III}^{np} are given by the single rescattering $N - N$ diagrams (see equation 3.36. and the transition matrix elements of the form $T(\pi N \rightarrow \pi N)$ are given by equation 3.17.

The argument that multiple scattering effects are small is supported by the fact that the behaviour of the data are well accounted for by the one loop diagram for both $\pi - N$ and $N - N$ rescattering, as was evident in the various comparison plots shown in the previous sections.

3.3.4 The $\Delta - N$ Interaction

The $\Delta - N$ interaction may be divided into two parts: the long range $\Delta - N$ interaction which results from the decay of the Δ inside the nucleus, and thus reduces to the multiple scattering effects that have been discussed in the previous sections. The other

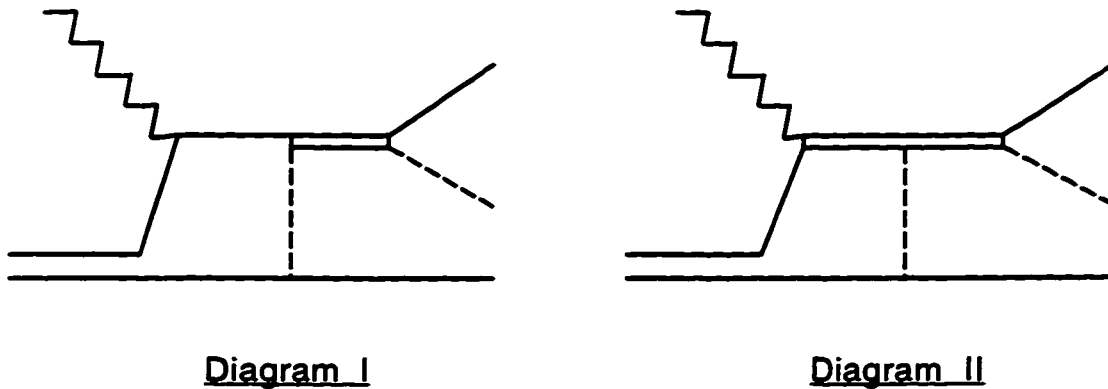


Figure 3.14: Feynman diagrams for the $\Delta - N$ interaction.

part results from the propagation of the Δ inside the nucleus and may be considered as the short range part of the $\Delta - N$ interaction. Comparisons of previous data to a calculation which includes single rescattering effects as well as the two loop diagram discussed above show significant deviations in some regions of phase space, particularly near the $\Delta - N$ threshold [28].

As previously mentioned, contributions from diagrams with more than two loops are expected to be small and are not expected to account for the observed deviations. In fact, these deviations are far from any dominant singularities in the multiple scattering series. Two other possibilities may be considered. The first is that the deviations in the cross section are due to underlying dibaryonic resonances due to quark-quark interactions [8, 18]. The second possibility is that the observed deviations are due to the part of the $\Delta - N$ interaction which does not reduce to the multiple scattering series. Figure 3.14 shows the Feynman diagram corresponding to this interaction.

A full treatment of the $\Delta - N$ interaction requires a solution to the relativistic three body πNN system allowing pion emission and absorption. Such a treatment is quite complicated, and instead an approximate treatment is considered by Laget in which

the Δ is treated as a stable particle, thus reducing the problem to the usual two-body channel. Such a solution, although not accurate, would still help to understand the general nature of the deviations.

When the photon couples directly to the Δ , the Δ may rescatter off the spectator proton. If the Δ is treated as a stable particle, an analytic expression may be obtained for the interaction matrix with the same method used to obtain $\pi - N$ and $N - N$ rescattering effects. The width of the Δ is then included by using a Breit-Wigner factor. The photon may also couple to one nucleon and the formation of the Δ may occur through an $NN \rightarrow N\Delta$ transition. Consideration of this channel is very important since interference effects with the $\Delta - N$ elastic scattering channel are expected, particularly near threshold [28]. The structure near the $N\Delta$ threshold is better accounted for when the short range $\Delta - N$ interaction is considered. Although the agreement is not too good, the calculation shows that the $\Delta - N$ interaction is indeed of the same order of magnitude as the deviations from the multiple scattering series, and has approximately the same variation with energy [28]. In fact, good agreement is not expected since several approximations were made in the calculation and not all possible partial waves were considered. This result suggests that a full treatment of the short range $\Delta - N$ interaction is likely to account for the structure at the $N\Delta$ threshold, and a dibaryon resonance is not expected. However, the calculation fails to account for deviations in other regions of phase space, and these deviations remain to be understood.

A possible dibaryonic resonance in the $N - \Delta$ final state was also considered and failed to account for the deviations. These deviations, however, do not ascertain the presence of a process different from those considered above, since the calculation of the short range $N - \Delta$ interaction is too crude to allow for definite conclusions. To be

able to draw any valuable conclusions about such deviations, two things are required. On the theoretical side, a complete treatment of the $\Delta - N$ interaction is needed. On the experimental side, a better understanding of the $\Delta N \rightarrow \Delta N$ elastic scattering is required for which the $\gamma D \rightarrow pp\pi^-$ reaction is best suited.

The short range $\Delta - N$ interaction has also been investigated in other reaction processes, particularly in $\pi - D$ elastic scattering and $\pi - D$ breakup. Independent calculations of the $\pi - D$ scattering channel tend to disagree with the data, and are typically off by a factor of 2 in some regions of phase space [15]. For $\pi D \rightarrow \pi NN$, the deviations are less dramatic, but are still statistically significant.

Ferreira and Dosch attempted to account for these deviations by considering a short range $\Delta - N$ interaction [1, 11, 14]. Their method was to calculate a T matrix for the $\Delta - N$ elastic scattering in the intermediate state. The T matrix was parametrized in terms of the inelasticity η and the phase shift δ , and the result was added to the $\pi - D$ elastic scattering amplitude. The best values of the parameters η and δ were then determined by fitting the experimental data.

The availability of experimental data for the $\pi - D$ scattering in which the deuteron target was polarized have allowed for several distributions to be considered in the fit. These calculations have resulted in an improved agreement in both $\pi - D$ elastic scattering and breakup channels. These calculations result in increased confidence that the missing ingredient in the theory is indeed the short range $\Delta - N$ interaction, and stress the need for more experimental data from other reactions to allow for a consistency check.

Chapter 4

Analysis

The data analysis process proceeds in two steps. First, the detector needs to be calibrated. This includes wire chamber calibrations (ADC pedestals, z position calibrations, efficiency calculation, and position resolution) and scintillator calibrations (ADC pedestals, gains, light correction, attenuation lengths, and energy resolution). The detector calibrations were discussed in the second chapter. The second step is to reconstruct each event (determine the angles and energies of outgoing particles), and extract the $D(\gamma, pp\pi^-)$ events from the background, the details of which are discussed in this chapter.

Once this is achieved a Monte Carlo simulation is required. The Monte Carlo serves two purposes. First, it demonstrates our understanding of the detector by comparing the various distributions of the raw histograms generated by the Monte Carlo simulation to those obtained from the actual data, such as the radial position of the vertex and the minimum distance between tracks. Second, a Monte Carlo simulation is necessary to calculate the efficiency of the detector, required to calculate the $D(\gamma, pp\pi^-)$ cross

section. A detailed discussion of the Monte Carlo simulation is presented here. The efficiency calculation is presented in the next chapter.

4.1 Data Analysis

4.1.1 Track Reconstruction

For each event, the SALAD tracking subroutine searches all the wires in the four chambers for a hit. A valid hit requires the presence of an ADC signal at each end of the wire, and that the sum of the ADC signals from both ends of the wire exceeds a set threshold. When two or more hits are found, such that at least one of the hits is in the outer chambers (3 or 4) and at least one is in the inner chambers (1 or 2), track reconstruction is carried out. The ϕ coordinate of a hit is identified by the position of the wire displaying the hit, whereas the z position is determined from charge division. The (x,y) position of a hit may be determined from the known radial position of the wire and the value of ϕ .

The search for wire chamber hits starts from the outer wire chambers, since they have the lowest count rate. When a hit is found in chamber 4, three wires in chamber 3 nearest the struck wire. If a hit is found there, the difference in the z position of the two hits is determined. If the difference is less than 200 mm, the two hits are assumed to be correlated and the search proceeds to the inner chambers in which wires consistent with a track originating in the target region are searched. The search continues until all wires in the outer wire chambers are searched. The direction of the track \hat{t} is defined by the vector sum over all possible vectors, \vec{r}_i , defined by any two hits

$$\hat{t} = \frac{1}{N} \sum_{i>j} \frac{(\vec{r}_i - \vec{r}_j)}{|\vec{r}_i - \vec{r}_j|}. \quad (4.1)$$

When more than two hits are associated with a given track, the track is over-determined and will not pass directly through the points defined by the hits. The minimum distance d_i between each hit and the above-defined track is then

$$d_i = | \hat{t} \times \vec{v}_i |, \quad (4.2)$$

where \vec{v}_i is the vector defined by the hit in a given wire chamber (in the SALAD coordinate system). A tracking residual is defined such that

$$R = \sum_i \frac{d_i}{N}, \quad (4.3)$$

where N is the total number of hits. When the search is complete and all possible tracks are reconstructed, the tracks are sorted by their residual value. Since a residual value may not be calculated for a two-hit track, such tracks are assigned a high residual value so that tracks with higher multiplicity of hits are given higher priority. If two or more tracks share the same hit, only the one with the lowest residual value is considered. Table 4.1 shows the distribution of track multiplicities per event found in a typical run. The majority of the background results from $\gamma \rightarrow e^+e^-$ pair production. The majority of one and two track events result from this background. The requirement that a tagger signal be present does not eliminate this background since these events may be produced by photons that have energies in the tagged region. The $D(\gamma, pp\pi^-)$ analysis was therefore confined to three track events. This requirement results in removing most of the background. A typical reconstructed three track $D(\gamma, pp\pi^-)$ event is shown in Figure 4.1.

When two or more tracks result from a single event, they should originate from a single point in the target region near the detector axis. Resolution effects result in a non-zero calculated minimum distance between these tracks. When only one track is

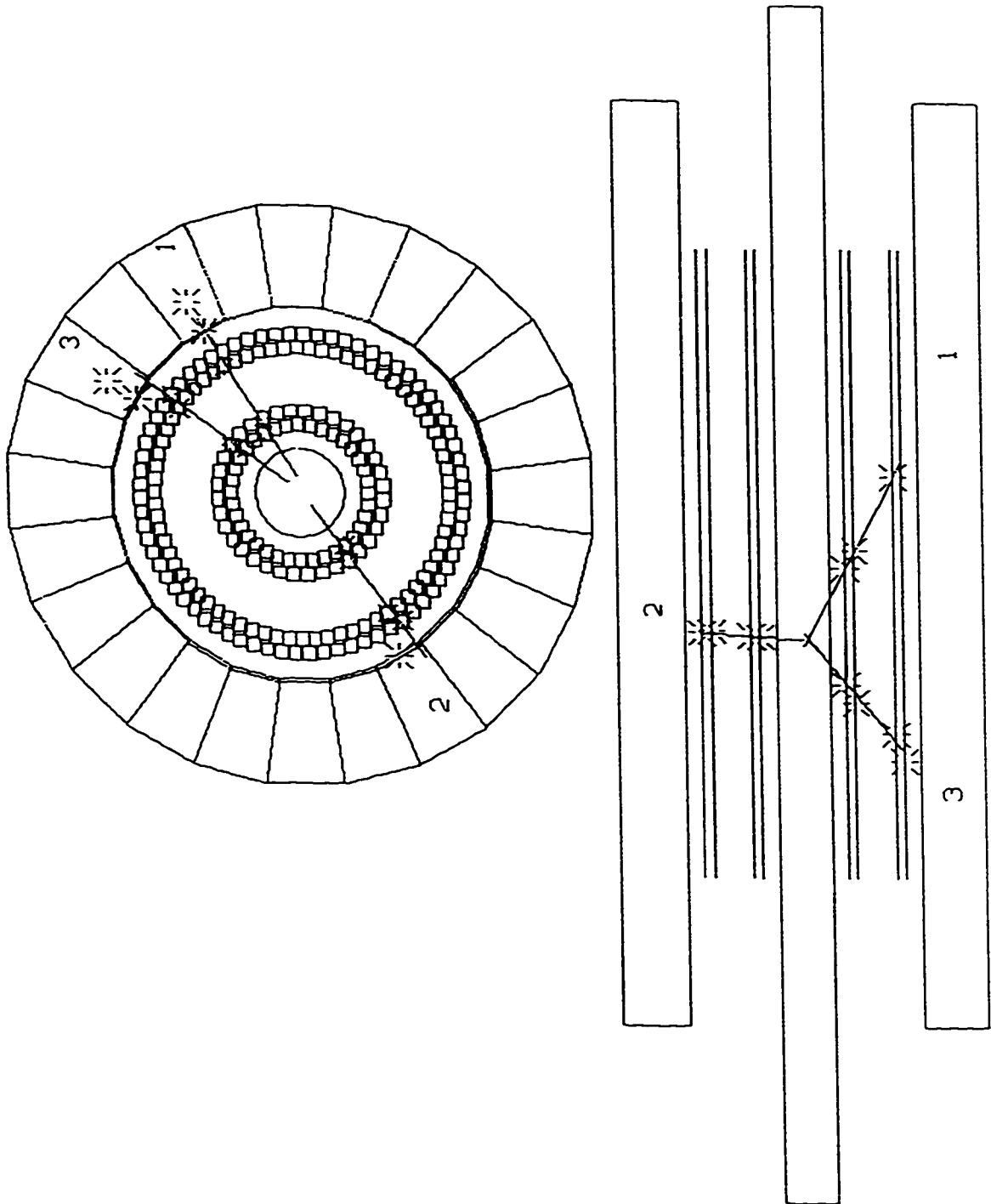


Figure 4.2: A typical reconstructed three track $D(\gamma, pp\pi^-)$ event as seen in SALAD.

Number of tracks per event	Counts	Percentage
1	296,060	50%
2	283,383	48%
3	7,591	1%
≥ 4	492	$< 0.1\%$

Table 4.1: Distribution of track multiplicities found in a typical $D(\gamma, pp\pi^-)$ run.

present, the vertex is defined to be the point on the track closest to the detector axis. For two track events, the vertex is defined to be the mid-point of the line segment joining the two tracks at their closest approach as illustrated in Figure 4.2. When more than two tracks are required, a temporary vertex is defined for the two tracks with the smallest minimum distance as described above. The minimum distances between the other tracks and this temporary vertex are then calculated, and the tracks are considered correlated if this minimum distance is less than 40 mm. The minimum distance between tracks for the event is defined to be the average of the minimum distances resulting from all possible two track permutations, and referred to as the *mindis*. The event vertex is taken to be the mid-point of *mindis*.

The z position of the vertex, z_{vtx} , should lie within the target volume. A cut was therefore applied such that

$$-1200 \text{ mm} < z_{vtx} < 1200 \text{ mm}. \quad (4.4)$$

A second cut was also applied on z_{vtx} since a CH_2 target (~ 2 mm thick) was placed inside the deuterium target. A reasonable cut was determined such that events with

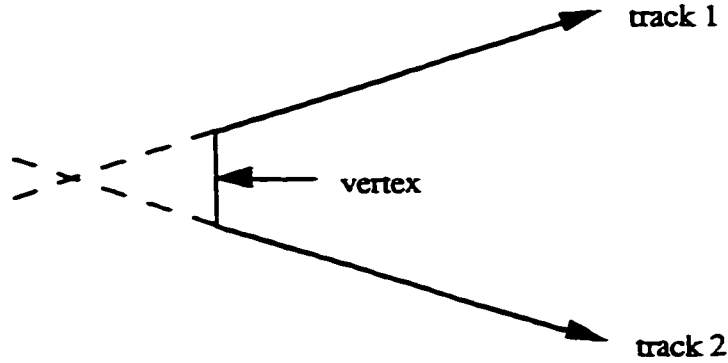


Figure 4.2: Vertex definition for two track events.

z_{vtx} in the range

$$157 \text{ mm} < z_{vtx} < 237 \text{ mm} \quad (4.5)$$

were rejected. The z_{vtx} distribution from a typical run is shown in Figure 4.3 for events with track multiplicities ≥ 1 . The spike is due to events coming from the solid target. The bump at small z values is background. The nature of this background may be clearly seen in the two dimensional histogram of θ versus z displayed in Figure 4.4. In the range of our photon energy, the expected background is mainly due to $\gamma \rightarrow e^+e^-$ pair production. At high energies the electron-positron pair have a mean opening angle given by [12]

$$\theta = \frac{m_e c^2}{E_e} \quad (4.6)$$

where m_e is the electron mass, c is the speed of light, and E_e is the electron energy. In our energy range the electron-positron pair have a small opening angle and thus have a better chance of being detected if they originate from the upstream end of the detector. For example, at $E = 100 \text{ MeV}$, this formula gives a mean opening angle of 0.29° .

A large portion of this background is rejected once a three track requirement is imposed. Figure 4.5 shows the z position of the vertex for three track $D(\gamma, pp\pi^-)$ events

after the final cuts (to be discussed later) were applied; the solid curve is a Monte Carlo simulation.

The radial position of the vertex distribution is shown in Figure 4.6. The data in the top plot consist of three track $D(\gamma, pp\pi^-)$ events before the final cuts are applied. A cut was applied to this distribution at 30 mm as shown in the figure. The position of this cut was determined by comparing the data with the Monte Carlo simulation. This results in cutting 16% of the remaining events. The bottom plot shows the same distribution after the final cuts were applied; the solid histogram is a Monte Carlo Simulation.

Figure 4.7 shows the *mindis* distribution after the final cuts were applied. The solid curve is a Monte Carlo simulation. As may be seen from the figure, once the final cuts are applied, the remaining events match the *mindis* distribution predicted from the Monte Carlo simulation. No cuts were imposed on this distribution.

4.1.2 Particle Identification

The energy loss by a particle traversing a given material depends on the charge and velocity of that particle. The energy loss per unit length may be calculated theoretically and is given, to a very good approximation, by the Bethe-Bloch formula [38, 12]

$$\frac{dE}{dx} = C_1 \left(\frac{z}{\beta}\right)^2 [\ln(C_2 \beta^2 \gamma^2) - \beta^2], \quad (4.7)$$

where C_1 and C_2 are constants that depend on the material type, and z is the charge of the incident particle. The energy loss depends on the particle's velocity through β and γ , where

$$\beta = \frac{v}{c}, \quad (4.8)$$

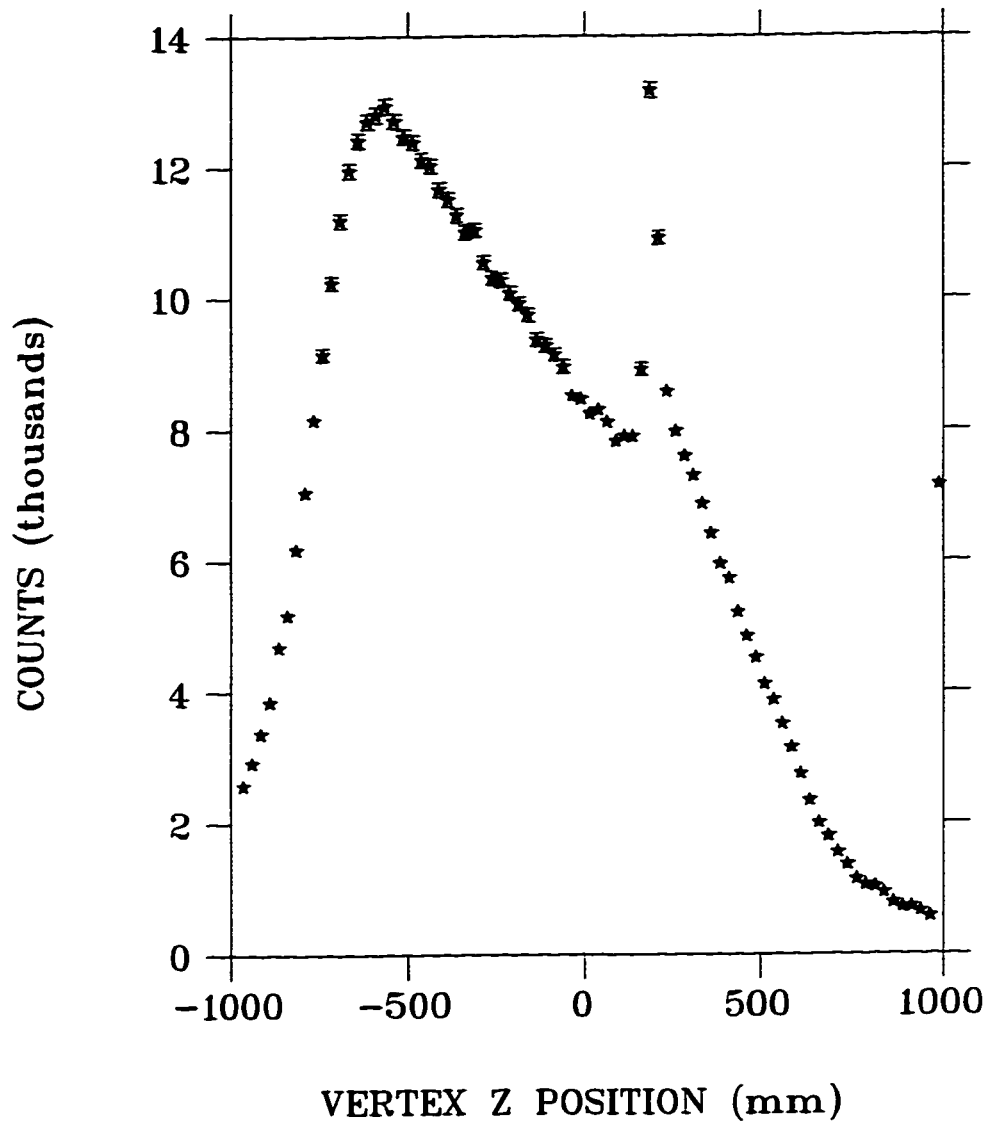


Figure 4.3: The z position of the vertex for events with track multiplicities ≥ 1 from a typical $D(\gamma, pp\pi^-)$ run.

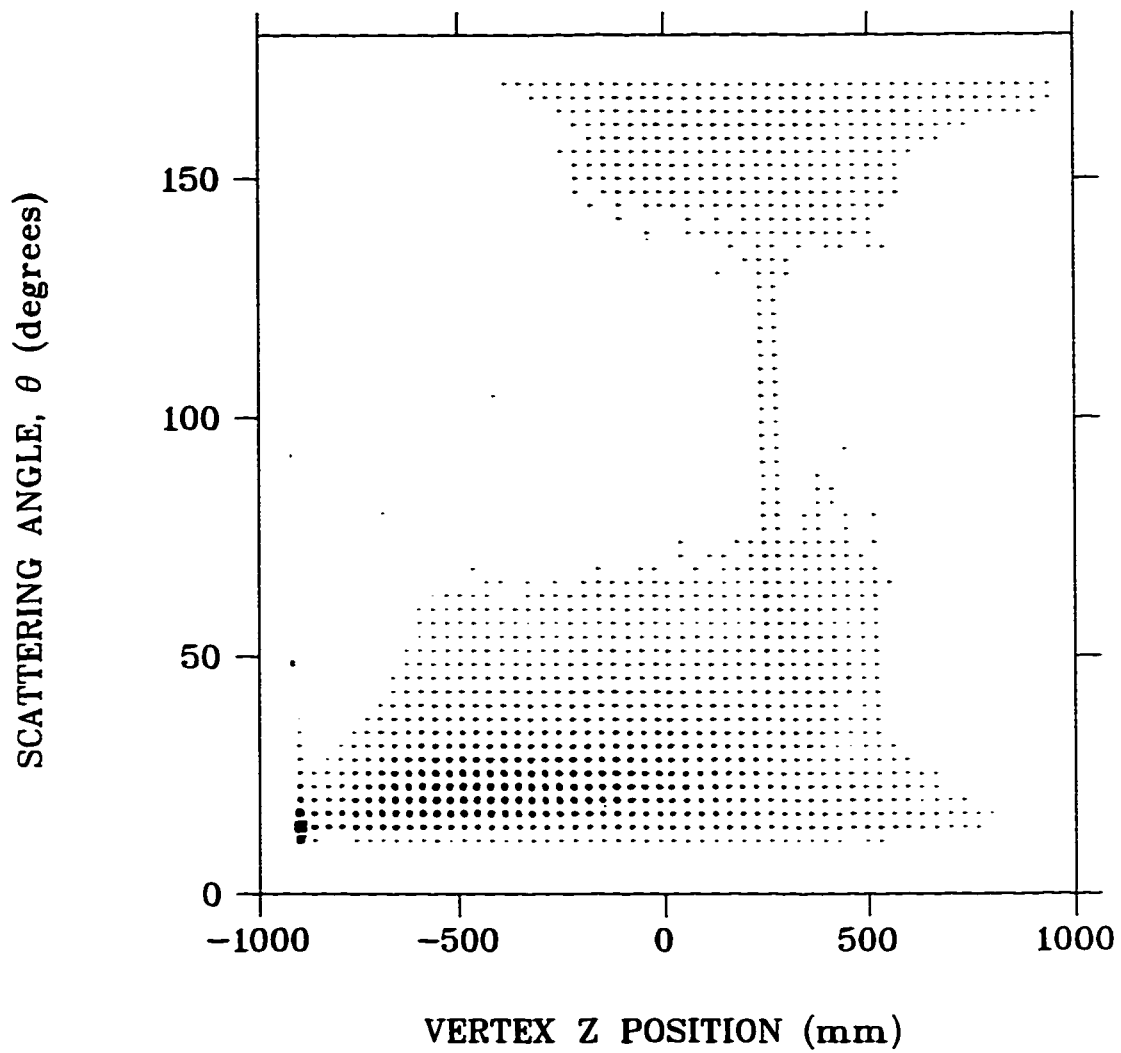


Figure 4.4: A θ versus z plot for events with track multiplicity ≥ 1 from a typical $D(\gamma, pp\pi^-)$ run.

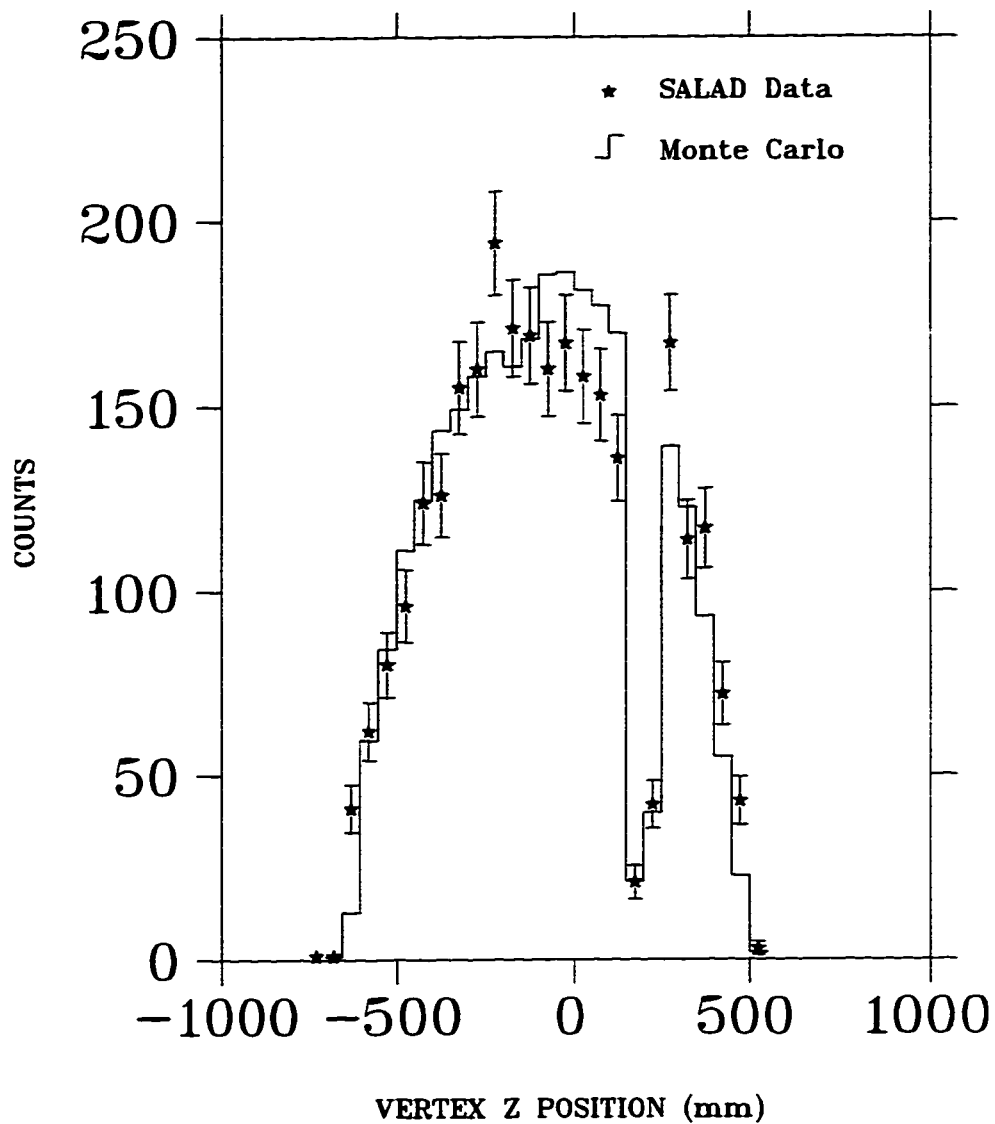


Figure 4.5: The z position of the vertex for three track $D(\gamma, pp\pi^-)$ events after the final cuts are applied. The solid histogram is a Monte Carlo simulation.

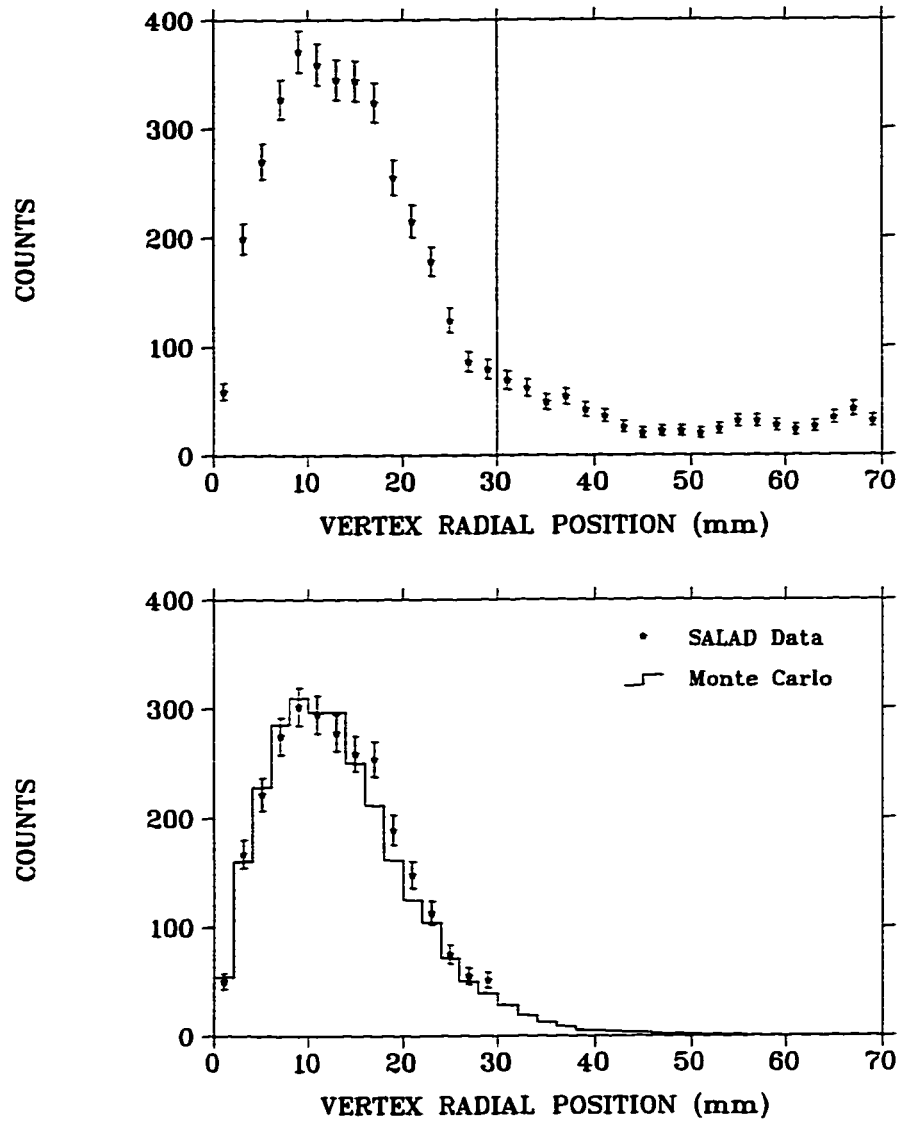


Figure 4.6: Radial position of the vertex for three track $D(\gamma, pp\pi^-)$ events. The top plot was obtained before the final cuts were applied. The bottom plot was obtained after the final cuts were applied. The solid histogram is a Monte Carlo simulation.

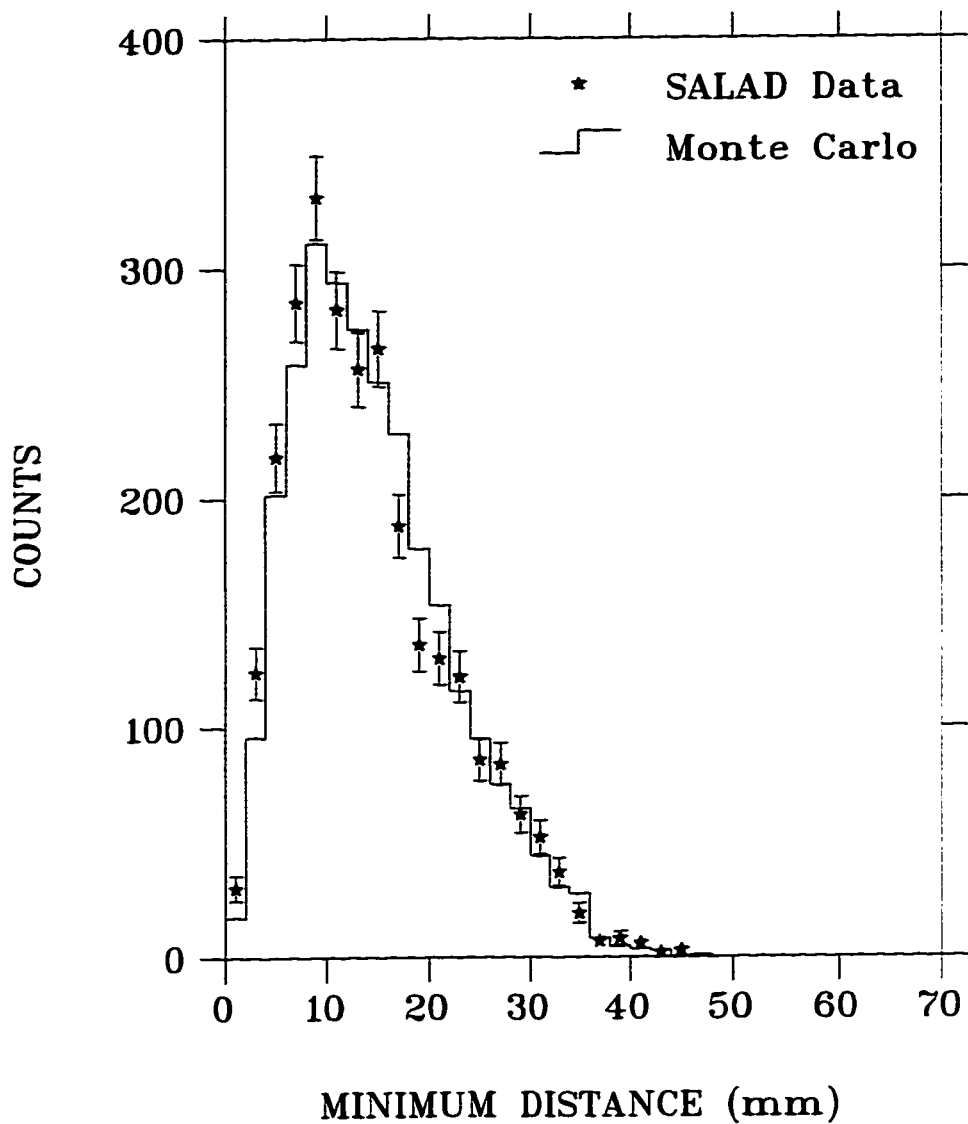


Figure 4.7: Average minimum distance between outgoing tracks for three track $D(\gamma, pp\pi^-)$ events after the final cuts are applied. The solid histogram is a Monte Carlo simulation.

and,

$$\gamma = \frac{1}{\sqrt{1 - \beta^2}}. \quad (4.9)$$

Figure 4.8 shows the mean energy loss obtained from the Bethe-Bloch formula as a function of kinetic energy. Protons and pions have distinct curves on such a plot, particularly in the low energy region. This may be exploited for particle identification purposes. Figure 4.9 is a $\Delta E/\Delta x$ versus E plot obtained from SALAD for three track events, where ΔE is the energy deposited, and Δx is the distance traversed in the ΔE scintillators. The lines of Figure 4.8 are smeared out due to the resolution of SALAD. However, two clusters may be identified. The first cluster, with the lowest ΔE and E values, is due to electrons and pions whereas the second cluster is due to protons. Cuts are usually applied to separate the different types of particles. In order to simplify the cuts, the two dimensional spectrum is projected on a one dimensional plot. The energy loss per unit length may be approximated by

$$\frac{dE}{dx} \simeq \frac{Dz^2A}{E^{\alpha-1}}, \quad (4.10)$$

where α and D are constants, and E is the kinetic energy of the incident particle. Integrating we get

$$\frac{(E + \Delta E)^\alpha - E^\alpha}{\alpha} \simeq Az^2D\Delta x. \quad (4.11)$$

Only z and A depend on the outgoing particle's type, and may therefore be used to identify the particle. We may then define

$$pid = z^2A \simeq \frac{(E + \Delta E)^\alpha - E^\alpha}{\alpha D \Delta x}. \quad (4.12)$$

The values of α and D are determined by optimizing the particle type separation on the one dimensional pid plot. Figure 4.10 shows the linearized stopping power histogram of

Figure 4.9. Two peaks (corresponding to the two clusters of Figure 4.9) may be clearly identified on this plot. The pions are buried under the electron peak, showing a small bump in the spectrum of Figure 4.10 at about $pid = 0.3$. The protons peak slightly above $pid = 1$.

A lower cut at 0.1 was applied on the pid spectrum as shown in Figure 4.10 to eliminate electrons that escaped the tracking cuts. This results in cutting 60% of the remaining events. Another cut at 2.0 was applied at the upper end of the pid spectrum to eliminate events with spurious pid , this results in cutting 0.5% of the events, as no major background results in particles with pid values in this region.

A fair amount of mixing between pions and protons is evident. This mixing results from the strong absorption of pions in the SALAD scintillators. As pions are negatively charged, the probability of them getting absorbed by a nucleus due to the Coulomb interaction is close to 100% as they slow down in the scintillators. As they approach the nucleus, they strongly interact with the nucleons, and a number of different types of particles may be emitted in this process. About 75% of the pion mass is available as kinetic energy for the outgoing particles, whereas the rest of the pion's mass is converted into binding energy. Table 4.2 shows the types of particles released from the process of π absorption on ^{12}C and the relative probability of their release [20, 34]. The strong interaction occurs in a time scale that is much shorter than that of the signal processing electronics (10^{-25} s compared to 10^{-8} s). If a pion stops in the E scintillator and is absorbed, the processed signal is a sum of the pion's kinetic energy and the energy deposited by the particles released in the process. The energy deposited in the E scintillator may thus be higher than expected, resulting in smearing out the pion cluster towards the proton cluster on a stopping power histogram. This smearing

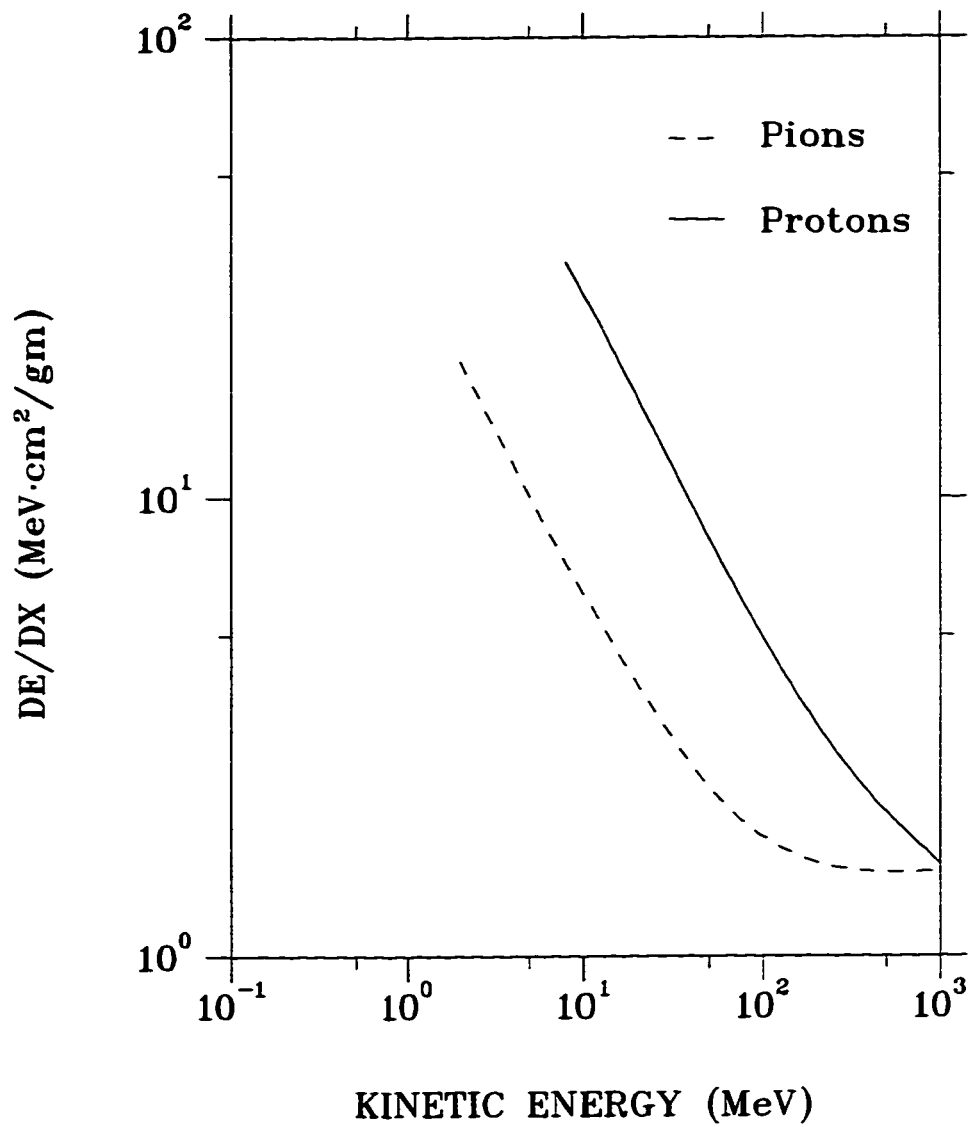


Figure 4.8: Stopping power as a function of energy for protons and pions as calculated from the Bethe-Bloch formula.

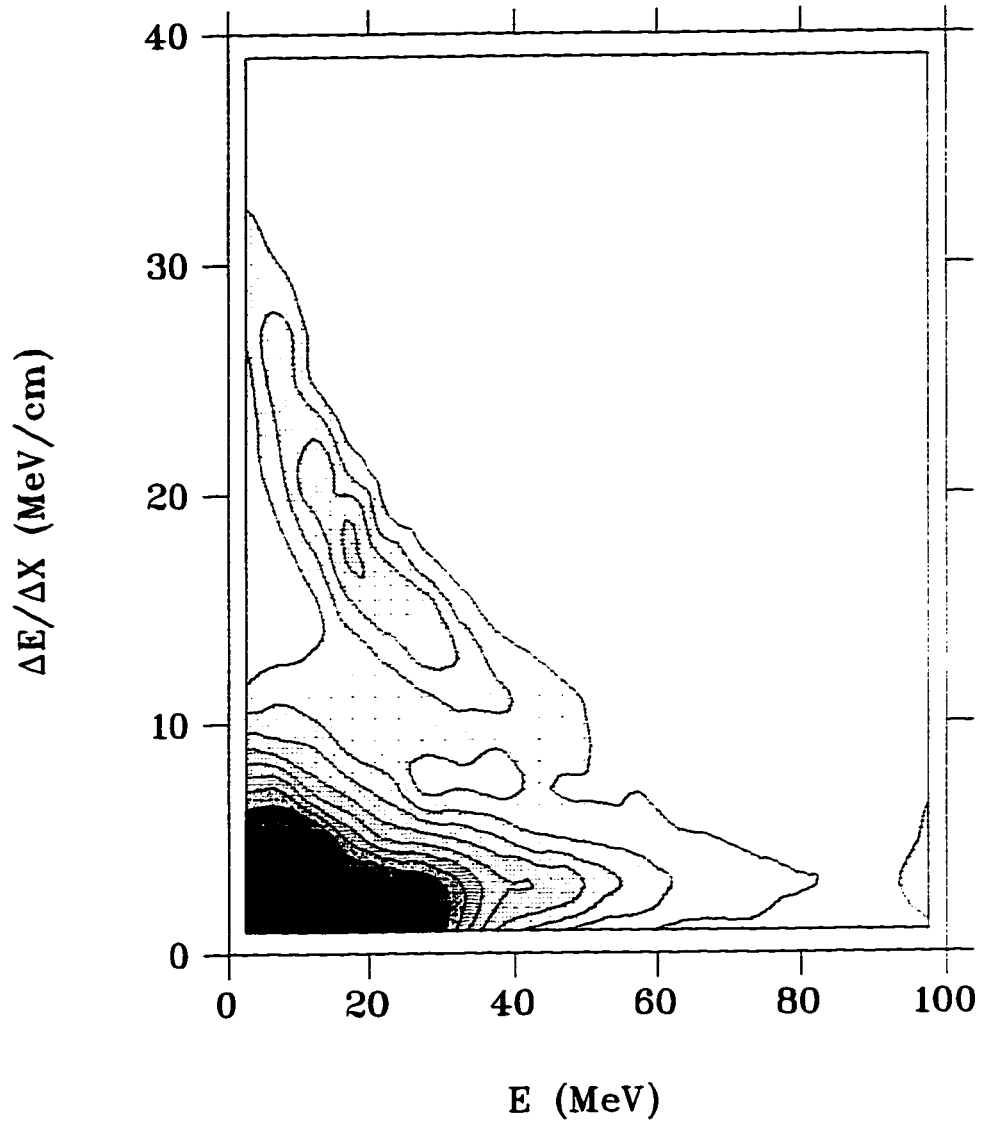


Figure 4.9: Stopping power versus energy for three track $D(\gamma, pp\pi^-)$ events before applying the cuts.

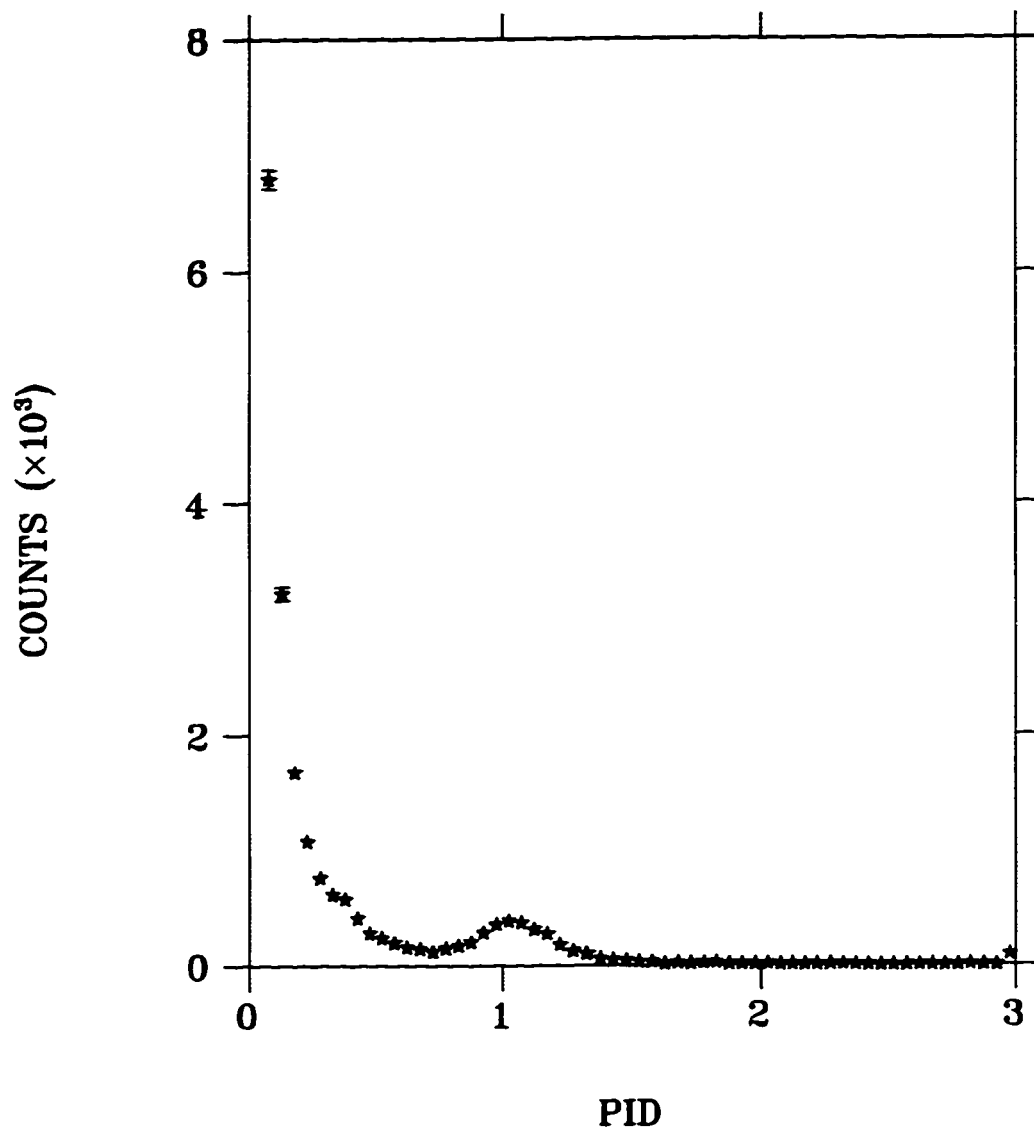


Figure 4.10: Linearized stopping power histogram for three track $D(\gamma, pp\pi^-)$ events before applying the cuts. The first peak corresponds to electrons, the small bump (at about 0.3) is due to pions, whereas the second peak is due to protons.

Particle type	Average multiplicity per π^- stop	Average released kinetic energy per π^- stop (MeV)
n	2.5	76.0
p	0.485	10.4
d	0.356	6.3
t	0.249	3.0
He	0.84	6.2
${}^9\text{Li}$	0.12	0.8
${}^7\text{Li}$	0.12	0.8

Table 4.2: Particles emitted as a result of the π^- absorption process on ${}^{12}\text{C}$ [20].

is also evident on the pid plot of Figure 4.11. While a Monte Carlo simulation (in this case, one that doesn't take pion absorption into account) predicts an almost symmetric distribution of pion pid as may be seen from the figure, the experimental pid spectrum is smeared out and highly asymmetric. It was determined that about 20% of the pions will have a pid value that corresponds to a proton as a result of this process. Many of the $D(\gamma, pp\pi^-)$ events will be interpreted as three proton events. In such a case, stopping power information is disregarded. Since the kinematics of these events are overdetermined, a permutation is made over the particles' type for these events, and the permutation that best satisfies the kinematics is chosen as the correct one. Where stopping power information is used, a particle with $pid < 0.6$ is considered to be a pion whereas a particle with $pid > 0.6$ is considered to be a proton. The Monte Carlo simulation was used in determining the correct particle identifications. Figure 4.12

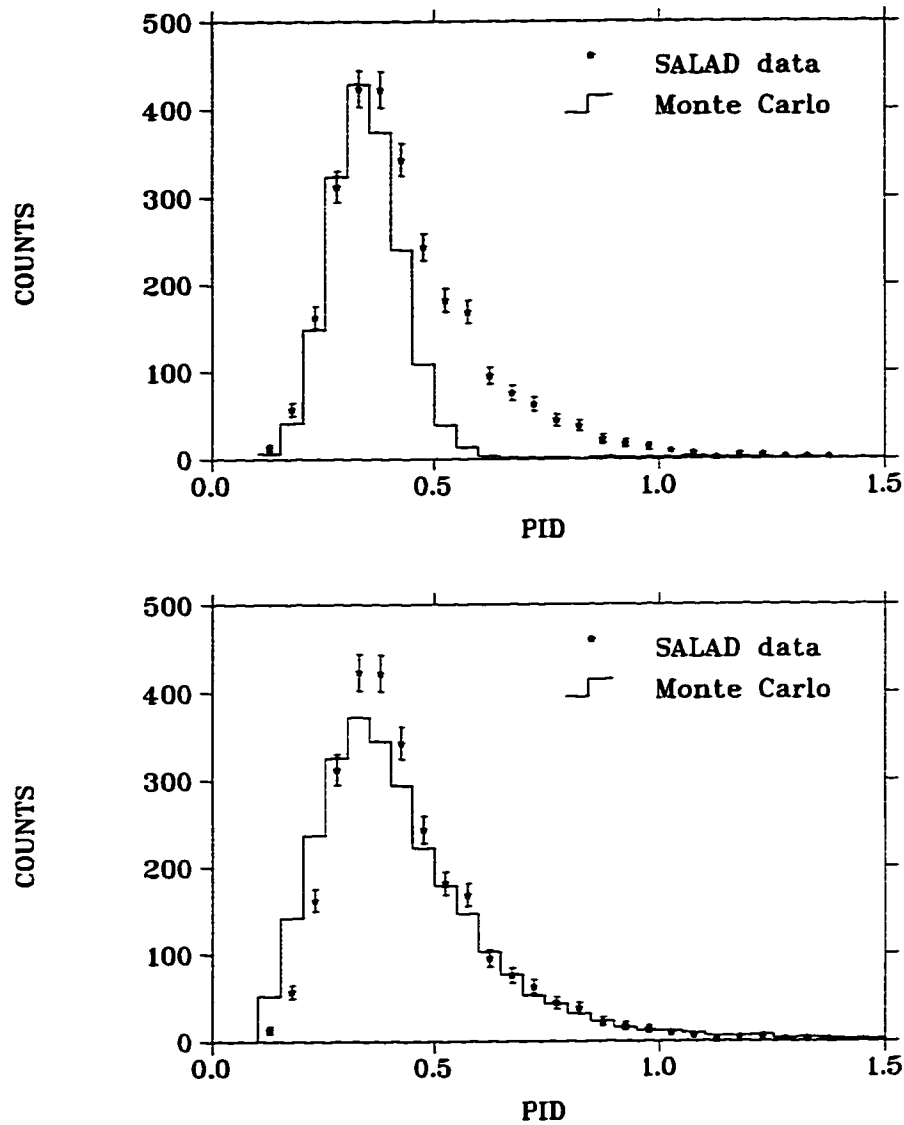


Figure 4.11: Pion's linearized stopping power histogram for three track $D(\gamma, pp\pi^-)$ events after applying the cuts. The top plot compares the data to a Monte Carlo simulation that does not take π^- absorption into account. The bottom plot compares the same data to a Monte Carlo simulation that accounts for π^- absorption.

shows a stopping power and a *pid* histogram after the final cuts were applied, where pions and protons are identified as discussed above.

4.1.3 Event Selection

The combined effect of low particle energies and relatively high detector thresholds results in drastically reducing the number of detected $D(\gamma, pp\pi^-)$ events. The highest photon energy was 290 MeV. Since a pion is formed, 140 MeV are lost, and the remaining 150 MeV are distributed as kinetic energy among the three outgoing particles. In this energy region, the quasi-free process is dominant and one of the protons is a spectator which does not share this energy. This proton will likely lose its energy in the walls of the detector and not make it all the way to the ΔE scintillators.

Due to the low photon energies, two decisions were made. At the hardware level, the usual trigger requirement that a tagger signal be present was dropped when three SALAD telescope signals were present, as discussed in section 2.4.1. At the software level, only three track events were analyzed in order to reduce the background. Furthermore, due to possible pion absorption in the scintillators, the measured pion energy was not used.

The events were then classified into five categories according to the number of measured kinematic quantities for each event. By examining the various distributions resulting from the analysis of each category, it was determined whether that category contains a large number of $D(\gamma, pp\pi^-)$ events or contains mostly background.

Table 4.3 shows the different types of events considered in the analysis. The category with the highest number of measured quantities (three tracks with three ΔE and three E signals) was first analyzed and used as a bench-mark for events with fewer measured

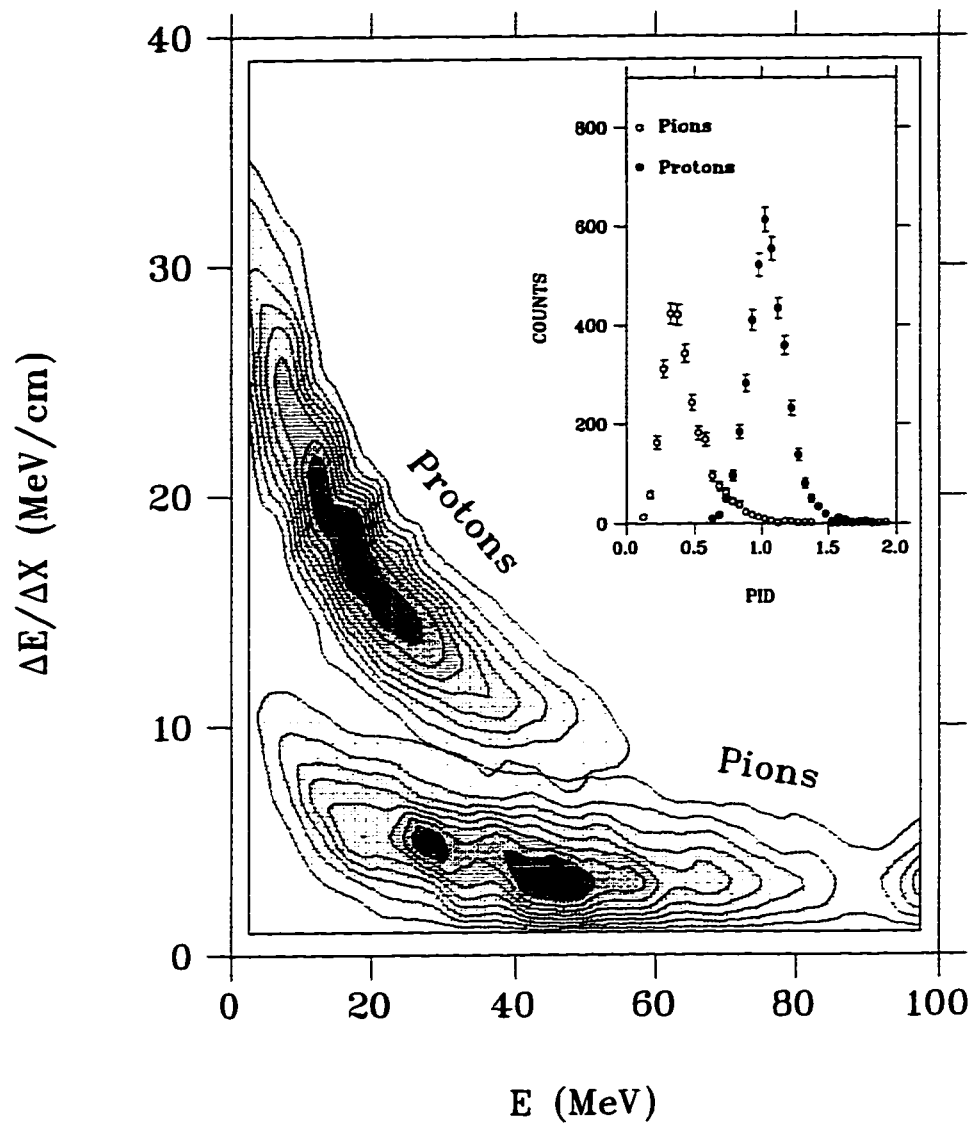


Figure 4.12: Stopping power versus energy for three track $D(\gamma, pp\pi^-)$ events after the final cuts were applied. The figure in the top right corner is a linearized stopping power histogram.

Number of E signals	Types of Particles resulting in E signals	Fraction of total events	$\langle\chi^2\rangle$
3	proton, proton, pion	32%	1.5
2	proton, pion	34%	1.5
2	proton, proton	6%	4.1
1	pion	12%	2.6
1	proton	16%	3.1

Table 4.3: Types of $D(\gamma, pp\pi^-)$ events analyzed, and the results of the analysis. All events have three tracks and three ΔE signals. The average χ^2 is computed from values between zero and 10.

quantities. The second type of events are those with three ΔE and two E signals. These events were further classified into two categories: events with one E signal due to a proton and the other due to a pion, and events with both E signals due to a proton. The first category was found to consist of mostly good events, whereas the other was found to be mostly background, as a result of the dominance of the quasi free process. The third type of events have three ΔE and one E signals. This group was also classified into two categories: events where the E signal is due to a pion or a proton. Both of these categories were found to be mostly background.

Several distributions were used to characterize the background. The θ , z_{vtx} , r_{vtx} , and $mindis$ distributions all provide means to characterize the background (see section 4.1.1), as well as the kinematic information available. Only three track events with three ΔE and three E signals, and three track events with three ΔE and two E proton-pion signals were used in the final analysis.

Both an analytic solution and a fitting program were used to analyze all categories. For all types of events discussed above, eight measured kinematic variables are available: six angles and two energies (the pion energy is not used as it is obscured due to a possible pion absorption). The photon and pion energies are to be determined. For the analytic solution, four angles and two energies were used to determine the unknown photon and pion energies. Since the tracks are unidentified, a permutation over the particle's type was required, and the remaining angles were used to select the correct permutation.

A fit has two advantages over an analytic solution. First, a χ^2 distribution may be used to characterize and eliminate the background, and second, a fit allows a more accurate determination of the unknown kinematics as well as the measured variables. For example, the difference between the measured θ angle and the one determined from the kinematic fit results in a distribution with a FWHM of 1.2° , whereas the FWHM from the analytic solution is 18° .

For the fitting program, the unknown variables may be eliminated from the kinematic equations, thus resulting in two equations. The inputs to the fitting program are then: all the measured variables (3 θ and 3 ϕ angles, 3 ΔE energies, and 1 or 2 E proton energies as available), two constraints (the reduced kinematic equations), and the resolutions (in θ , ϕ , ΔE , and E all of which were presented in the second chapter). The constraints of the fit are minimized by varying the measured variables within their respective weights. Once the measured variables are constrained, the unknown kinematic variables may be determined.

A χ^2 distribution was defined by

$$\chi^2 = \frac{1}{N} \sum_i \left(\frac{v_i^m - v_i^f}{\sigma_i} \right)^2, \quad (4.13)$$

where v_i^m is the i^{th} measured variable, v_i^f is the i^{th} variable determined from the fit. σ_i

Cut Applied	Remaining Events
r_{utz}	84%
χ^2	77%

Table 4.4: Final cuts imposed on the remaining $D(\gamma, pp\pi^-)$ events and the percentage of events remaining after each successive cut is applied.

is the detector's resolution for that variable, and N is the number of variables in the fit. Whenever a particle type ambiguity exists (see section 4.1.2), the process is repeated for the three possible track permutations, and the one with the lowest χ^2 value is chosen as the correct one. Figure 4.13 shows a schematic summary of the analysis. Figure 4.14 shows the χ^2 distribution for the different types of events rejected due to the relatively large background. Figure 4.15 shows the χ^2 for events considered in the analysis.

To reduce the remaining background, a cut was imposed on the χ^2 distribution, as shown in Figure 4.15. Only events with $\chi^2 < 3$ were considered as good $D(\gamma, pp\pi^-)$ candidate events. Table 4.4 shows a summary of the final cuts imposed in this analysis and the percentage of events remaining after each cut is applied.

4.2 Monte Carlo Simulations

The SALAD Monte Carlo generates events according to the phase space distribution, using the actual spatial distribution of the photon beam. For untagged events, the Monte Carlo uses a bremsstrahlung beam energy distribution [33, 40] calculated at the proper electron energy as shown in Figure 4.16.

Since the angles and energy of the outgoing particles are known, each particle may be tracked forward through the various layers of the detector, and the energy deposited

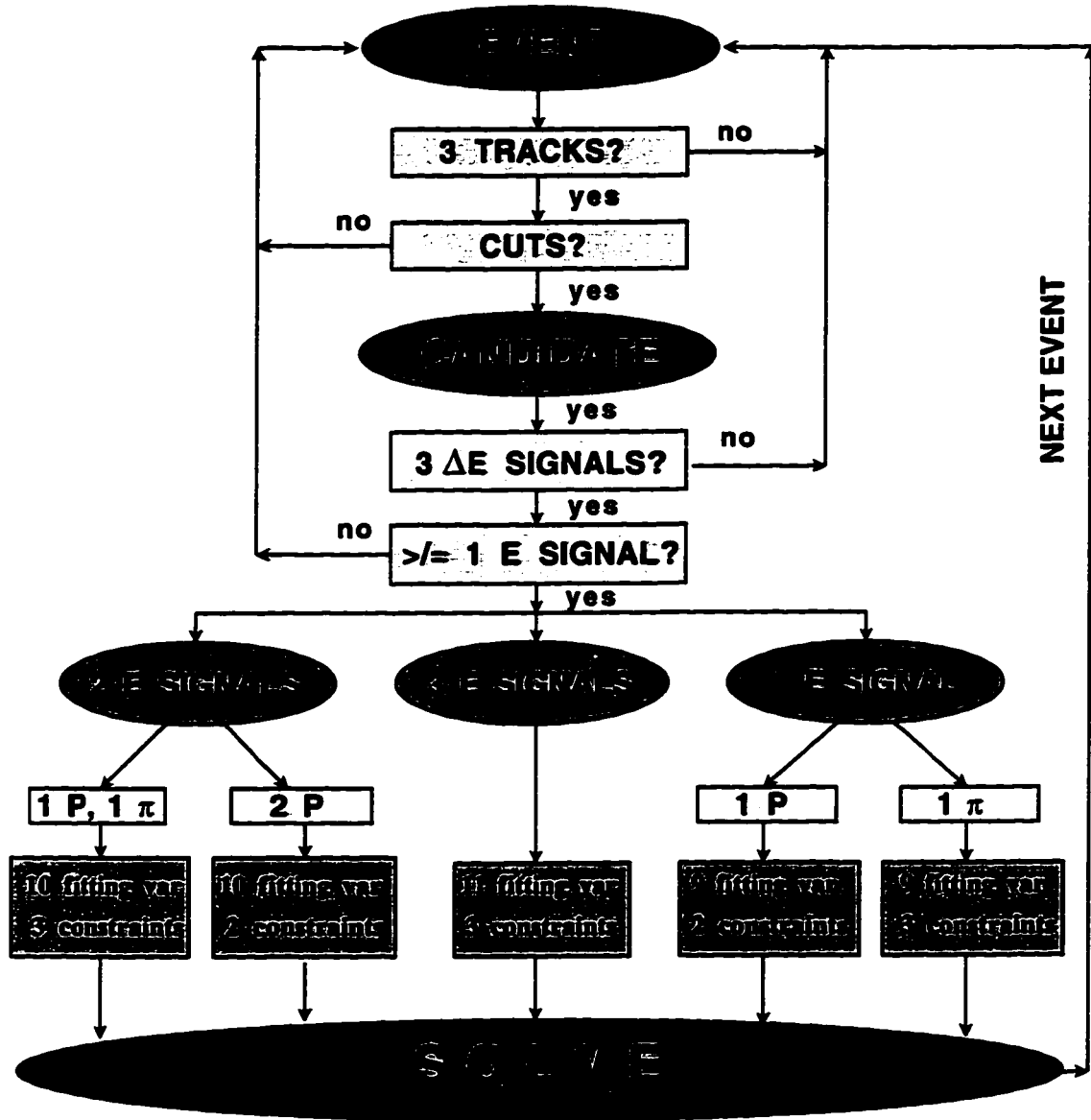


Figure 4.13: A schematic summary of the analysis showing the different types of $D(\gamma, pp\pi^-)$ events analyzed.

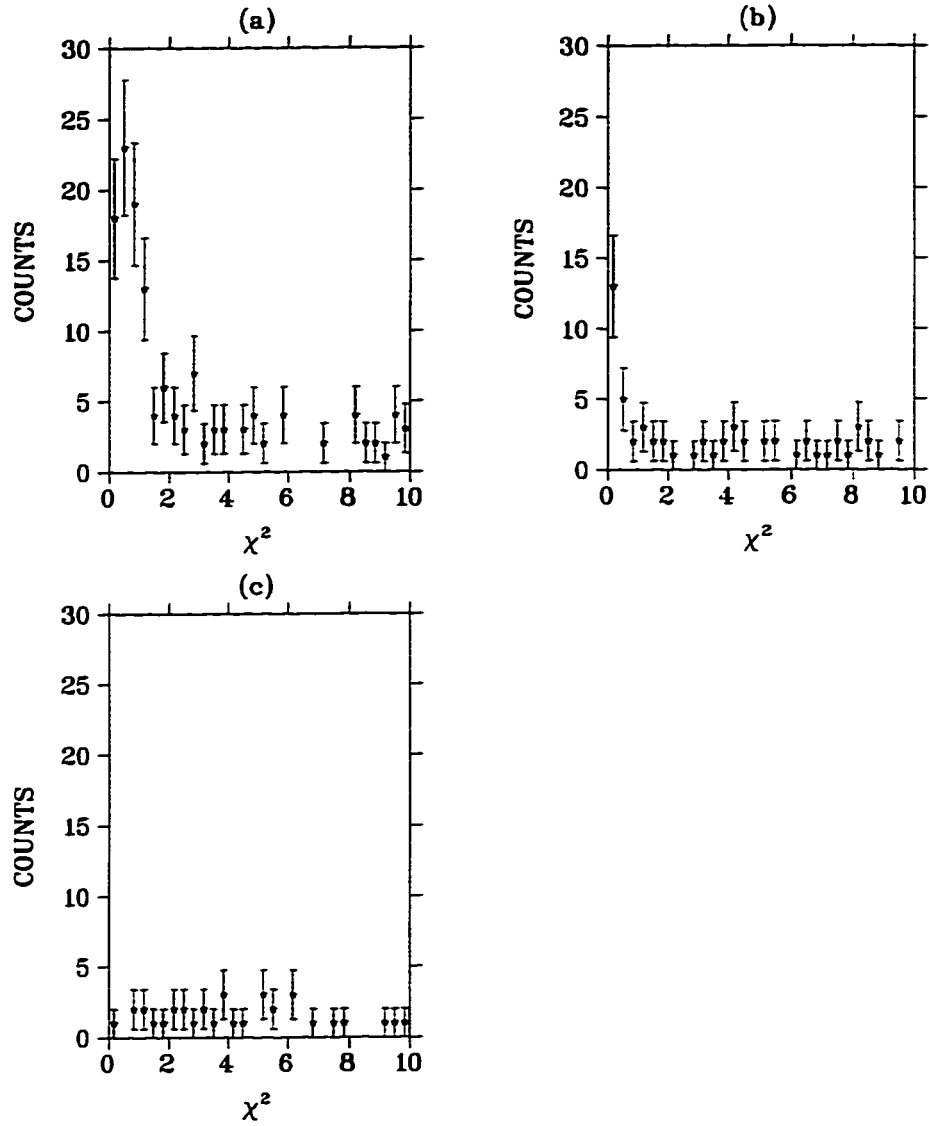


Figure 4.14: χ^2 distributions for $D(\gamma, pp\pi^-)$ candidates with three tracks and three ΔE signals which were not used in this analysis. Figure (a) is for events with one E pion signal. Figure (b) is for events with one E proton signal, and Figure (c) is for events with two E proton signals.

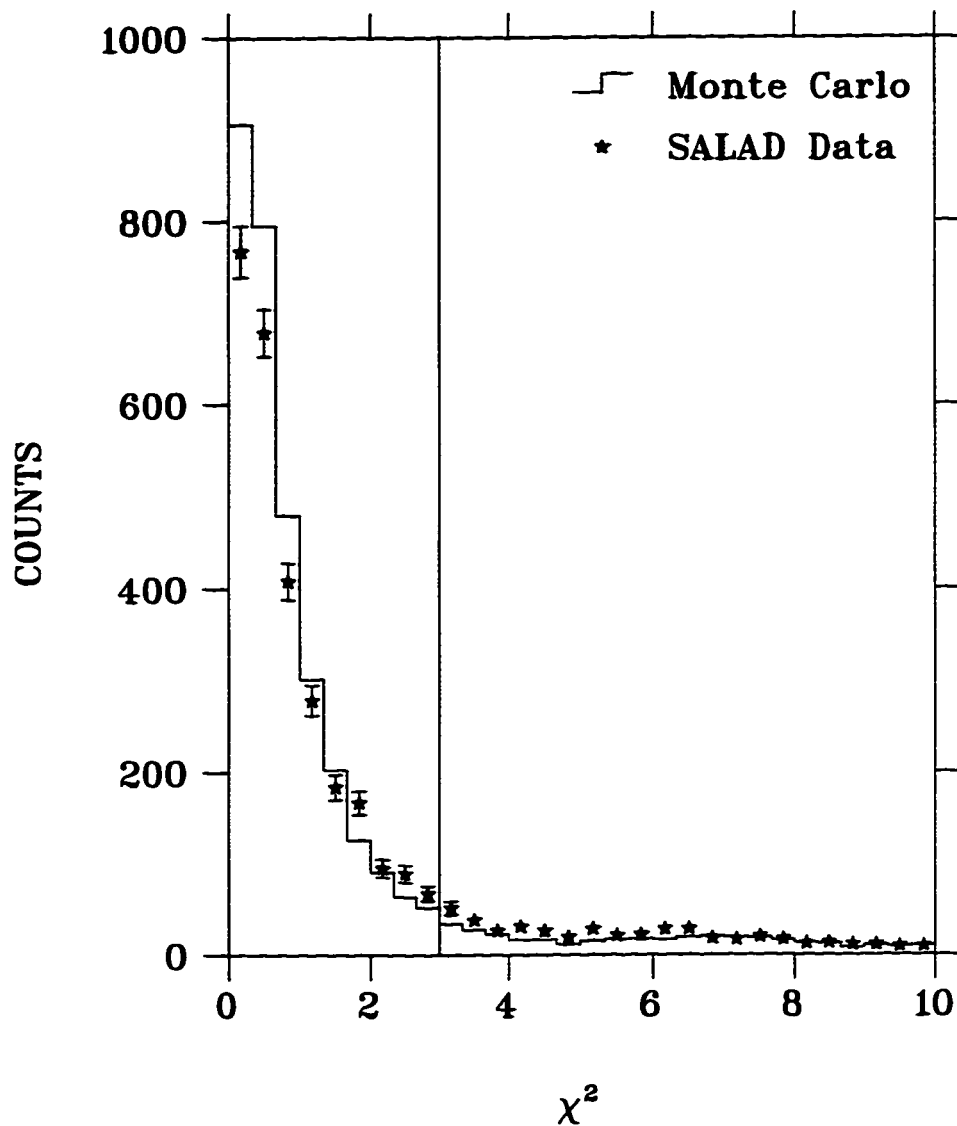


Figure 4.15: χ^2 distributions for $D(\gamma, pp\pi^-)$ candidates considered in the remaining part of the analysis. These events include three track events with three ΔE signals, and either three E or two E proton-pion signals. A cut is imposed at $\chi^2 = 3$ to eliminate the remaining background. The solid histogram is a Monte Carlo simulation.

in each layer may be calculated. As each particle is tracked in the wire chambers, the wire chamber cells intersected by the track are determined, as well as the z position of the hit on the wire. This z position is smeared out to take into account the wire chamber resolutions discussed in section 2.3.1.4. The total charge deposited in a wire chamber cell Q_{sum} is chosen according to a Gaussian distribution designed to characterize the data distribution. Knowing the z position of the hit on a wire, the difference between the charge deposited at the upstream and downstream ends of the wire may be determined by solving equation 2.5 for ΔQ , where ΔQ is given by equation 2.4. The upstream and downstream ADC values, A_u and A_d , may then be calculated, and are given by

$$A_u = \frac{Q_{sum} + Q_{sum} \times \Delta Q}{2} \quad (4.14)$$

and

$$A_d = \frac{Q_{sum} - Q_{sum} \times \Delta Q}{2} \quad (4.15)$$

The wire chamber efficiency was determined from $^{12}C(\gamma, pp)$ events. When three hits that define a track are present in three chambers, the cell in the fourth chamber intersected by the track is investigated. The fraction of the events where that cell has an ADC hit is defined as its efficiency. This process is repeated for all the 216 cells in the four chambers. Figure 4.17 shows the wire chamber efficiencies for the four chambers. The resulting efficiencies are used in the Monte Carlo to define the probability distributions which determine whether struck cells should be assigned non-zero ADC values.

Once the ADC values of the wires are determined, the particle tracking proceeds to the calorimeter and the energy deposited in the ΔE and E scintillators is determined.

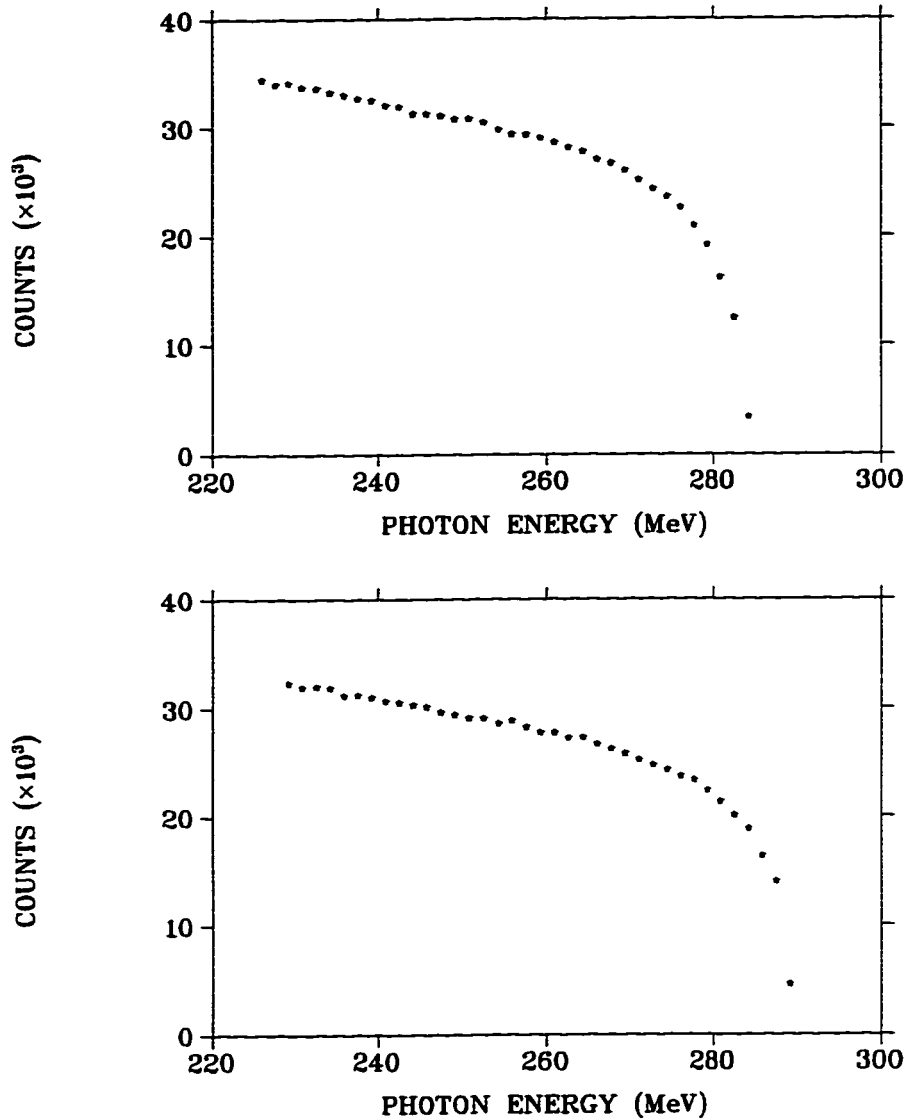


Figure 4.16: Photon energy distribution generated by the SALAD Monte Carlo to simulate a bremsstrahlung distribution. The bremsstrahlung cross section is obtained from Schiff [40], and calculated at an electron energy of 284 MeV for the top plot and 290 MeV for the bottom plot, corresponding to the two electron energies at which the experiment was conducted.

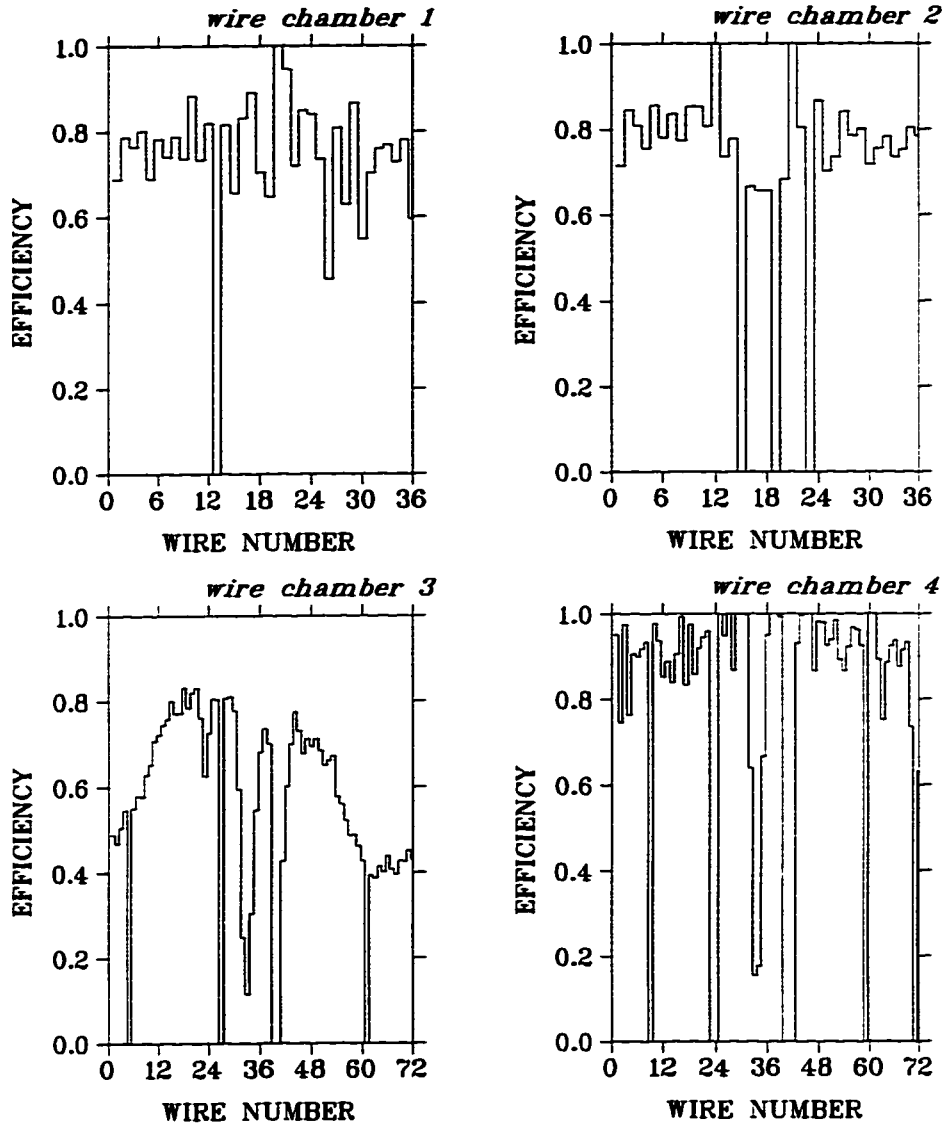


Figure 4.17: Efficiencies of the four SALAD wire chambers.

The total light output L_t may then be calculated by reversing the light correction process discussed in section 2.3.2.3. The light collected at either end of the scintillator, L_u and L_d , are give by

$$L_u = L_t e^{\frac{-|z|}{\lambda}} \quad (4.16)$$

and

$$L_d = L_t e^{\frac{-L-|z|}{\lambda}} \quad (4.17)$$

where z is the position of the hit in the scintillator (as determined by the wire chambers). L is the scintillator's length, and λ is the attenuation length of that scintillator. The attenuation lengths for each ΔE and E scintillator were calculated separately from overdetermined events obtained from other reactions. The resulting light outputs are smeared out to account for the ΔE and E energy resolutions discussed in section 2.3.2.4. Finally, the ADC_u and ADC_d values are calculated, and are given by

$$ADC_u = L_u \times gain. \quad (4.18)$$

and

$$ADC_d = L_d \times gain. \quad (4.19)$$

Several other corrections are included in the Monte Carlo simulation. Protons traversing the calorimeter may interact strongly with the scintillating material. The GEANT Monte Carlo simulation package GHEISHA was used to simulate the process and determine the observed energy when such an interaction occurs. Figure 4.18 shows the result of this simulation process for protons generated from the $D(\gamma, pp\pi^-)$ SALAD Monte Carlo simulation. The number of protons that deposit a different amount of energy than expected due to nuclear interactions is less than 0.5%. Nonetheless, this effect was included in the Monte Carlo.

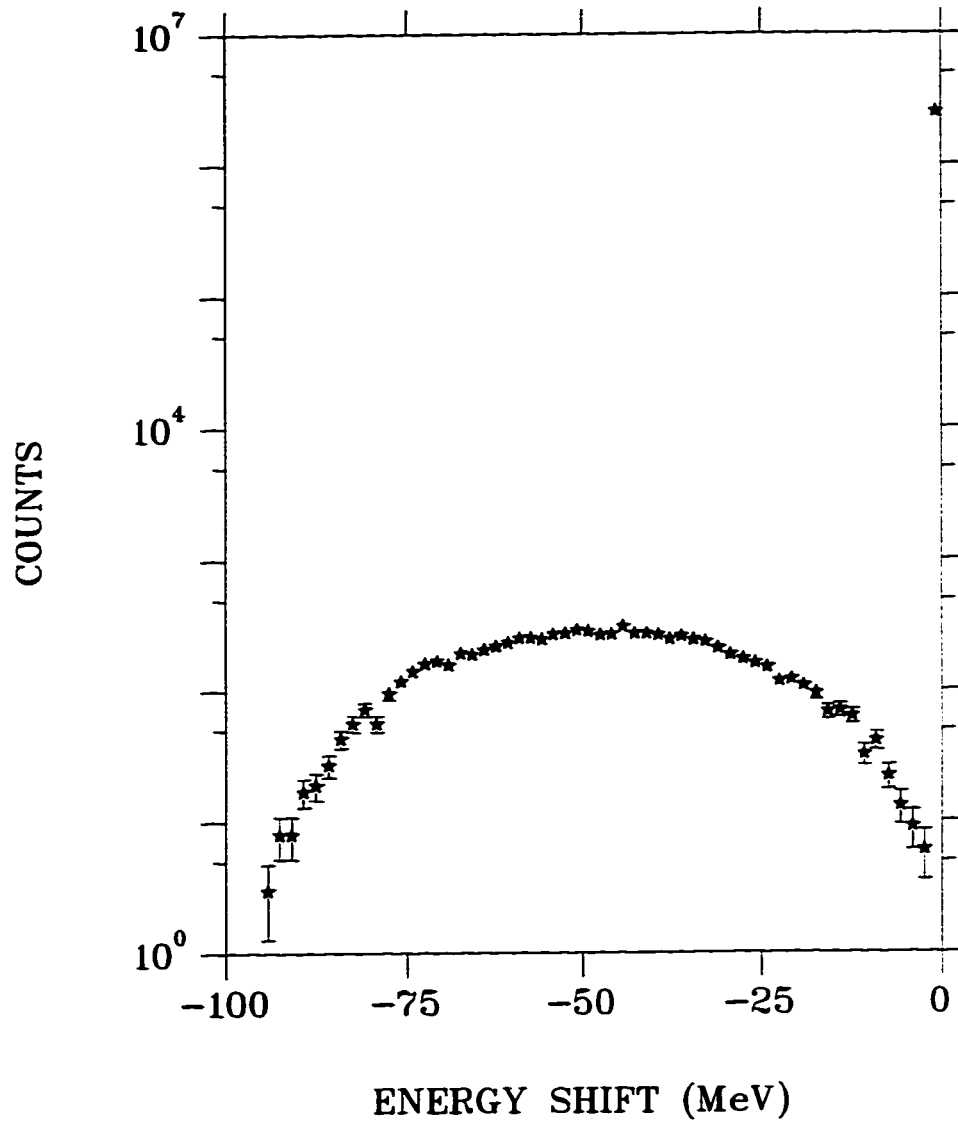


Figure 4.18: Shift in proton energy due to strong interactions in plastic scintillators. The distribution is obtained from the GEANT simulation package GHEISHA. A log scale was used to show the tail of the distribution. The number of protons that deposit a different amount of energy than expected due to nuclear interactions is 0.37%.

Two other complications arise due to pion detection: pion absorption and pion decay. As discussed in section 4.1.2, negative pions are absorbed by nuclei in the scintillator resulting in a strong interaction that in turn results in the release of several different particles. As shown in Table 4.2, neutrons are the most probable particles to be released. Plastic scintillators are highly inefficient in the detection of neutrons, and their response is highly nonlinear. A detailed simulation of this process is difficult to achieve. To account for this process, the shift in the pion energy is determined from the data. As discussed in section 4.1.3, the pion's energy is calculated from the fit. The energy deposited in the E scintillator is calculated by tracking the particle forward in the detector. This energy may be compared to the actual energy deposited in the E scintillator, and the shift ($E_m - E_f$) may be determined. The result is shown in Figure 4.19. This distribution is used as an input to the Monte Carlo, and pion energies are shifted according to this probability distribution.

A full account of the pion decay process is also included in the Monte Carlo simulation. Pions have a mean life $\tau = 2.60 \times 10^{-8}$ s seconds and decay via the process

$$\pi^- \rightarrow \mu^- + \bar{\nu}_\mu. \quad (4.20)$$

Pion decay times are selected according to the probability distribution

$$P(t) \propto e^{-t/\tau} \quad (4.21)$$

where t is the pion lifetime. Figure 4.20 shows the output distribution obtained from the Monte Carlo simulation. Once the lifetime is known, the distance from the vertex to the pion's decay point may be determined. If the decay occurs inside the target or the wire chambers, the muon's emission angle and energy are selected consistent with the kinematics of the decay process, and the muon is tracked instead of the pion. The wire

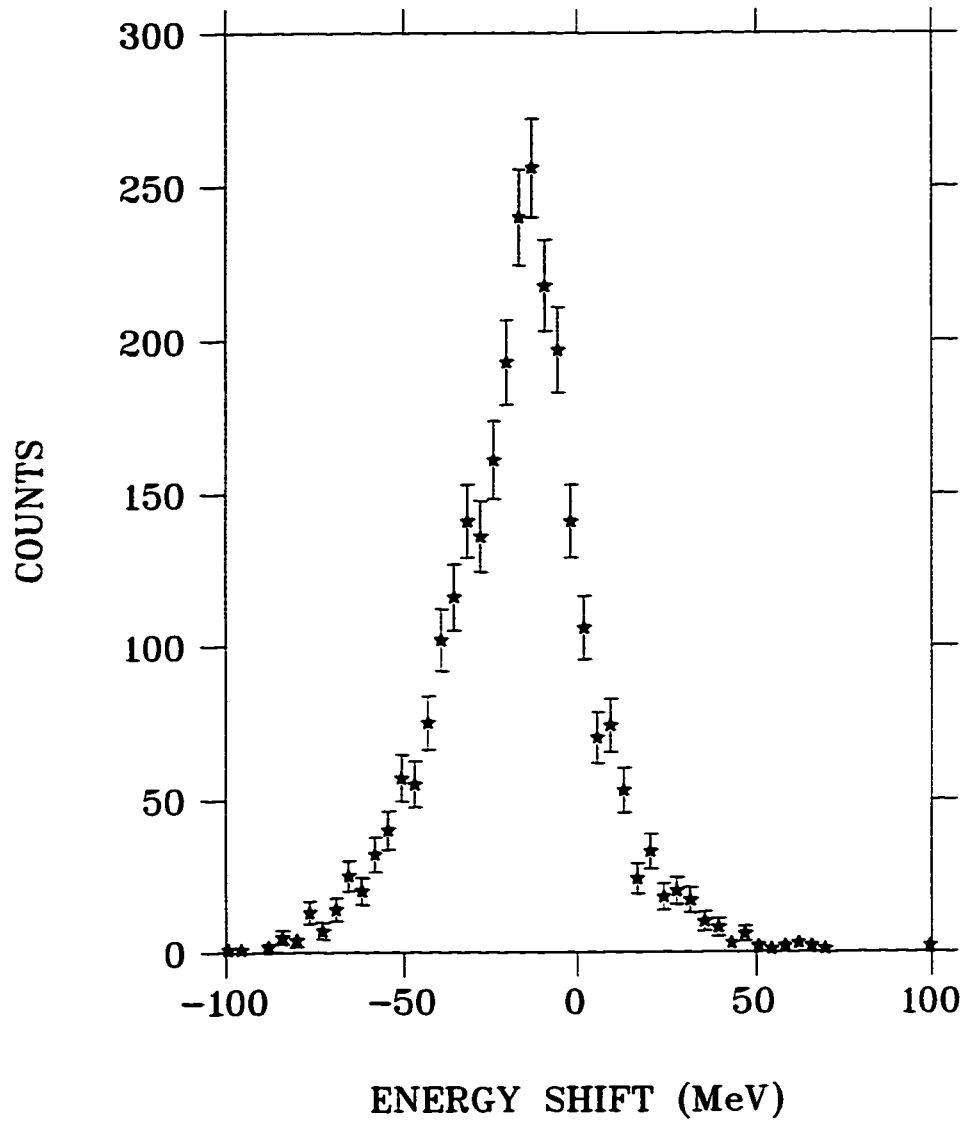


Figure 4.19: Shift in pion energy as a result of absorption in the SALAD scintillators.

chamber hits are then modified to account for the muon track and the resulting hits are used to attempt reconstructing a track assuming it is due to a single particle. Since this is not the case, a track is unlikely to be successfully reconstructed, and the event falls in the two track category and is thus disregarded. If a track is successfully reconstructed, the resulting θ and ϕ angles are likely to be off the values expected from the $D(\gamma, pp\pi^-)$ kinematics, and will fall in the tail of the χ^2 distribution, therefore not escaping the χ^2 cut. By simulating Monte Carlo events with and without pion decay, it was determined that 6% of the events are lost due to this process. It is worth mentioning at this point that since the pion's energy is not used, muons that decay outside the wire chambers need not be tracked.

The simulated events are then tested to determine whether they satisfy the experimental trigger. Both a ΔE threshold and a sum threshold are imposed as in the actual experimental trigger. These thresholds were determined for each ΔE and E scintillator separately from the raw ADC spectra and used as input to the Monte Carlo. Monte Carlo events that do not satisfy the threshold or do not fall within the detector's acceptance have their ADC values set to zero. Events that satisfy this threshold are written to disk. The Monte Carlo events are then read by the same analysis code used to analyze the actual experimental data. The same calibration parameters (energy loss tables, light correction tables, etc....) are used in the Monte Carlo as in the data analysis. This ensures that any deviation of the data from the Monte Carlo is due to dynamical physical effects.

The Monte Carlo allows for a large number of variables to be compared to the data. Figures ??, 4.6, and 4.7 show the good agreement in the tracking variables r_{viz} , $mindis$, and z_{viz} between the data and the Monte Carlo. Figure 4.11 shows the Monte Carlo pid

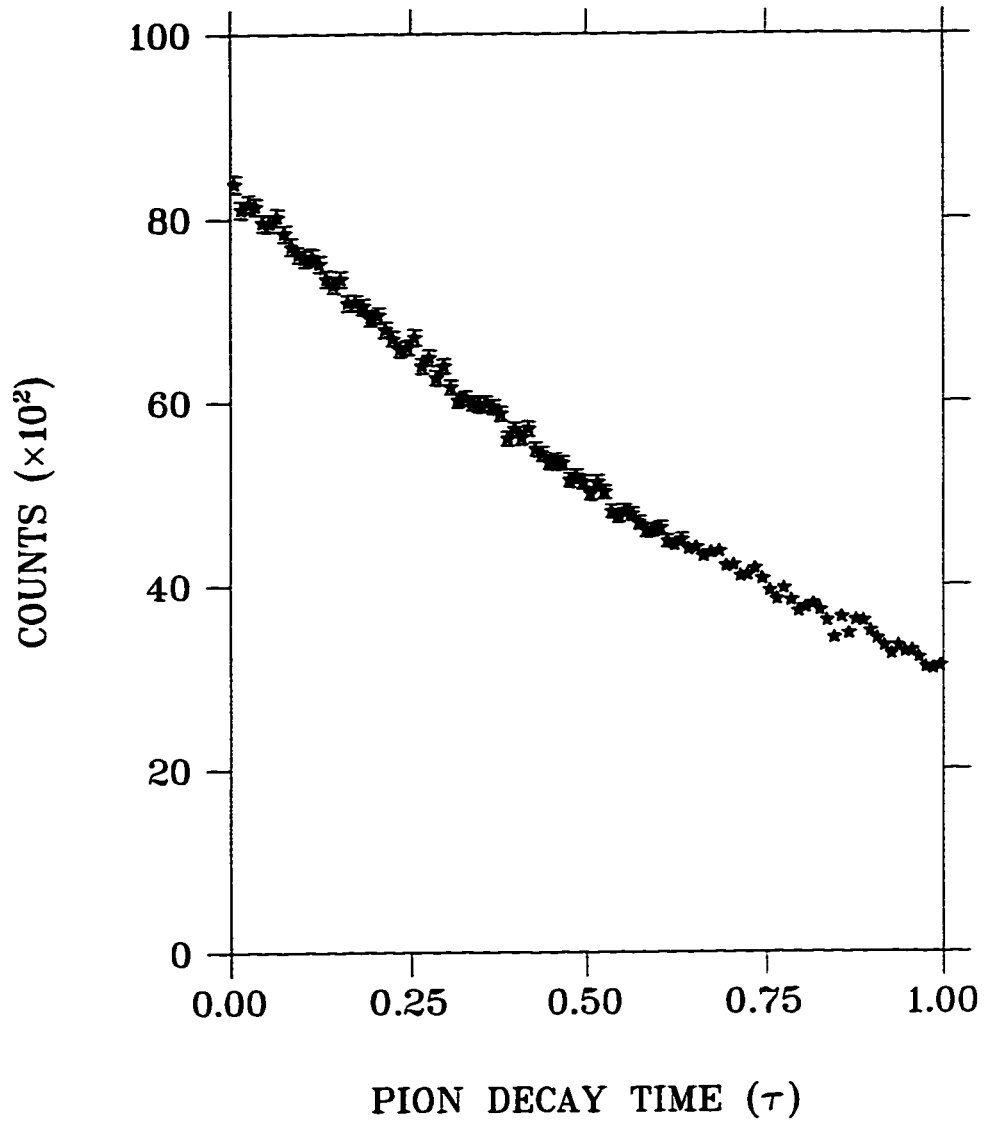


Figure 4.20: Pion lifetime distribution in units of the pion mean life $\tau (= 2.60 \times 10^{-8} \text{ s})$.

histogram with and without pion absorption, and Figure 4.15 shows the χ^2 distribution. The agreement with the data is quite good for all distributions. A slight disagreement may be seen in the χ^2 distribution. This is a result of the ambiguity in the energy resolution of the ΔE scintillators. The data used to determine the ΔE scintillators resolution are sparse, particularly for low values of ΔE , as may be seen in Figure 2.13.

Chapter 5

Results

Once the $D(\gamma, pp\pi^-)$ events are identified, one may proceed to calculate a cross section. The details of this calculation are presented in this chapter, as well as a detailed comparison to the theoretical calculation of J.M. Laget.

5.1 Calculation of the $D(\gamma, pp\pi^-)$ cross section

In the region of the Δ resonance the $\gamma D \rightarrow pp\pi^-$ may occur in two steps. The deuteron first disintegrates into a proton and a Δ ; the Δ , being an unstable particle (width. $\Gamma = 115$ MeV), quickly decays into a proton and a pion,

$$\gamma D \rightarrow p\Delta^0 \rightarrow pp\pi^-. \quad (5.1)$$

For the two body disintegration, the three particles involved (photon, proton and Δ) lie in a single plane so as to conserve momentum. Similarly, the particles involved in the Δ decay process should lie in one plane. This results in two planes with the track defining the direction of the Δ being common to both, as shown in Figure 5.1. With no

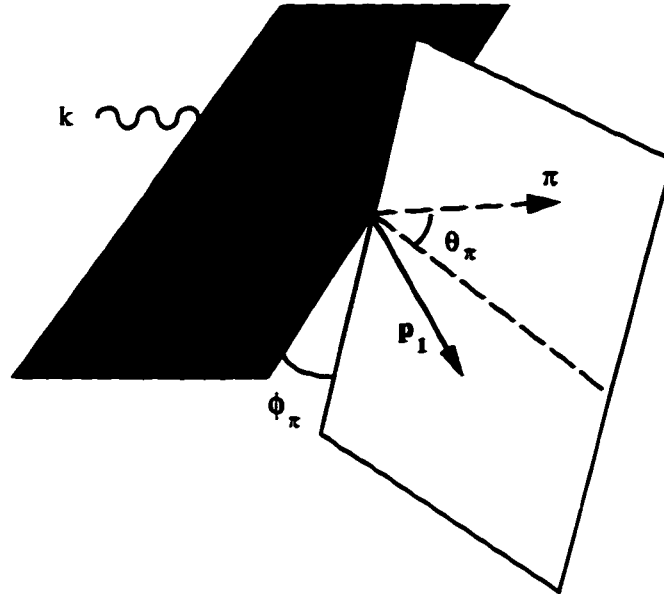


Figure 5.1: A schematic diagram of the $D(\gamma, pp\pi^-)$ reaction showing the intermediate process resulting in the creation of the $\Delta(1232)$ resonance and its subsequent decay. The definition of the kinematic variables used to calculate the cross section are also shown on the plot.

dynamical physical processes present, the two planes are randomly rotated with respect to each other, with the direction of the Δ defining the axis of rotation. In a coordinate system where the direction of the incoming photon defines the z axis, the angle between the two planes is the azimuthal angle of the pion, ϕ_π .

For three body final states, six variables (including the incident energy) are needed to uniquely identify the kinematics of the event. A differential cross section may thus be calculated in terms of six variables. However, one of these variables is a trivial overall azimuthal rotation and need not be considered, so the cross section may be described by a set of five variables. The five kinematic variables that best identify the process of interest should be used. In our experiment, the dynamics of the Δ are of particular

interest, so the variables chosen are those that best describe the reaction in terms of the intermediate $\Delta - N$ state. The photon energy E_γ , the $p - \pi$ invariant mass Q_Δ , the Δ scattering angle θ_Δ , and the pion scattering angles θ_π and ϕ_π were used. The Δ scattering angle is boosted to the γ -D centre of mass frame and labeled θ_Δ^{cm} . The pion's scattering angles are boosted to the Δ rest frame and labeled θ_π^- and ϕ_π^- . In terms of these five variables, the five-fold differential cross section may be written as,

$$\begin{aligned} & \frac{d^5\sigma}{dE_\gamma dQ_\Delta d\cos\theta_\Delta^{cm} d\cos\theta_\pi^- d\phi_\pi^-}(E_\gamma, Q_\Delta, \cos\theta_\Delta^{cm}, \cos\theta_\pi^-, \phi_\pi^-) \\ &= \frac{Y(E_\gamma, Q_\Delta, \cos\theta_\Delta^{cm}, \cos\theta_\pi^-, \phi_\pi^-)}{\Delta E_\gamma \Delta Q_\Delta \Delta \cos\theta_\Delta^{cm} \Delta \cos\theta_\pi^- \Delta \phi_\pi^-} \\ & \times \{N_\gamma(E_\gamma) \times N_t \times \varepsilon(E_\gamma, Q_\Delta, \cos\theta_\Delta^{cm}, \cos\theta_\pi^-, \phi_\pi^-)\}^{-1}. \end{aligned} \quad (5.2)$$

Defining a set of variables q_i as

$$\{q_i\} = \{E_\gamma, Q_\Delta, \theta_\Delta^{cm}, \theta_\pi^-, \phi_\pi^-\}, \quad (5.3)$$

the first factor on the right hand side of equation 5.2 may be written as $Y(\{q_i\})/\Pi_i \Delta q_i$. This factor is the experimental yield in a given bin divided by the bin width. $N_\gamma(E_\gamma)$ is the photon flux, N_t is the number of target nuclei per unit area, and $\varepsilon(\{q_i\})$ is the efficiency of the detector. The calculation of each one of these factors is described in detail below.

5.1.1 Experimental Yield

Calculation of the first factor in the above formula, $Y(\{q_i\})/\Pi_i \Delta q_i$, is straightforward. After reconstructing the $D(\gamma, pp\pi^-)$ events and applying the cuts described earlier, the events are binned in the five variables above. Table 5.1 lists the range of each variable and the bin width. This results in a five dimensional matrix labeled by the centre of each of the above bins.

Variable	Range	Bin width
E_γ	205 to 305 MeV	10 MeV
Q_Δ	1070 to 1190 MeV/c ²	12 MeV/c ²
$\cos\theta_\Delta^{cm}$	-1 to 1	0.2
$\cos\theta_\pi^*$	-1 to 1	0.2
ϕ_π^*	0° to 360°	36°

Table 5.1: List of variables used to calculate the $D(\gamma, pp\pi^-)$ cross section. The range for each variable was divided into 10 bins.

5.1.2 Photon Beam Flux

For tagged experiments the total number of photons in an energy bin $N_\gamma(E_\gamma)$ may be directly determined from the tagger counting rates, and is given by

$$N_\gamma(E_\gamma) = N_{tag}(E_\gamma) \times \eta_{tag}(E_\gamma), \quad (5.4)$$

where $N_{tag}(E_\gamma)$ is the number of electron counts in each of the tagger channels, and $\eta_{tag}(E_\gamma)$ is the tagging efficiency (see section 5.1.2).

Calculation of the photon flux for this experiment is complicated by the fact that the photons used had energies beyond the acceptance of the tagger. For tagged photons, the photon flux may be directly determined from the counting rates of the tagger. Although the bremsstrahlung energy distribution is well known, the actual number of photons remains to be determined. As previously mentioned, the tagger allows the tagging of photons up to an energy of 229 MeV. The photon flux up to an energy of 229 MeV may therefore be calculated as in a tagged experiment. Since the shape of the bremsstrahlung distribution is also known, it may be normalized to fit the tagger

E_γ MeV	210	220	230	240	250	260	270	280	290
N_γ	53.20	50.65	48.32	46.11	43.86	41.26	37.48	27.66	9.57

Table 5.2: Number of photons N_γ ($\times 10^9$) determined from the fits of the bremsstrahlung distribution.

counting rates in the tagged energy range. Due to a major beam tuning during this experiment, the first set of runs was conducted with an electron beam energy of 284 MeV and a tagging efficiency of 49%, whereas the second set was conducted with an electron beam energy of 290 MeV and a tagging efficiency of 56%. The photon energy was thus determined separately for each set. Figure 5.2 shows the result of these fits. Counts from the 62-channel tagger are binned in ten bins. The number of photons in each of the ten bins required for the calculation may be determined from the fit and are given in Table 5.2. The total number of photons in the incident beam in the range $205 \text{ MeV} \leq E_\gamma \leq 305 \text{ MeV}$ was determined to be 3.581×10^{11} photons.

5.1.3 Target Density

The target for this experiment was a deuterium gas cell 2.08 meters long with a 10.1 centimeter diameter (see section 2.2). Calculation of the number of target nuclei per unit area, N_t , is straightforward. Applying the ideal gas law, we have

$$N_t = \frac{Pl}{kT}, \quad (5.5)$$

where P , T , and l are the target's pressure, length and temperature, respectively, and k is the Boltzmann constant. Both the pressure and temperature of the target were monitored throughout the experiment. The areal density of target nuclei was calculated to be $7.79 \times 10^{22} \text{ Nuclei/cm}^2$. Variations in the target's pressure and temperature result

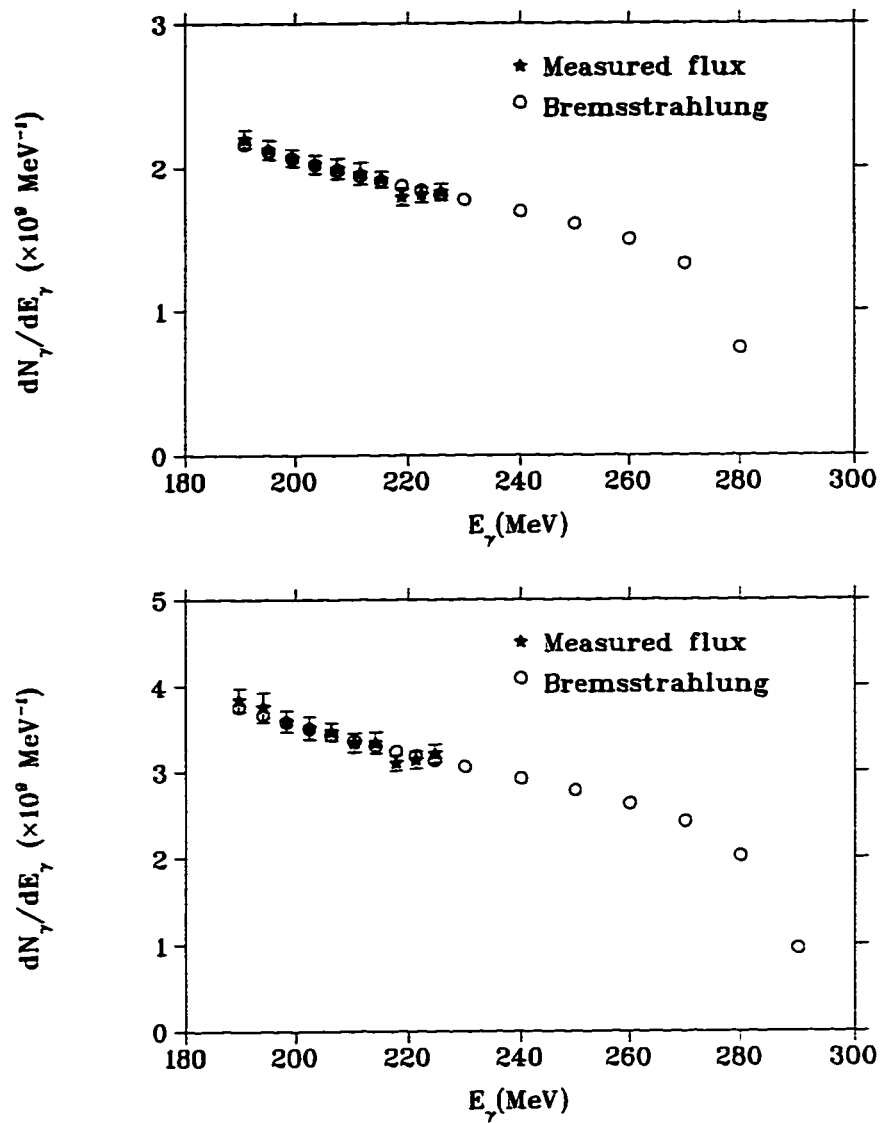


Figure 5.2: Bremsstrahlung photon energy distribution fitted to the tagger counting rates. The plots correspond to a maximum electron energy of 284 and 290 MeV for the top and the bottom plot, respectively.

in an error of less than 4%.

5.1.4 Detector Efficiency

Calculating the efficiency of the detector requires both calculating the detector's geometric acceptance and intrinsic efficiency. For a discrete detector, the geometric acceptance is easily determined and requires the calculation of the solid angle subtended by the detector. For SALAD however, the geometric acceptance is complicated due to the extended target and the requirement of coincidence detection.

The geometrical acceptance of the SALAD detector is dependent on the position of the target nuclei along the z axis, being maximum at the centre and dropping down towards either end. On the other hand, the geometrical acceptance is different for different events originating from the same position along the z axis due to the coincidence requirement, and depends on the direction and energies of the outgoing particles. The intrinsic efficiency of the detector is also strongly dependent on the kinematics of the event. The energy deposited in each layer of the detector is strongly dependent on both the particle energy and emission angle. Whether an event will cause three triggers requires the knowledge of the kinematics of all three outgoing particles so that the energy loss in the walls of SALAD may be calculated for each track separately to determine whether each particle will have enough energy to cause a trigger. One has, therefore, to determine whether the event generated will be detected for each event separately. An efficiency may be defined as

$$\varepsilon(E_\gamma, Q_\Delta, \cos\theta_\Delta^{cm}, \cos\theta_\pi^-, \phi_\pi^-) = \frac{N_{det}(E_\gamma, Q_\Delta, \cos\theta_\Delta^{cm}, \cos\theta_\pi^-, \phi_\pi^-)}{N_{gen}(E_\gamma, Q_\Delta, \cos\theta_\Delta^{cm}, \cos\theta_\pi^-, \phi_\pi^-)} \quad (5.6)$$

where $N_{gen}(\{q_i\})$ is the number of Monte Carlo generated events, and $N_{det}(\{q_i\})$ is the number of detected (and accepted) events.

It is worth mentioning at this point that in addition to the geometric acceptance and intrinsic efficiency of the detector, the factor $\varepsilon(\{q_i\})$ takes into account all the cuts applied in the analysis, including cuts aimed at eliminating the background. The efficiency factor thus accounts for any good events lost due to the cuts. The Monte Carlo, however, does not account for background events that may have survived the cuts. This contamination is estimated to be less than 1%, as may be seen in the good agreement between the data and the Monte Carlo simulation for the various distributions. In particular, the *mindis* distribution of Figure 4.7 has no cuts imposed on it, but no events are seen with a *mindis* value greater than 45 mm. Similarly the *pid* spectrum of Figure 4.12 shows no evidence of an electron contamination.

Calculation of the efficiency factor is quite cumbersome. The number of generated and detected events has to be large enough so that the statistical error in the determination of the efficiency factor does not impose a limit on the accuracy of the cross section. In this experiment, a three-fold coincidence was required. The highly selective nature of the analysis resulted in a very low efficiency, averaging around 4%. A large number of Monte Carlo events had to be generated and analysed. In addition, the efficiency has to be determined in terms of the five variables, binned the same way as the data (see section 5.1.1 and Table 5.1), requiring the calculation of the efficiency for 10^5 bins. A total of 45 million events were analyzed. While generating Monte Carlo events proceeded reasonably fast, due to the cpu-intensive fitting program it took an average of 0.28 cpu seconds to analyze each event on a vax 6000/90 resulting in a total of 3500 cpu hours for the complete calculation.

5.2 $D(\gamma, pp\pi^-)$ Cross Section

The five-fold differential cross section calculated in equation 5.2 was binned in 10 bins for each variable resulting in 10^5 bins. To calculate a single differential cross section, a summation is required over the other four variables. For example, to calculate the cross section as a function of the variable q_k we have

$$\frac{d\sigma}{dq_k}(q_k) = \sum_{i \neq k} \frac{d^5\sigma}{\prod_j dq_j}(\{q_i\}) \prod_i \Delta q_i \quad (5.7)$$

where $d^5\sigma / \prod_j dq_j$ is defined in equation 5.2. The resulting cross section in terms of the five variables $\{q_i\} = \{E_\gamma, Q_\Delta, \theta_\Delta^{cm}, \theta_\pi^{cm}, \phi_\pi^{cm}\}$ are shown in Figures 5.3-5.5. The error bars are a combination of the errors in the data as well as the systematic error in the tagging efficiency measurements. The error bars do not include systematic errors from other sources; these are discussed in the next section. It is worth noting at this point that the shapes of these distributions are a convolution of both the actual physical processes (both phase space and dynamics), as well as the geometrical acceptance of SALAD and the cuts imposed in the analysis. For example, if the cross section is plotted in terms of the pion's scattering angle in the laboratory frame, a certain range of forward and backward angles would be identically zero due to the acceptance of SALAD. This would result in a non-trivial effect on the shapes of the cross section when plotted in terms of other variables, as the measured variables are effectively integrated over.

The overall effect of all this is to make the conclusions model dependent. A comparison to an actual model is required, in which the above mentioned effects are corrected for in the theoretical calculation. This will be discussed in more detail in the next section.

The particular shape of the ϕ_π^* distribution is a good example of how the cuts

• $D(\gamma, pp\pi^-)$ - SALAD DATA

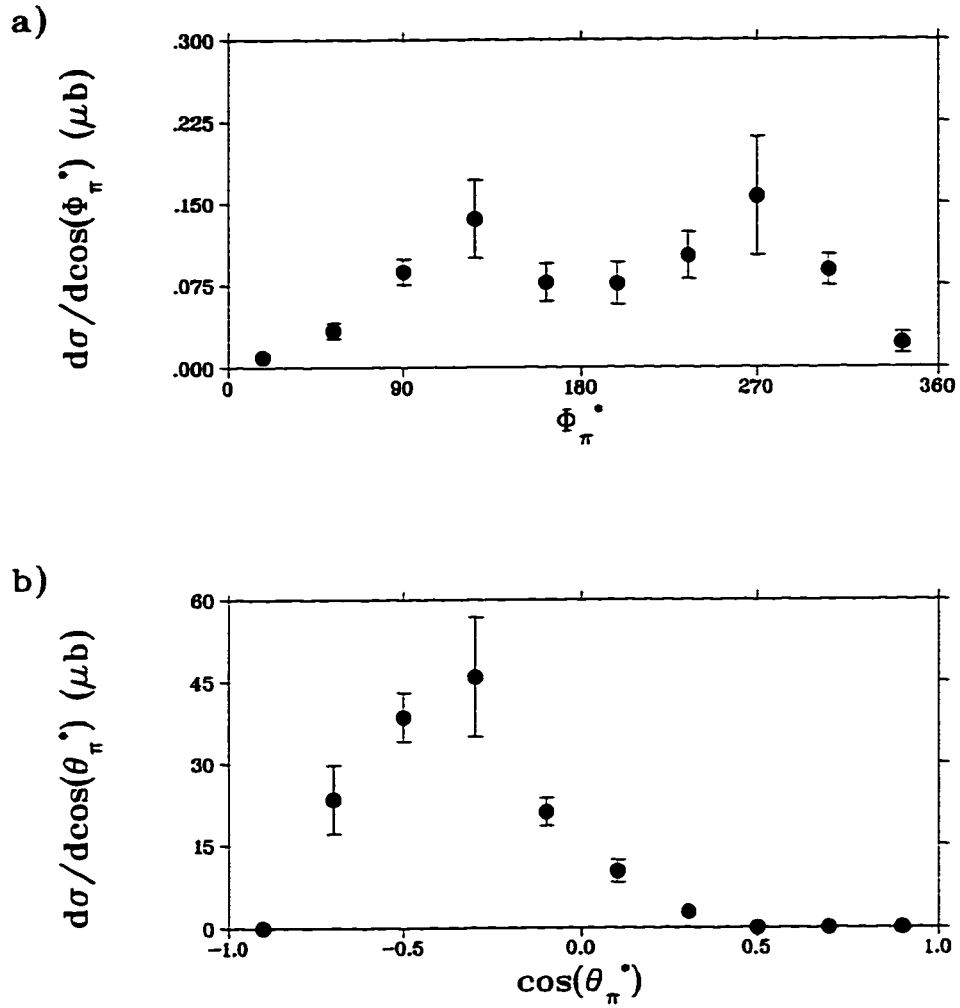


Figure 5.3: Single differential cross section for $D(\gamma, pp\pi^-)$ in terms of (a) the pion's azimuthal angle and (b) the pion's scattering angle as measured using SALAD. Both angles are calculated in the Δ rest frame, where the direction of the Δ defines the z-axis.

• $D(\gamma, pp\pi^-)$ - SALAD DATA

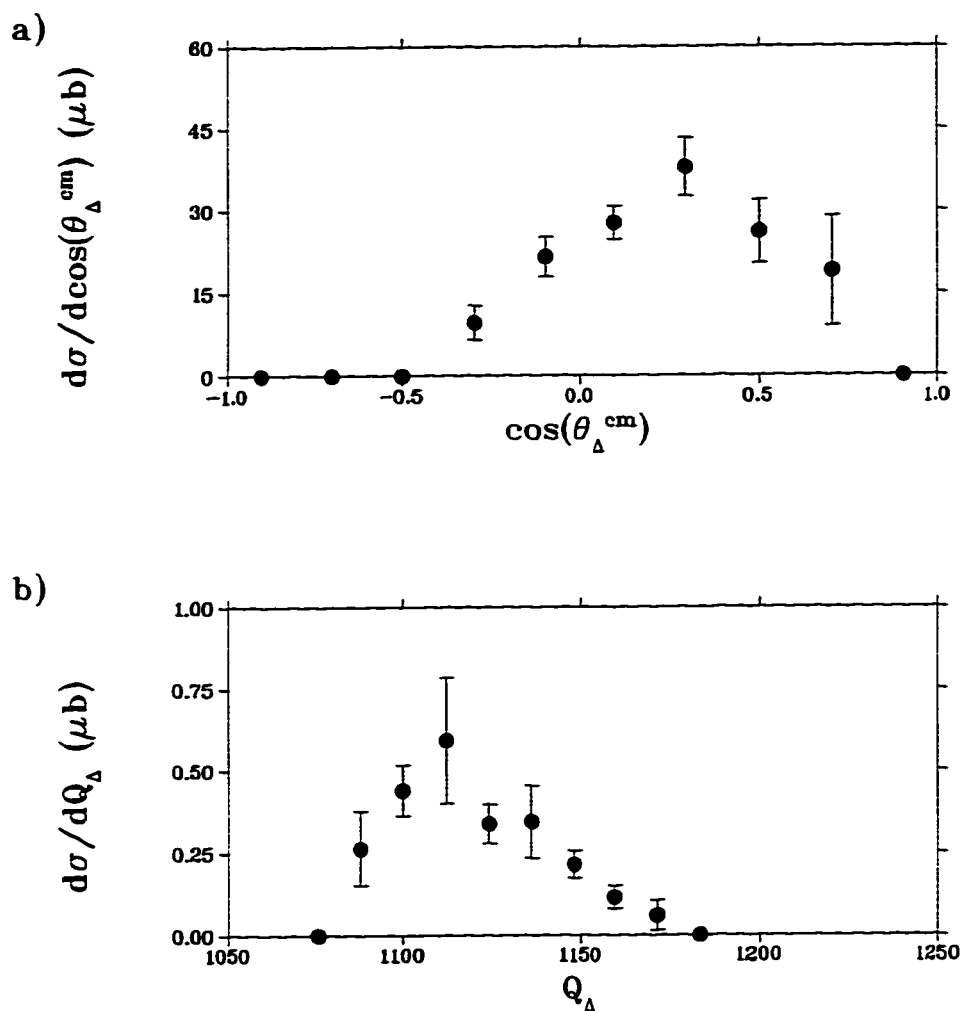


Figure 5.4: Single differential cross section for $D(\gamma, pp\pi^-)$ in terms of (a) the Δ scattering angle and (b) the $p-\pi^-$ invariant mass as measured using SALAD. The Δ scattering angle is calculated in the $\gamma-D$ centre of mass frame, where the direction of the photon defines the z-axis.

• $D(\gamma, pp\pi^-)$ - SALAD DATA

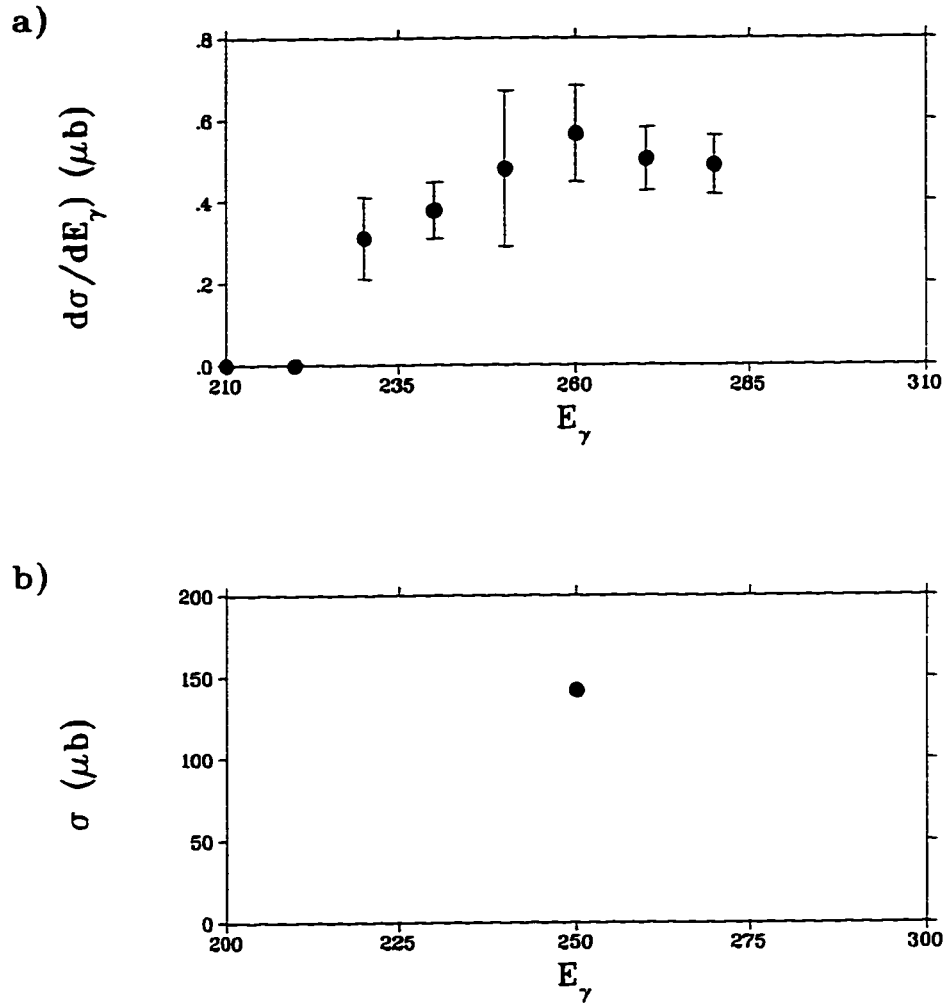


Figure 5.5: $D(\gamma, pp\pi^-)$ cross section as a function of beam energy measured using SALAD. The bottom plot is the total cross section in the measured region plotted at the centre of that region.

imposed in the analysis may affect the shapes of these distributions. A strong dip is noticed at $\phi_\pi^* = 0^\circ/360^\circ$ and 180° . These values of ϕ_π^* correspond to one of the decay products going out at the same azimuthal angle (in the laboratory frame) as the spectator nucleon, and will thus hit the same scintillator bar. Such events are excluded from the analysis as it is practically impossible to measure the energies deposited in the ΔE and E scintillators independently for each particle.

Figures 5.3b and 5.4a show the single differential cross section in terms of the variables $\cos(\theta_\pi)$ and $\cos(\theta_\Delta)$. The regions where the cross section goes to zero are inaccessible to us due to the acceptance of the SALAD detector. Although the inaccessible regions in the scattering angle distribution are expected to be the same at forward and backward angles due to the symmetry of the detector, the particular choice of coordinate system and reference frame results in shifting this symmetry.

The cross section as a function of the $p - \pi$ invariant mass and the photon energy are shown in Figures 5.4b and 5.5a, respectively. The E_γ distribution has the expected shape, showing a monotonic rise as a result of the production of a Δ resonance. The Q_Δ distribution has the expected shape as well. The production of a Δ resonance results in the initial steep rise of the cross section. Due to the maximum photon energy, however, the amount of phase space accessible to the Δ decreases as higher photon energies are not possible, and the distribution decreases monotonically until it hits zero at the point where the highest photon energy has been reached.

Figure 5.5b is the total cross section obtained by integrating the $d\sigma/dE_\gamma$ distribution over the measured range of photon energies and plotting it at the center of this range. As previously mentioned, due to the complications of the detector's acceptance, the cuts involved, and the amount of statistics available to us, the actual shapes of these

distributions as well as the magnitude of the cross section are hard to predict except in the context of a particular model. This is done in section 5.3.

5.2.1 Systematic Errors

The sources of systematic errors are quoted in Table 5.3 together with their respective contributions. The contribution of the target density to the systematics is estimated by considering the change in the target temperature and pressure, both of which were monitored throughout the experiment.

Three source data files were obtained during this experiment. The uncertainties arising from the deviations between the different wire chamber calibration files was estimated by analyzing the data with the different files. Although the wire chamber efficiencies were simulated in this experiment, any inaccuracies in the calculation of these efficiencies would result in a contribution to the systematics. A 5% systematic error was assigned to include both the wire chamber calibrations and efficiencies.

The energy loss calculation makes another contribution to the systematics. In this experiment the outgoing particles have low kinetic energies, and the calculation is quite sensitive to small uncertainties in the material thickness and density in the walls of SALAD. An error of 5% is reasonable in this case.

Particle identification makes a small contribution to the systematics. Although a 20% mixing occurs between pions and protons, the fact that *pid* information was not used directly (see section 4.1.2) succeeded in lowering the uncertainty quite substantially. The uncertainty of 1% was estimated using the Monte Carlo simulation.

In this experiment, the photon flux was calculated by assuming a bremsstrahlung distribution normalized to the tagger counts in the tagged region. A 4% systematic is

Source of error	Contribution
Target density	4%
Tracking efficiency	5%
Energy loss	5%
Particle identification	1%
Photon flux	4%
Total error	9%

Table 5.3: Sources of systematic errors and there contribution to the total systematic error.

included as a result of this extrapolation. The contribution of the tagging efficiency measurements to the error was calculated separately and will be included in the error bars for all the SALAD cross sections presented. This error was calculated by considering the deviations between the different tagging efficiency measurements for each channel, as well as the statistical accuracy of the data.

5.3 Comparison to Theory

The only theoretical calculation available to us is that of Laget which we discussed in detail in chapter 3. In this section we present a comparison of this calculation to our SALAD data, as well as a comparison between the different ingredients of this calculation.

Figures 5.6-5.8 show the results of the theoretical calculations including different FSI's. The short dashed curve includes the quasi-free diagram only, the long dashed curve includes rescattering effects, whereas the solid curve includes the short range

$\Delta - N$ interaction as well. The theoretical calculation was binned in the same 10^5 bins as the data and then integrated in the same manner. The acceptance of SALAD was applied to the theoretical calculation by setting the theoretical calculation to zero in any bin for which the efficiency calculation yields a zero value in the corresponding bin.

As may be seen from the figures, the theoretical calculations describe the data reasonably well except for the ϕ_π^* distribution. In addition the overall normalizations are in good agreement, particularly with the calculation that includes both rescattering effects and the $\Delta - N$ interaction. This may be seen clearly in Figure 5.8b where the cross section from this distribution falls right on the data.

As may be seen from these comparisons, the overall effect of the FSI's and the $\Delta - N$ interaction on the single differential cross section is about 10%-15%. This is a small effect, which is not particularly surprising, since we are looking at a single differential cross section. When integrating over many variables, any interesting effects that may be present in particular regions of phase space as a result of a strong contribution from a particular diagram will be washed out in the integration process. The best method to single out a particular diagram is to focus on a specific region of phase space where that diagram makes a strong contribution, as has been explained in detail in chapter 3. We have calculated the two dimensional cross section with respect to the Δ mass and each of the other four variables and compared that to Laget's calculation. Even at this level our statistical errors are bigger than the variations between the different ingredients of the theoretical calculation. The comparison of the single differential cross section confirms, however, that there are no strong effects of FSI's or the $\Delta - N$ interaction that contribute in a wide range of phase space to the extent that they will prevail when

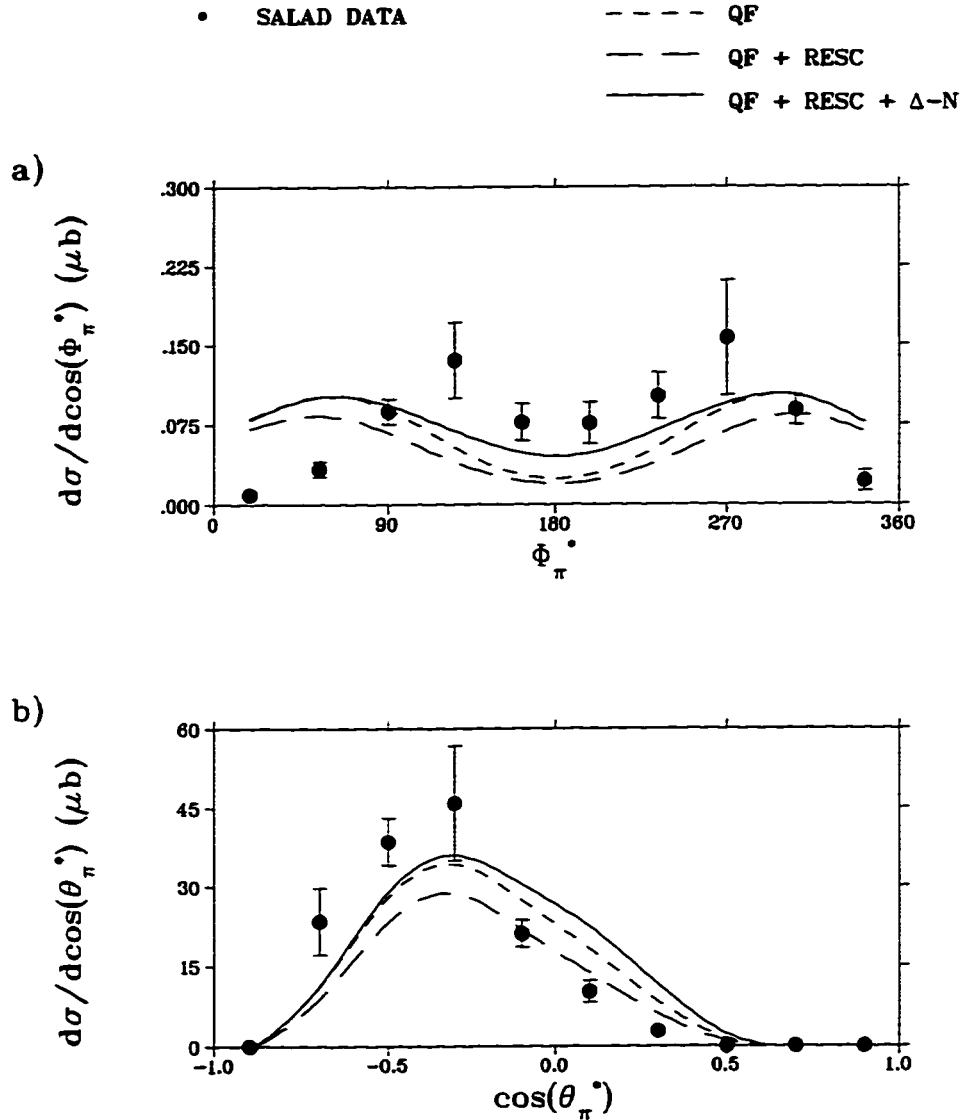


Figure 5.6: Single differential cross section for $D(\gamma, pp\pi^-)$ in terms of (a) the pion's azimuthal angle and (b) the pion's scattering angle as measured using SALAD. Both angles are calculated in the Δ rest frame, where the direction of the Δ defines the z-axis. The theoretical curves are calculated by J.M. Laget and corrected for the efficiency of SALAD.

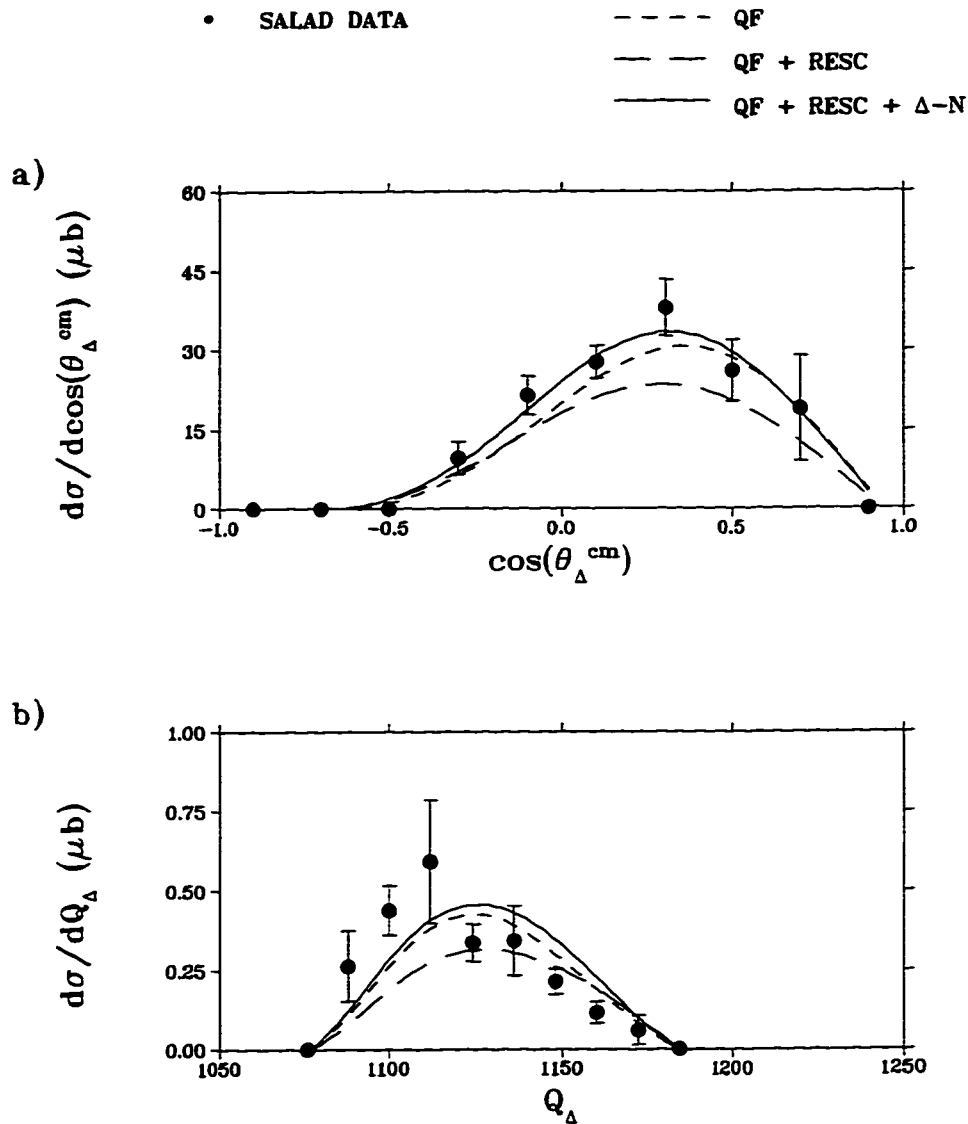


Figure 5.7: Single differential cross section for $D(\gamma, pp\pi^-)$ in terms of (a) the Δ scattering angle and (b) the $p-\pi^-$ invariant mass as measured using SALAD. The Δ scattering angle is calculated in the $\gamma-D$ centre of mass frame, where the direction of the photon defines the z-axis. The theoretical curves are calculated by J.M. Laget and corrected for the efficiency of SALAD.

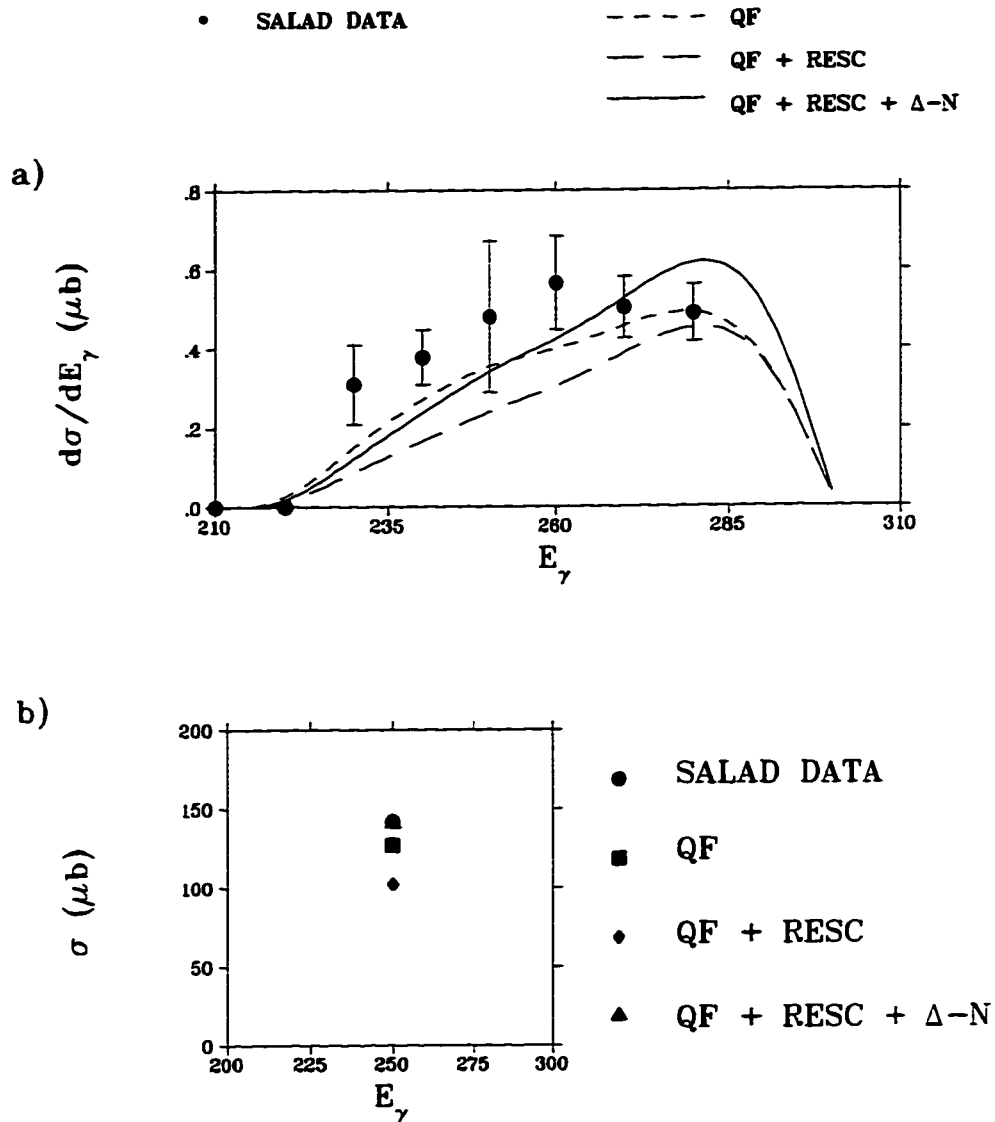


Figure 5.8: $D(\gamma, pp\pi^-)$ cross section as a function of beam energy measured using SALAD. The bottom plot is the total cross section in the measured region plotted at the centre of that region. The theoretical curves are calculated by J.M. Laget and corrected for the efficiency of SALAD.

a single differential cross section is calculated.

This is the first successful measurement of the $\gamma D \rightarrow pp\pi^-$ cross section over a 4π acceptance. A similar measurement was attempted at Mainz few years ago and failed to obtain normalizations consistent with theory.

Chapter 6

Summary and Conclusions

This is the first measurement of the $\gamma D \rightarrow pp\pi^-$ cross section covering a wide range of phase space which successfully constrains the FSI's as well as the short range $\Delta - N$ interaction. We conclude that Laget's theory is quite successful in describing the shapes of the distributions, as well as the overall magnitude of the cross section. The different FSI's and the $\Delta - N$ interaction have an overall effect of 10%-15% on the single differential cross section, with the calculation that includes $\Delta - N$ interaction having the best agreement compared to the data.

Explicit comparisons to other experiments are hard to make in this case. Most pre-existing data sets were obtained with discrete (small acceptance) detectors and are thus confined to a very limited range of phase space. Our data on the other hand is spread over a 4π acceptance with limited statistics. Moreover, as explained in section 5.2, the shape of the cross section in terms of the different variables is highly dependent on the geometrical acceptance of SALAD and the cuts imposed in the analysis. It should be noted, however, that the good agreement with Laget's theory implies a good agreement

with other experiments as well, as Laget's theory has been compared to the various experimental data available (see chapter 3).

We were unable, however, to single out the effects of the different diagrams. This is a result of the limited statistics achieved in this experiment. In order to do such a detailed comparison, one needs to focus on the particular range of phase space in which a certain diagram (FSI) has a strong contribution. This requires looking at a multi-differential cross section (i.e. fixing the values of a few kinematic variables), which in turn requires high statistics.

The limited statistics in this experiment may be attributed to three main difficulties. The first of these results from the large $\gamma \rightarrow e^+e^-$ background, which despite our extensive efforts, still made a very large contribution to the collected data. Out of about 80 million events collected in this experiment, only 3,000 events were successfully extracted. This large contribution resulted in a large collection of long data files which we had to analyze: a process that is time consuming. Needless to say, that the presence of a huge background makes it harder to extract the good events being buried under the huge background.

The second difficulty is due to the pion absorption process in the SALAD scintillators. Neither the pion's energy nor particle identification information may be used, thus reducing the number of measured quantities available to the fit.

Extensive efforts were made in the design and construction of SALAD to reduce the threshold to the minimum possible. This includes the construction of the carbon fiber tubing for the target cell, as well as the foam structure of the wire chambers. The low photon energy available at SAL combined with the relatively large detector thresholds, however, still had the most significant effect on reducing the statistics. As most of the

outgoing particles will have a small share of the kinetic energy available, they will stop in the walls of SALAD resulting in no energy and/or tracking information. In most cases, this reduces the number of measured quantities significantly for each event making it unsuitable to fit.

Although these major difficulties appear to be separate, they conspire in such a way so as to significantly reduce the yield. For example, the large amount of background present would not be hard to eliminate if enough measured quantities are present to result in overdetermined conditions so that the event may be successfully fit. The low photon energy and the relatively high detector threshold, however, result in a small number of measured quantities making the good events hard to extract. Similarly, the pion absorption process results in reducing the number of kinematic quantities available to the fit, which would not be a major problem if it wasn't for the fact that they have been already reduced due to the other effects.

As a result of these difficulties it would be impractical to run this experiment with the conditions prevailing at SAL. The experiment would be feasible, however, if the maximum energy available at SAL was higher by a few tens of MeV's. This would practically eliminate all the difficulties encountered in this experiment. The extra range of photon energy would allow most of the outgoing particles to make it above the detector's threshold, increasing the number of measured quantities per event significantly. Although the pion absorption process would still be present, the effect would be easily handled, as the extra number of measured quantities would compensate for it. An additional advantage would be achieved if the tagger would cover the energy range up to the maximum. This would increase the number of measured quantities by one, allow for a good resolution on the photon energy, and allow for a direct calculation of the

photon flux from the tagger scalars, thus avoiding the extra systematics arising from the extrapolation of the bremsstrahlung distribution.

The huge background would be easily handled in such a case. As the background is mainly due to $\gamma \rightarrow e^+e^-$ events, it results in two track events, typically in coincidence with the tagger. If the SALAD trigger is set so as to look for three calorimeter triggers (in coincidence with the tagger, if present), most of these events will be excluded at the hardware level, resulting in small dead-times.

In addition, a careful analysis of the theoretical calculation is required after correcting for the acceptance of the detector. For example, if the short range $\Delta - N$ interaction is to be investigated, one needs to find the regions of phase space where this interaction is expected to have a strong contribution as predicted by the theoretical calculation. The calculation has to be corrected by the efficiency of SALAD to make sure that this region will be accessible to SALAD with reasonable statistics.

It should be added at this point that the requirement of a three-fold coincidence, which would still cut out an appreciable number of good events, will not result in the loss of interesting physics. The physical region excluded would constitute mainly quasi-free events, as the spectator nucleon is required to have a momentum of >150 MeV/c to make it above threshold.

A similar experiment may be done at SAL using discrete detectors. With the resources currently available at SAL, this is a practical way of investigating a particular FSI such as the $\Delta - N$ interaction. On one hand, one would be able to run at the highest beam flux available, increasing the event rate by an order of magnitude over what SALAD could handle. on the other hand, the complication arising from the relatively high detector thresholds would be avoided. It should be emphasized, however, that this

experiment would only be worth doing if such a region of phase space does exist in the energy range presently available at SAL. A search is thus required of the theoretical calculation over all regions of phase space to investigate whether such a region does exist in this energy range.

Last but not least, a complete theoretical calculation is required, particularly for the short range $\Delta - N$ interaction. This would allow solid conclusions about our understanding of the mechanisms involved, and would confirm the presence or absence of other possible mechanisms. On the other hand, the only calculation presently available for the $\gamma D \rightarrow pp\pi^-$ reaction is that of Laget. It would be advantageous to have additional calculations to allow for consistency checks.

Bibliography

- [1] Sarah C.B. Andrade et al. *Phys. Rev. C*, 34:226, 1986.
- [2] P.E. Argan et al. *Nuc. Phys.*, A296:373, 1978.
- [3] P.E. Argan et al. *Phys. Rev. Lett.*, 41:86, 1978.
- [4] P. Benz et al. *Nuc. Phys.*, B65:158, 1973.
- [5] I. Blomqvist and J.M. Laget. *Nuc. Phys.*, A280:405, 1977.
- [6] S. Brehin et al. *Nuc. Ins. and Meth.*, 123:225, 1975.
- [7] E.B. Cairns et al. *Nuc. Instr. and Meth.*, A321:109, 1992.
- [8] H. Clement et al. *Phys. Lett. B*, 337:43, 1994.
- [9] R.L. Craun and D.L. Smith. *Nuc. Ins. and Meth.*, 80:239, 1970.
- [10] L.O. Dallin. *Proc. of the 1989 IEEE Part. Acc. Conf.*, 1. 1989.
- [11] H.G. Dosch and Erasmo Ferreira. *Phys. Rev. C*, 38:2322, 1988.
- [12] Richard C. Fernow. *Introduction to Experimental Particle Physics*. Cambridge University Press, 1986.

- [13] Erasmo Ferreira and H.G. Dosch. *Phys. Rev. C*, 42:2334, 1990.
- [14] Erasmo Ferreira and H.G. Dosch. *Phys. Rev. C*, 40:1750, 1989.
- [15] Hamberto Garcilazo. *Phys. Rev. C*, 42:2334, 1990.
- [16] K. Gottfried and J.D. Jackson. *Phys. Lett.*, 8:144, 1964.
- [17] E.D. Hackett. *Phys. Rev. C*, 53:R1047, 1996.
- [18] Itonaga et al. *Phys. Rev. C*, submitted.
- [19] J.D. Jackson. *Rev. Mod. Phys.*, 37:484, 1965.
- [20] Zbigniew Jakubowski and Michael Kobel. *Nuc. Ins. and Meth.*, A297:60, 1990.
- [21] N.R. Kolb et al. *Phys. Rev. C*, submitted.
- [22] N.R. Kolb et al. *Phys. Rev. C*, 49:2586, 1994.
- [23] Stanely Kowalski et al. *IEEE Part. Acc. Conf.*, 1, 1989.
- [24] J.L. Laclare and R. Servanckx. *IEEE Trans. Nuc. Sci.*, NS-18:207, 1971.
- [25] J.M. Laget *Nuc. Phys.*, A296:388, 1978.
- [26] J.M. Laget *Nuc. Phys.*, A312:265, 1978.
- [27] J.M. Laget. *Nuc. Phys.*, A335:267, 1980.
- [28] J.M. Laget. *Phys. Rep.*, 69:1, 1981.
- [29] J.M. Laget. *Can. J. Phys.*, 62:1046, 1984.

- [30] P.P. Langill. A large acceptance detector for photonuclear reactions. Master's thesis, University of Alberta, 1989.
- [31] W. Leidmann and H. Arenhovel. *Can. J. Phys.*, 62:1036, 1984.
- [32] W.R. Leo. *Techniques for Nuclear and Particle Physics Experiments*. Springer-Verlag, 1987.
- [33] J.L. Matthews and R.O. Owens. *Nuc. Ins. and Meth.*, III:157, 1973.
- [34] G. Mechttersheimer et al. *Nuc. Phys.*, A324:379, 1979.
- [35] M. Nikolic'. *Kinematics and Multiparticle Systems*. Gordon and Breach Science Publishers, 1968.
- [36] R.O. Owens. *Nuc. Ins. and Meth.*, A288:574, 1990.
- [37] V. Rossi et al. *Nouvo Cimento*, 13A:59, 1973.
- [38] J.J. Sakurai. *Modern Quantum Mechanics*. Addison Wesley Publishing Company, 1985.
- [39] P.E. Scheffler and P.L. Walden. *Phys. Rev. Lett.*, 24:952, 1970.
- [40] L.I. Schiff. *Phys. Rev.*, 252:252, 1951.
- [41] R. Servanckx and J.L. Laclare. *IEEE Trans. Nuc. Sci.*, NS-18:204, 1971.
- [42] J.M. Vogt et al. *Nuc. Ins. and Meth.*, A324:198, 1993.
- [43] G.T. Wright. *Phys. Rev.*, 91:1282, 1953.